Liquid–mediated directed self–assembly for soft electronic applications

李　玲穎

February 2022

Liquid–mediated directed self–assembly for soft electronic applications

李　玲穎
Doctoral Program in Materials Science and Engineering

Submitted to the Graduate School of
Pure and Applied Sciences
in Partial Fulfillment of the Requirements
for the Degree of Doctor of Philosophy in
Engineering

at the
University of Tsukuba

Contents

List of figures

List of tables

Acknowledgements

I would first like to express my sincere gratitude to my supervisor Prof. Tomonobu Nakayama at the Graduate School of Pure and Applied Sciences of University of Tsukuba and the International Center for Materials Nanoarchitectonics (MANA) of National Institute for Materials Science (NIMS) for the continuous supporting, understanding, and encouraging of my doctoral study. The door to Prof. Nakayama office was always open whenever I felt bewildered about my research. Without his guidance and constant feedback this PhD would not have been achievable. His motivation, creativity, patience, immense knowledge, and truth–seeking spirit became the beacon for me in all the time of my doctoral course.

Many thanks also to the rest of my thesis committee: Prof. Yohei Yamamoto, Prof. Naoki Fukata, Prof. Jie Tang, and Dr. Takeo Minari for their valuable comments, encouragement, and scrutiny, which incented me to enrich my research from diverse perspectives. I would extend my thanks gratefully to Dr. Takeo Minari and Prof. Wanli Li for their supervisory roles, who provided me plenty of help, guidance, and encouragement along the way. Without they as always support it would not be possible to finish this PhD.

My sincere thanks also go to Dr. Mizuki Tenjimbayashi for his inspiring advices, profound knowledge and generous support on my research. I would also like to acknowledge Prof. Xuying Liu, Prof. Qingqing Sun, Dr. Hiroyo Segawa, Dr. Chisato Niikura, and Dr. Jinting Jiu, for giving me their kind suggestion, help, and inspiration during my doctoral course. I express my deep gratitude to Dr. Masayuki Kanehara for offering the state–of–the–art and high–quality functional ink bountifully. And I would like to acknowledge Prof. Katsuaki Suganuma, Prof. Chuantong Chen, Prof. Genki Yoshikawa, and Mr. Masaaki Matoba for their generous supports on research facilities.

I thank all my research colleagues in Nano Functionality Integration Group, Dr. Yoshitaka Shingaya, Dr. Adrian Diaz–Alvarez, Dr. Qiao Li, Mrs. Keiko Tanaka and Mrs. Kayoko Hatori. My sincere thanks also go to all my co–workers in Printed Electronics Group, Mrs. Yoko Yoshikawa and Mrs. Yuko Taki. Without their kind instruction, constant encouragement, and warm support, it would not be possible for me to conduct this research smoothly. I also want to express my sincere appreciation to my fellow researchers, Prof. Daiming Tang, Prof. Jie Wang, Dr. Shisheng Li, Dr. Kewei Sun, Dr. Ran Liu, Dr. Siyu Cao, and Ms. Yintong Huang, for all the effort we did, and all the fun we have had in last three years.

I gratefully acknowledge the kind support and cultivation received towards my PhD through Research Fellowship for Young Scientists, Japan Society for the Promotion of Science (JSPS). I am also grateful for the funding received through NIMS Graduate Research Assistantship.

Finally, I would love to say a very big thank you to my parent and my grandparent for inspiring me to realize my own potential and supporting me materially and spiritually throughout my life. All the encouragement, devotion, support, trust, and love they have provided me over the years help me to work hard and focus on the pursuit of my dreams without fears.

Lingying Li

Tsukuba, Japan

February 2022

Chapter 1

Introduction

1.1 The rise of soft electronics

1.1.1 Brief history of soft electronics

The concept of soft electronics has been put forward for several decades. It is to follow up the world's growing demands of electronic manufacturing toward diversified functionalities and dimensional miniaturization.[1] In principle, the transition from stiff electronics to soft electronics can not only conserve device space, but also offer significant applicability to be integrated with various surfaces.

Besides wiring and cables, which can be found everywhere as the prime examples of soft electronics, the silicon solar cells equipped for spacecraft were first thinned to reduce the thickness and lower specific mass in the 1960s.[2] By using a thin plastic substrate instead of the conventional rigid support, these first flexible solar cells allowed a certain degree of wrapping over a large area to improve energy supply (**Figure 1.1**). Along with this concept, a gradual development, including conductive polymers,[3] amorphous silicon,[4] organic semiconductors,[5] and metal oxide semiconductor thin–film transistors[6] in the following decade, took a huge step forward in the processability and flexibility. Thus these materials laid the groundwork for developing and manufacturing soft electronics in applications requiring bending, stretching, folding, rolling, deforming, and self–healing, that cannot be satisfied by conventional rigid electronics.

As time passes, the interest in exploring new functional materials and novel fabrication technologies keeps growing for manufacturing high–performance and scalable electronics directly on soft substrates. This interest not only promotes flexibility but also endows the electronics with stretchability and self–heal ability owing to the strong molecular interactions of elastomeric substrates,[7–8] leading to a more versatile application prospect including flexible organic light–emitting diode (OLED), stretchable organic photovoltaics, and rechargeable soft batteries.[9–11] At the same time, as there is a growing issue over sustainability, biodegradability has been taken into account by utilizing the environment–friendly polymer or cellulose that can be broken down into small constituent pieces or completely decomposed in the soil.[12] Likewise, biocompatibility has also been studied under the unique characterizations of soft electronics through polymers or functional materials that do not affect normal physiological activities.[13] These criteria lead the developing trend of next–generation devices that can be integrated into complex or dynamic surfaces, for example, bioresorbable devices,[14] neuromorphic biological systems,[15] and cognitive soft robotics.[16]

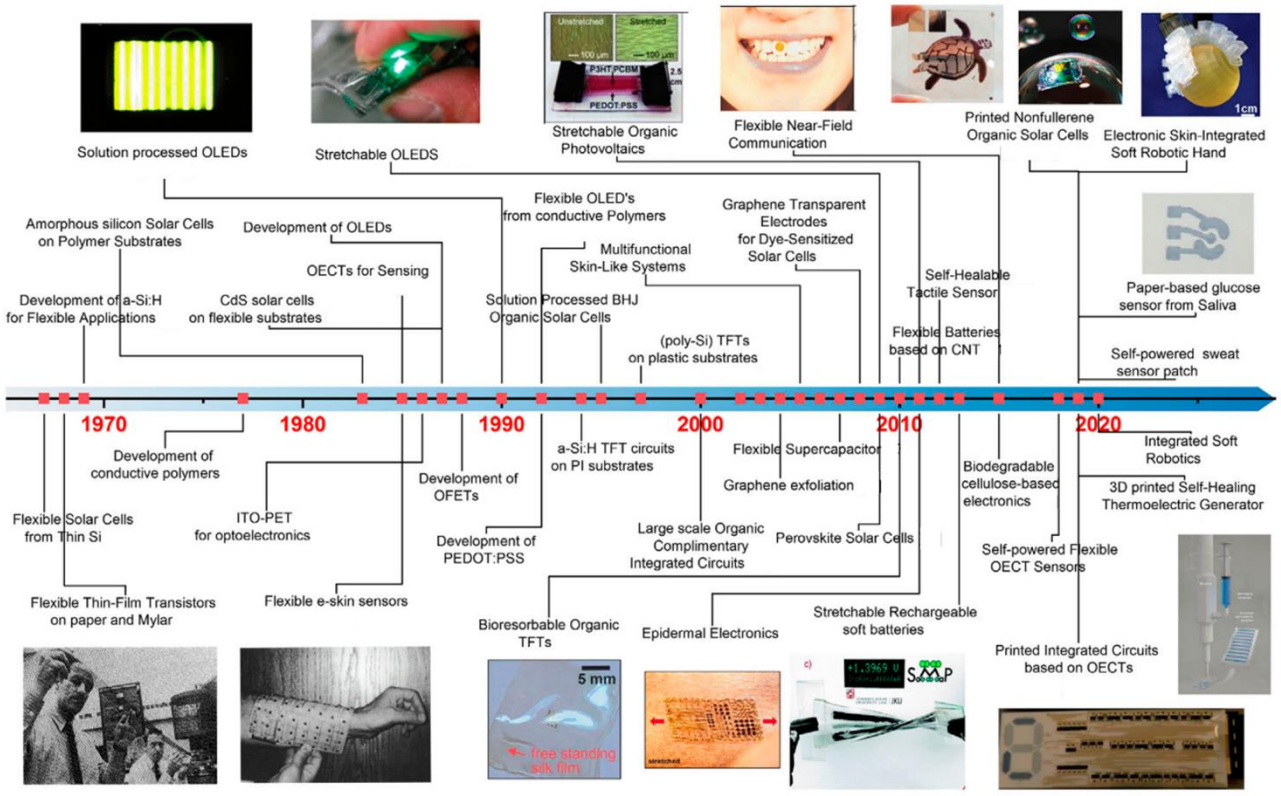

Figure 1.1. Timeline of major discoveries and advances in the development of soft electronics, from the 1970 to the present.[17]

1.1.2 Status, value, and challenges

These significant advancements in soft electronics open new doors to bringing electronic science and technology into daily life, such as wearable, smart textiles equipped with biosensors for monitoring bio–signals and habits;[18–19] flexible optoelectronics with optical transparency and electrical conductivity for customized displays, architecture, and electro–magnetic interference;[20–22] as well as skin prosthesis and micro soft robot with integrated conformable sensors and actuators for recognizing external stimuli and harvesting energy.[23–25] Even though conventional electronics are capable of these functions to a certain degree, soft electronics are intended to adhere to the arbitrary surface via hybrid strategies to carry out higher perception–driven tasks, or be highly deformable standalone devices with prominent portability, disposability, low cost, and lightweight, which are expected to offer an unparalleled comfort toward our daily life.

The definition of soft changes along with the applications. From rolling and bending for scalable handling of large–area solar cell panels and photovoltaics,[26–27] to stretching and conforming onto irregularly shaped circuits,[27–28] to twisting and deforming into electronic skin,[29–30] soft electronics are expected to keep the balance between reliability and device performance. While plenty of early–stage studies in progress and significant innovations have been reported already, fabricating soft electronics that can replace existing products and be put into service in our daily life is a grand challenge. As a result, soft electronic manufacturing toward dimensional miniaturization and multifunctionality with advanced adaptability, dexterity, and reliability is highly demanded to cope with the increasingly complicated circuit design and uncertain work environment. This offers scientific research and

development enormous opportunities to undertake in–depth study and advance this area considerably and rapidly.

1.1.3 Opportunities and applications

So far, soft electronics are generally manufactured by vacuum or solution processes. Owing to the advantages of soft electronics specified above, vacuum–processed soft electronics were commercialized in 2012 as a revolutionary driving unit for integrating liquid crystal displays, such as those applied in electronic paper, mobile phones, and flat panel displays. Until now, the further commercialization of soft electronics has been achieved in the application of flexible and foldable OLED displays. The commercial success of soft electronics indicates that vacuum–processed soft electronics possess high functionality and reliability during daily use. This prompts researchers to graft this technology onto other fields beyond display technology.

On the other hand, compared to vacuum–processed soft electronics, solution–processed soft electronics encounter drawback of low device quality, which may arouse subsequent low–performance issues.[31] Aside from this issue, solution–processed soft electronics are considered as one of the most promising next–generation devices, which is attributed to its streamlined and cost–effective fabrication, sustainable and versatile products, as well as flexible adaptability.[32–33]

Notably, the number of soft electronics studies has seen explosive growth in nearly two decades. **Figure 1.2** shows the number of research papers published from 2000 to 2021, based on Google Scholar and Web of Science searches. Overall, the number of soft electronics studies has increased substantially from 61 to 211 per year in 2012. From then on, the number of research papers is expanding dramatically and continuously and reached 2049 per year in 2021. As the manufacturing process of vacuum–processed soft electronics is already a mature technology, the studies of solution–processed soft electronics are considered to occupy the leading position in the contemporary scientific community. Therefore, we could know that liquid–mediated soft electronics equipped with novel functionality and reliable performance are highly demanded to fit the needs of today's academi and industrial requirements.[34] In this chapter, the mainstream fabrication technologies for soft electronics will be introduced and compared systematically, as well as novel strategies for solution–processed soft electronics will be summarized and evaluated.

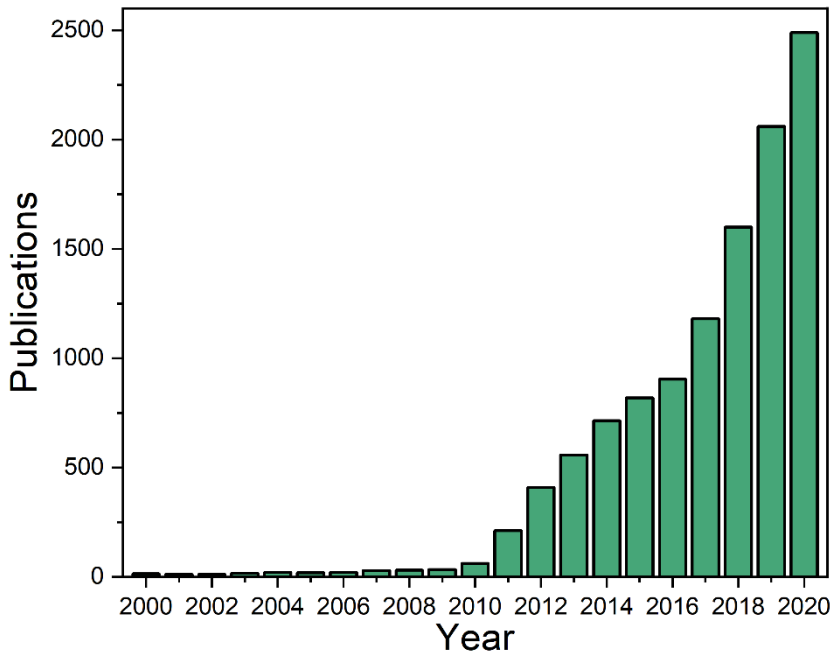

Figure 1.2. The number of the papers published per year obtained for the term "soft electronics" from 2000 to 2021, based on Google Scholar and Web of Science searches.

1.2 Overview of manufacturing technologies for soft electronics

In recent years, the demand for high–performance, high–resolution, reliable, soft electronics has been increased rapidly. To meet the market requirements, a lot of efforts have been made to fabricate soft electronics using a variety of functional materials, such as conductive materials, semiconducting materials, and dielectric materials, on various soft substrates, such as polyethylene naphthalate (PEN), polyethylene terephthalate (PET), polyimide (PI), polydimethylsiloxane (PDMS), and cyclic olefin polymer (COP).

However, fabricating soft electronics on soft substrates is not an easy task. The commercialization of soft electronics with satisfactory conductivity and flexibility in a facile, scalable, and versatile manner remains an open issue. Generally, the manufacturing technologies can be distinguished into two categories, top–down subtractive process and bottom–up additive process. In this section, the current situation and recent progress of soft electronic manufacturing technologies are summarized and analyzed.

1.2.1 Top–down subtractive technologies

In top–down subtractive technologies, various lithography technologies are utilized to downscale micro–/nanoscale patterns. Photolithography and scanning beam lithography, including extreme ultraviolet lithography, focused ion beam and electron beam lithography, are the conventional fabrication technology of this field.[35] The most well–known and widespread subtractive technology is photolithography, which is therefore selected as the demonstration to illustrate herein.

Photolithography is the mature patterning technology for electronic manufacturing. As lithography systems upgrade the wavelength technology with increasing stronger wavelength peaks from a broad spectrum with multiple peaks at 436 nm, 405 nm, and 365 nm[36–37] to present–day wavelength of extreme ultraviolet at 13.5 nm (ASML,

2021), it proved the far more competence in decreasing the minimum feature dimensions to realize Moore's law and More than Moore concepts that one could ever have imaged.

In detail, top–down photolithography is to pattern functional microstructures on the target substrate by exposing and constructing a pre–coated thin–film photoresist through a photomask. The photomask is generally made of glass and coated by a thin chromium layer for light blocking. The selective light exposure induces the chemical changes of the photosensitive materials, triggering the selective solubility variation of the photoresist through rinsing in a developer solution. The exposed regions of the positive and negative photoresists can be selectively removed upon developing, leading to a three–dimensional composite on the substrate (**Figure 1.3**). Afterwards, a subsequent process of vacuum evaporation, etching, stripping, and baking is used to define features of functional micro–/nanostructures.

The resolution of subtrative photolithography keeps increasing owing to the continuously reduced exposure wavelength and the increased numerical aperture, which have pushed the boundary to the resolution limit into sub microscale on Si substrates. In the meanwhile, photolithography has been utilized to fabricate patterns for soft electronics as well. However, depending on the harsh process conditions, such as chemical etching, developing, and high–temperature baking, an additional pattern transferring is commonly required to transfer the patterned circuit from the stiff Si substrate onto the targeted soft substrate.[38–39] The entire process exposes the problems toward the sustainable manufacturing of soft electronics, including cumbersome operation, severe waste of patterning materials, high cost, and trivial pattern transfer.

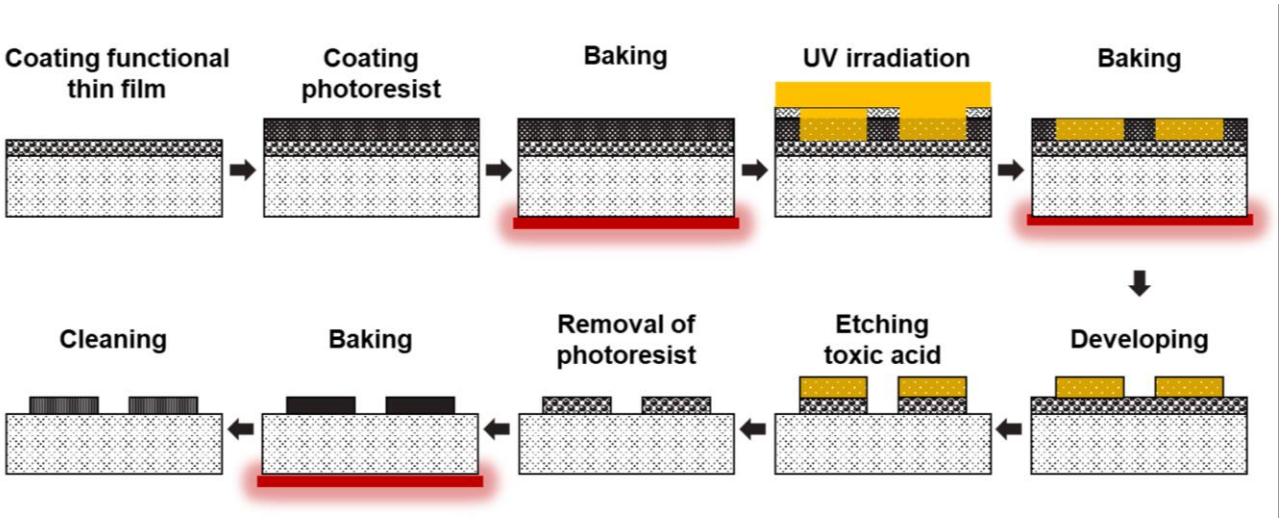

Figure 1.3. Schematic representation of the manufacturing process of top–down subtractive photolithography using negative photoresist.

1.2.2 Additively manufactured technologies

In consequence, additively manufactured technology as a promising replacement attracts increasing attention in soft electronic manufacturing. This is because the technology allows functional materials to be patterned on soft substrates via a fully bottom–up process, offering great opportunities that include higher design freedom, shorter development iterations, more compact electronic devices, and more energy–efficient production line. The additively manufactured technologies for soft electronics can be mainly classified into two categories, printing and self–

assembly. Each category of manufacturing technology will be introduced in detail.

1.2.2.1 Printing technology

Among various fabrication process, printing technology has been widely studied owing to their distinct capacity to break away from mainstream rigid silicon–based electronics to deposit the functional ink directly on soft substrates in a straightforward and efficient manner.[40] As shown in **Figure 1.4**, the functional suspension with dispersed micro–/nanomaterials can be simply printed onto the designated regions on the targeted substrate and the electrodes can be obtained after drying. Two points in this technology are worthy of notice, the printability/solubility of dispersed materials in functional inks and the fidelity of printed structures with high–resolution and precise alignment due to rheological properties during printing process.[41]

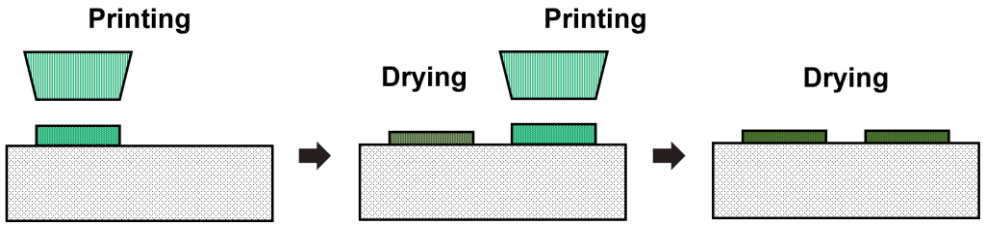

Figure 1.4. Schematic representation of the manufacturing process of printing technology.

In order to meet the different demands during the practical application, different printing technologies have been invented and applied according to the expected resolution and dimension of soft electronics.[42] For high–resolution electronic manufacturing, printing technologies, including inkjet printing, aerosol jet printing, screen printing, and gravure printing, can handle the demanding work precisely. When large–scale fabrication is required, the roll–to–roll (R2R) technologies, utilizing gravure printing, flexographic printing, and rotary screen printing, stand out. As shown in **Figure 1.5**, printing techniques with various printing approaches and equipment offer the fabrication of soft electronics with various featured sizes and processabilities.

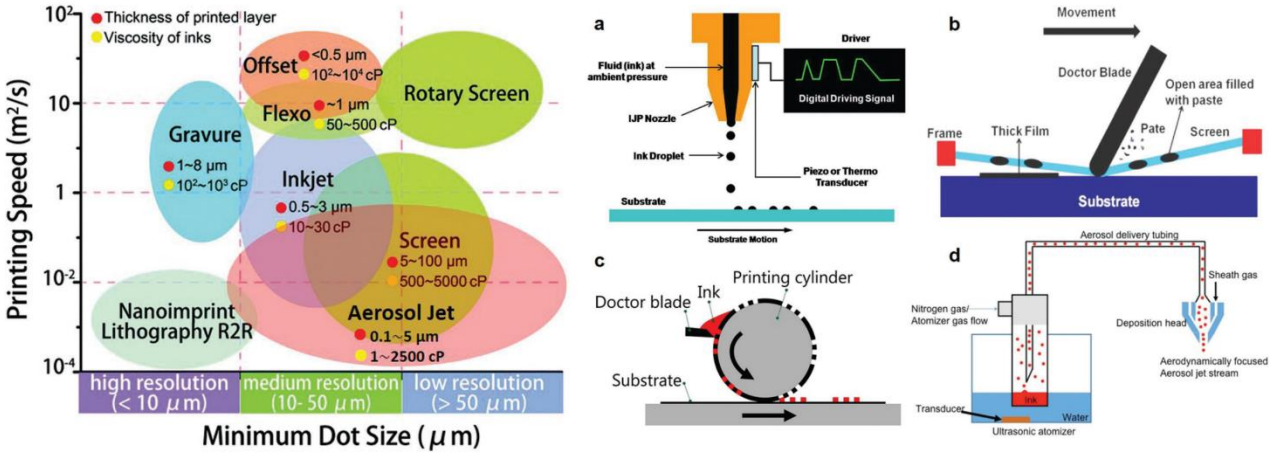

Figure 1.5. Left: Phase–diagram of printing speeds and printing resolution demonstrated by the mainstream printing technologies. The minimum layer thickness (red dot) and the demanded ink viscosity (yellow) dot have been marked.[43] Right: Schematic representation of different kinds of printing technologies, (a) inkjet printing, (b) screen

printing, (c) gravure printing, and (d) aerosol jet printing.[44–45]

1.2.2.2 Self–assembly technology

Self–assembly technology for soft electronics has gathered increasing attention. And it is expected to play a significant role in next–generation soft electronic manufacturing owing to its low equipment demands, mild process conditions, and excellent cost efficiency. Compared to rigid subtractive photolithography and delicate printing technologies, self–assembly enables high–performance soft electronic manufacturing over large areas. As shown in **Figure 1.6**, the functional ink can be self–assembled onto the designated regions through appropriate surface modification and then dry into functional patterns. The materials and equipment are easy to be prepared, and the entire process can be implemented facilely in laboratories.[46] Despite the demerits of low–resolution issue, self–assembly technology is highly beneficial for soft electronic manufacturing without harsh constraints.

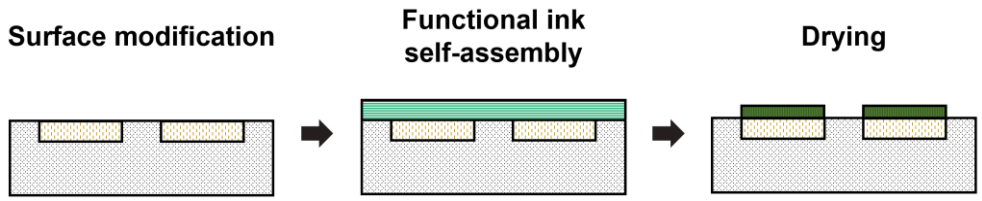

Figure 1.6. Schematic representation of the manufacturing process of self–assembly technology.

The critical point to trigger the self–assembly is to modify the substrate effectively so that the substrate can be endowed with controllable driving force such as capillary force[47], buoyancy force[48], liquid surface tension[49], magnetic field[50], acoustic field[51] and electric field (**Figure 1.7**).[52] As a result, various structured patterns can therefore be self–assembled into diversified functional micro–/nanostructures, such as monolayer structures,[53–55] three–dimensional structures,[56] and large–scale grids.[57] Nowadays, more and more studies have been focused on how to precisely control the self–assembled structures with high–accuracy and customizable topography, for example, introducing soft lithography[58–59] or combing with printing technics[60–61] to further confine the patterning positions in the self–assembly systems. These efforts lead to the complication of the self–assembly process, weakening the advantage.

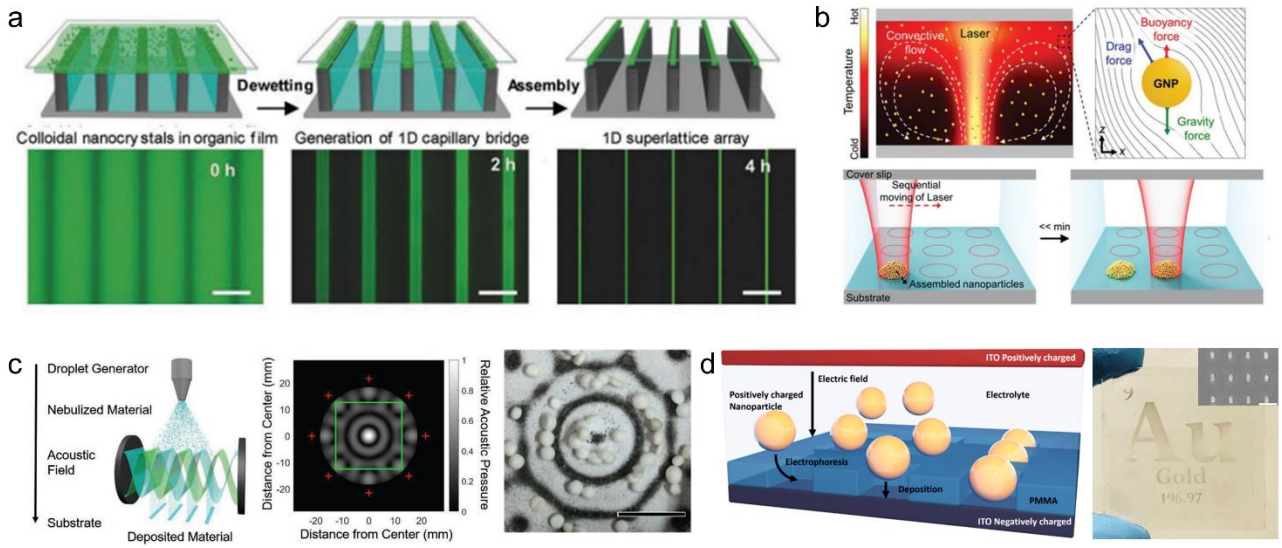

Figure 1.7. Liquid–mediated self–assembly technologies triggered by different driving force, (a) capillary force,[62] (b) buoyancy force,[48] (c) acoustic field,[51] and (d) electric field.[58]

1.3 Motivation of present research

1.3.1 Issues associated with self–assembly technologies

Among various conventional lithography technologies and emerging additively manufacturing approaches, the technology of self–assembly for soft electronic manufacturing driven by surface energy contrast is one of the most promising approaches because of its high compatibility and versatile applicability with extensive applications ranging from soft printed circuits to wearable devices. By regulating solid and liquid surface energies, the desired functional ink can spontaneously flow into the designated regions and thus form functional patterns, revealing rapid process simplicity with freeform structure.

However, the typical resolution of conventional self–assembly technologies triggered by surface energy contrast is not sufficient for practical applications in the rapidly evolving soft electronic market. As shown in **Figure 1.8, left**, the self–assembled functional electrodes exhibited coarse edge and unclear boundary, which deteriorates the patterning fidelity.[71,63] A mainstream method for overcoming this issue is to build ancillary templates above the substrate for providing extra solid surface energy contrast and assisting the self–assembly property. This approach has been widely successful in the creation of high–performance patterned soft circuits, as demonstrated by some pioneering studies using structured templates, including ice crystals,[63] fluoropolymers,[64] bubbles,[65] leaf skeletons,[66] spider's silk web,[67] cracked gels,[68] and nanoimprinted stamps.[69] However, all these methods require cumbersome and expensive processes (e.g., photolithography, electron beam lithography, etching, or biological cultivation) for building templates. And they are not promising for the scalable production of high–performance functional composites that can be integrated with soft electronic manufacturing.

In the meanwhile, the current electrodes fabricated by self–assembly technologies suffer from the inherent coffee–ring phenomenon severely (**Figure 1.8, right**). This kind of intrinsic evaporation–induced ring structure can be easily found in almost all sorts of liquid–mediated patterned electrodes, which causes the inhomogeneous solute alignment and affects the flatness, uniformity, and, more seriously, the electrical properties of the fabricated

electronics.[70]

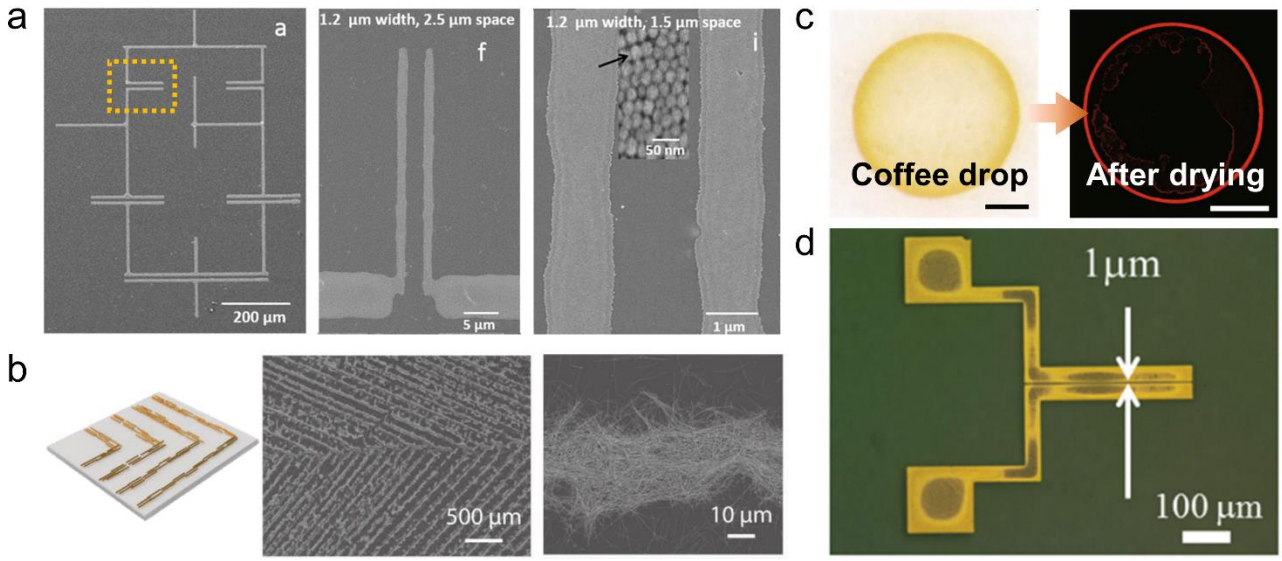

Figure 1.8. Current issues of self–assembly technologies, including low resolution of patterned functional micro–/nanostructures with (a) silica nanoparticle patterns[71] and (b) silver nanowire (AgNW) patterns[63] and coffee–ring effect with fluorescent polystyrene patterns[72] and gold nanoparticle (AuNP) patterns.[73]

1.3.2 Strategies for development of liquid–mediated directed self–assembly

Vacuum ultraviolet (VUV) light provides a shortcut to replace the template because VUV–induced photochemical reactions can efficiently convert a hydrophobic soft polymer substrate into a hydrophilic surface, leading to the directed self–assembly of soft electronics. Recently, our group further proposed the parallel vacuum ultraviolet (PVUV) technique, which can generate highly straight VUV light to modify the substrate with precise and well–defined modified hydrophilic patterns. This process has enabled the directed self–assembly of metal nanoparticle (NP) ink, leading to large–area functional patterns with microscale resolution.[74]

Diverging from the prevailing studies based on honing the difference between hydrophilicity and hydrophobicity, we propose that the self–assembly process driven merely by modifying the hydrophilic and hydrophobic performance on the substrate is not sufficient for high–resolution patterning. Inspired by the Tokay gecko as shown in **Figure 1.9**, whose tiny feet exhibit superior adhesion to almost any material via both mechanical and chemical architecturing,[75–76] the surface adhesion on the designated regions of the substrate is expected to be regulated simultaneously to further boost the self–assembly property.

Furthermore, the unique rheological property in the liquid–mediated directed self–assembly is going to be utilized rationally. The periodic internal microflow in the deposited functional suspension induced by evaporative convection can be utilized as a natural driving force to trigger the spontaneous alignment of the dispersed functional materials, leading to large–scale directed self–assembly for soft electronic manufacturing. Thus, this study aims to spontaneously organize and pattern functional micro–/nanomaterials into highly ordered and high–performance soft electronics that are actively adaptive to freeform circuit designs without the need for elaborate template construction by leveraging the advances in directed self–assembly technologies.

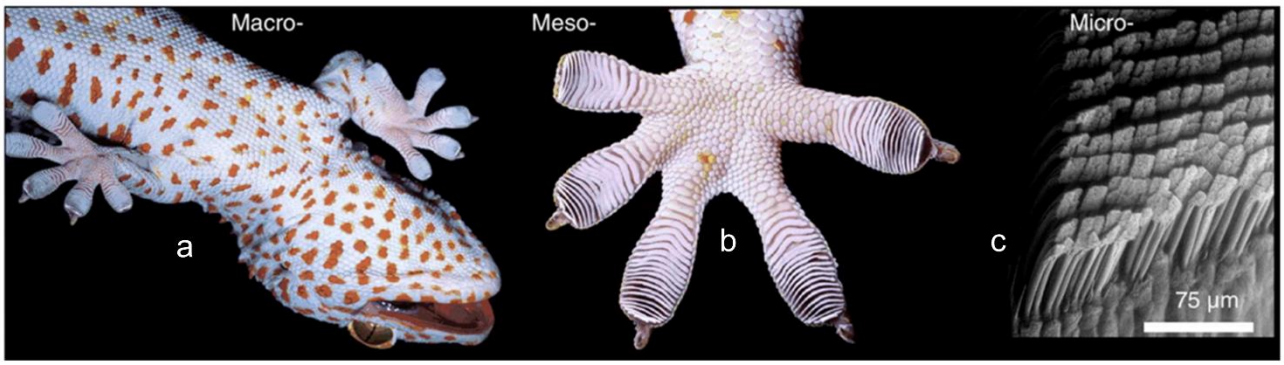

Figure 1.9. Structural hierarchy of the gecko adhesive system. (a and b) Gecko toe pads. (c) Gecko setae.

1.4 Purpose and scope of this study

The purpose of this study is to develop novel directed self–assembly strategies for additively manufacturing high–performance and highly reliable soft electronics, enabling the streamlined liquid–mediated manufacturing technologies to replace or share the responsibility of conventional lithography as well as produce the novel electronics that cannot be achieved by lithography. Attempts are also made to break the bottleneck of the present challenges in soft electronic manufacturing. The thesis presents one fundamental dual–surface–architectonic (DSA) strategy which endows soft polymer substrates with distinct directed self–assembly property. Moreover, two novel strategies for high–performance soft electronic fabrications based on the DSA strategy have been demonstrated, revealing the strong feasibility and practicability. The research results of this study enrich the theory of liquid–solid interfacial engineering, expand the application scope of liquid–mediated directedly self–assembled technologies, and provide fundamental guides for prototyping and manufacturing of advancing arbitrary as well as spatial soft electronics.

In *Chapters 1 and 2*, a brief description of soft electronics (history, status, value, challenges, opportunities, and application fields), an overview of manufacturing technologies for soft electronics, and the existing issues of self–assembly technologies are listed. At the same time, the purpose of developing liquid–mediated directed self–assembly strategies for patterning high–performance and high–resolution soft electronics is introduced. The manufacturing technologies and the employed characterization techniques are summarized.

In *Chapter 3*, the concept of using surface adhesion force to magnify the directed assembly property is demonstrated, which is referred as the DSA strategy. By a cascade modification using PVUV exposure and alkali rinsing, the surface energy and surface polarity of the designated regions on the substrate have been increased simultaneously, leading to a significant enhancement of directed self–assembly property. The effects of PVUV exposure and alkali rinsing to the surface modification have been explored systematically. The results confirm that the modification degree can be controlled precisely by simply adjusting the exposure time of PVUV exposure, suggesting potential adaptability in directed self–assembly of different functional suspensions onto a variety of soft substrates.

In *Chapter 4*, by utilizing the proposed DSA strategy, a directed self–assembled gold nanoparticle (AuNP) electrode has been demonstrated successfully with an unprecedentedly ultrahigh resolution of 600 nm. Directed self–assembled circuits in various shapes and sizes can be prepared facilely with suppressed coffee–ring effect and

long–term stability. Furthermore, the DSA process enables a layer–by–layer fabrication of additively manufactured organic thin–film transistors (OTFTs) with a short channel length of 1 μm, resulting in a large on–off ratio of 10^6 and high field–effect mobility of 0.5 $cm^2 V^{-1} s^{-1}$. These results firmly prove the effectiveness of the proposed DSA strategy toward soft electronic manufacturing.

In *Chapter 5*, the usage of the developed DSA strategy has been further expanded. Inspired by the obvious wetting/dewetting behavior of the DSA substrate, an innovative directed self–assembly strategy is proposed for patterning silver nanowires (AgNWs) into flexible transparent conductors (TCs) in a highly ordered manner using microflow velocity–field–induced spontaneous alignment. The self–assembled AgNW TCs with honeycomb–structured patterns exhibit ultrahigh transmittance (98.2%), low sheet resistance (29.7 Ω sq^{-1}), and prominent mechanical deformability. Moreover, the proposed strategy has been further applied to fabricate high–accuracy arbitrary AgNW circuits to realize flexible transparent heaters with adjustable localized heat sources. This is a universal and customizable method for patterning functional nanomaterials with almost no shape and dimension limitation, offering a promising prospect of liquid–mediated self–assembly technology in the manufacturing of advancing 2D or futuristic 3D soft electronics.

In *Chapter 6*, the summary of the thesis is presented.

Reference

[1] Z. Martin, The chips are down, Nature. 530 (2016) 145–147. https://doi.org/10.1038/nj6893–03a.

[2] Frey JW, C. M, Thin Silicon Solar Cells for Large Flexile Arrays, Nat. Publ. Gr. 213 (1967) 1223–1224. https://doi.org/10.1038/2131223a0.

[3] H. Shirakawa, E.J. Louis, A.G. MacDiarmid, C.K. Chiang, A.J. Heeger, Synthesis of electrically conducting organic polymers: Halogen derivatives of polyacetylene, (CH)x, J. Chem. Soc. Chem. Commun. (1977) 578–580. https://doi.org/10.1039/C39770000578.

[4] R.C. Chittick, J.H. Alexander, H.F. Sterling, The Preparation and Properties of Amorphous Silicon, J. Electrochem. Soc. 116 (1969) 77–81. https://doi.org/10.1149/1.2411779.

[5] J.H. Burroughes, C.A. Jones, R.H. Friend, New semiconductor device physics in polymer diodes and transistors, Nature. 335 (1988) 6186. https://doi.org/10.1038/335137a0.

[6] H.A. Klasens, H. Koelmans Reference, P.K. Weimer, A tin oxide field–effect transistor, Solid State Commun. 7 (1964) 701–702. https://doi.org/10.1016/0038–1101(64)90057–7.

[7] K. Nan, S.D. Kang, K. Li, K.J. Yu, F. Zhu, J. Wang, A.C. Dunn, C. Zhou, Z. Xie, M.T. Agne, H. Wang, H. Luan, Y. Zhang, Y. Huang, G.J. Snyder, J.A. Rogers, Compliant and stretchable thermoelectric coils for energy harvesting in miniature flexible devices, Sci. Adv. 4 (2018) eaau5849. https://doi.org/10.1126/sciadv.aau5849.

[8] J.Y. Oh, S. Rondeau–Gagné, Y.C. Chiu, A. Chortos, F. Lissel, G.J.N. Wang, B.C. Schroeder, T. Kurosawa, J. Lopez, T. Katsumata, J. Xu, C. Zhu, X. Gu, W.G. Bae, Y. Kim, L. Jin, J.W. Chung, J.B.H. Tok, Z. Bao, Intrinsically stretchable and healable semiconducting polymer for organic transistors, Nature. 539 (2016) 411–415. https://doi.org/10.1038/nature20102.

[9] K. Kim, Y.G. Park, B.G. Hyun, M. Choi, J.U. Park, Recent Advances in Transparent Electronics with

Stretchable Forms, Adv. Mater. 31 (2019) 1804690. https://doi.org/10.1002/adma.201804690.

[10] S. Choi, S.I. Han, D. Kim, T. Hyeon, D.H. Kim, High–performance stretchable conductive nanocomposites: Materials, processes, and device applications, Chem. Soc. Rev. 48 (2019) 1566–1595. https://doi.org/10.1039/c8cs00706c.

[11] H. Yuk, B. Lu, X. Zhao, Hydrogel bioelectronics, Chem. Soc. Rev. 48 (2019) 1642–1667. https://doi.org/10.1039/c8cs00595h.

[12] T. Kasuga, H. Yagyu, K. Uetani, H. Koga, M. Nogi, "return to the Soil" Nanopaper Sensor Device for Hyperdense Sensor Networks, ACS Appl. Mater. Interfaces. 11 (2019) 43488–43493. https://doi.org/10.1021/acsami.9b13886.

[13] S.K. Kang, J. Koo, Y.K. Lee, J.A. Rogers, Advanced Materials and Devices for Bioresorbable Electronics, Acc. Chem. Res. 51 (2018) 988–998. https://doi.org/10.1021/acs.accounts.7b00548.

[14] H. Ouyang, Z. Li, M. Gu, Y. Hu, L. Xu, D. Jiang, S. Cheng, Y. Zou, Y. Deng, B. Shi, W. Hua, Y. Fan, Z. Li, Z. Wang, A Bioresorbable Dynamic Pressure Sensor for Cardiovascular Postoperative Care, Adv. Mater. (2021) 2102302. https://doi.org/10.1002/adma.202102302.

[15] Z. Kuncic, T. Nakayama, Neuromorphic nanowire networks: principles, progress and future prospects for neuro–inspired information processing, Adv. Phys. X. 6 (2021) 1894234. https://doi.org/10.1080/23746149.2021.1894234.

[16] H. Kim, J. Gibson, J. Maeng, M.O. Saed, K. Pimentel, R.T. Rihani, J.J. Pancrazio, S. V. Georgakopoulos, T.H. Ware, Responsive, 3D Electronics Enabled by Liquid Crystal Elastomer Substrates, ACS Appl. Mater. Interfaces. 11 (2019) 19506–19513. https://doi.org/10.1021/acsami.9b04189.

[17] D. Corzo, G. Tostado–Blázquez, D. Baran, Flexible Electronics: Status, Challenges and Opportunities, Front. Electron. 1 (2020) 1–13. https://doi.org/10.3389/felec.2020.594003.

[18] W. Gao, S. Emaminejad, H.Y.Y. Nyein, S. Challa, K. Chen, A. Peck, H.M. Fahad, H. Ota, H. Shiraki, D. Kiriya, D.H. Lien, G.A. Brooks, R.W. Davis, A. Javey, Fully integrated wearable sensor arrays for multiplexed in situ perspiration analysis, Nature. 529 (2016) 509–514. https://doi.org/10.1038/nature16521.

[19] J.R. Windmiller, J. Wang, Wearable Electrochemical Sensors and Biosensors: A Review, Electroanalysis. 25 (2013) 29–46. https://doi.org/10.1002/elan.201200349.

[20] I.J. Park, T.I. Kim, T. Yoon, S. Kang, H. Cho, N.S. Cho, J.I. Lee, T.S. Kim, S.Y. Choi, Flexible and Transparent Graphene Electrode Architecture with Selective Defect Decoration for Organic Light–Emitting Diodes, Adv. Funct. Mater. (2018) 1704435. https://doi.org/10.1002/adfm.201704435.

[21] H.S. Jo, S. An, J.G. Lee, H.G. Park, S.S. Al–Deyab, A.L. Yarin, S.S. Yoon, Highly flexible, stretchable, patternable, transparent copper fiber heater on a complex 3D surface, NPG Asia Mater. 9 (2017) e347. https://doi.org/10.1038/am.2016.206.

[22] X. Zhu, J. Xu, F. Qin, Z. Yan, A. Guo, C. Kan, Highly efficient and stable transparent electromagnetic interference shielding films based on silver nanowires, Nanoscale. 12 (2020) 14589–14597. https://doi.org/10.1039/d0nr03790g.

[23] J. Kim, M. Lee, H.J. Shim, R. Ghaffari, H.R. Cho, D. Son, Y.H. Jung, M. Soh, C. Choi, S. Jung, K. Chu, D. Jeon, S.T. Lee, J.H. Kim, S.H. Choi, T. Hyeon, D.H. Kim, Stretchable silicon nanoribbon electronics for

skin prosthesis, Nat. Commun. 5 (2014). https://doi.org/10.1038/ncomms6747.

[24] N. Matsuhisa, D. Inoue, P. Zalar, H. Jin, Y. Matsuba, A. Itoh, T. Yokota, D. Hashizume, T. Someya, Printable elastic conductors by in situ formation of silver nanoparticles from silver flakes, Nat. Mater. 16 (2017) 834–840. https://doi.org/10.1038/nmat4904.

[25] H. Kim, S. kyun Ahn, D.M. Mackie, J. Kwon, S.H. Kim, C. Choi, Y.H. Moon, H.B. Lee, S.H. Ko, Shape morphing smart 3D actuator materials for micro soft robot, Mater. Today. 41 (2020) 243–269. https://doi.org/10.1016/j.mattod.2020.06.005.

[26] J.H. Seo, I. Hwang, H.D. Um, S. Lee, K. Lee, J. Park, H. Shin, T.H. Kwon, S.J. Kang, K. Seo, Cold Isostatic–Pressured Silver Nanowire Electrodes for Flexible Organic Solar Cells via Room–Temperature Processes, Adv. Mater. 29 (2017) 1701479. https://doi.org/10.1002/adma.201701479.

[27] J. Saghaei, A. Fallahzadeh, T. Saghaei, ITO–free organic solar cells using highly conductive phenol–treated PEDOT:PSS anodes, Org. Electron. Physics, Mater. Appl. 24 (2015) 188–194. https://doi.org/10.1016/j.orgel.2015.06.002.

[28] B.W. An, K. Kim, H. Lee, S.Y. Kim, Y. Shim, D.Y. Lee, J.Y. Song, J.U. Park, High–Resolution Printing of 3D Structures Using an Electrohydrodynamic Inkjet with Multiple Functional Inks, Adv. Mater. 27 (2015) 4322–4328. https://doi.org/10.1002/adma.201502092.

[29] Y. Wang, S. Lee, T. Yokota, H. Wang, Z. Jiang, J. Wang, M. Koizumi, T. Someya, A durable nanomesh on–skin strain gauge for natural skin motion monitoring with minimum mechanical constraints, Sci. Adv. 6 (2020) eabb7043. https://doi.org/10.1126/sciadv.abb7043.

[30] K. Kwon, J.U. Kim, Y. Deng, S.R. Krishnan, J. Choi, H. Jang, K.H. Lee, C.J. Su, I. Yoo, Y. Wu, L. Lipschultz, J.H. Kim, T.S. Chung, D. Wu, Y. Park, T. il Kim, R. Ghaffari, S. Lee, Y. Huang, J.A. Rogers, An on–skin platform for wireless monitoring of flow rate, cumulative loss and temperature of sweat in real time, Nat. Electron. 4 (2021) 302–312. https://doi.org/10.1038/s41928–021–00556–2.

[31] J.W. Park, B.H. Kang, H.J. Kim, A Review of Low–Temperature Solution–Processed Metal Oxide Thin–Film Transistors for Flexible Electronics, Adv. Funct. Mater. 1904632 (2019) 1904632. https://doi.org/10.1002/adfm.201904632.

[32] J.Z. Wang, Z.H. Zheng, H.W. Li, W.T.S. Huck, H. Sirringhaus, Dewetting of conducting polymer inkjet droplets on patterned surfaces, Nat. Mater. 3 (2004) 171–176. https://doi.org/10.1038/nmat1073.

[33] T. Kraus, L. Malaquin, H. Schmid, W. Riess, N.D. Spencer, H. Wolf, Nanoparticle printing with single–particle resolution, Nat. Nanotechnol. 2 (2007) 570–576. https://doi.org/10.1038/nnano.2007.262.

[34] J. Bae, J. Lee, Q. Zhou, T. Kim, Micro–/Nanofluidics for Liquid–Mediated Patterning of Hybrid–Scale Material Structures, Adv. Mater. 31 (2019) 1804953. https://doi.org/10.1002/adma.201804953.

[35] P.F. Moonen, I. Yakimets, J. Huskens, Fabrication of Transistors on Flexible Substrates: from Mass–Printing to High–Resolution Alternative Lithography Strategies, Adv. Mater. 24 (2012) 5526–5541. https://doi.org/10.1002/adma.201202949.

[36] K. Jain, S. Rice, B.J. Lin, Ultrafast deep UV lithography using excimer lasers, IEEE Electron Device Lett. 3 (1982) 53–55. https://doi.org/10.1002/pen.760231808.

[37] V. Pol, J.H. Bennewitz, T.E. Jewell, D.W. Peters, Excimer Laser Based Lithography: A Deep–Ultraviolet

Wafer Stepper For VLSI Processing, Opt. Eng. 26 (1987) 311–318. https://doi.org/10.1117/12.7974072.

[38] Y. Zhu, J. Tang, X. Jin, T. Pan, Y. Chang, Z. Yang, Additive Preparation of Conductive Circuit Based on Template Transfer Process Using a Reusable Photoresist, ACS Appl. Mater. Interfaces. 12 (2020) 7679–7689. https://doi.org/10.1021/acsami.9b17694.

[39] B. Zhu, S. Gong, W. Cheng, Softening gold for elastronics, Chem. Soc. Rev. 48 (2019) 1668–1711. https://doi.org/10.1039/c8cs00609a.

[40] Y. Chu, C. Qian, P. Chahal, C. Cao, Printed Diodes: Materials Processing, Fabrication, and Applications, Adv. Sci. 6 (2018) 1801653. https://doi.org/10.1002/advs.201801653.

[41] M.A.M. Leenen, V. Arning, H. Thiem, J. Steiger, R. Anselmann, Printable electronics: Flexibility for the future, Phys. Status Solidi Appl. Mater. Sci. 206 (2009) 588–597. https://doi.org/10.1002/pssa.200824428.

[42] R.D. Farahani, M. Dubé, D. Therriault, Three–Dimensional Printing of Multifunctional Nanocomposites: Manufacturing Techniques and Applications, Adv. Mater. 28 (2016) 5794–5821. https://doi.org/10.1002/adma.201506215.

[43] W. Wu, Inorganic Nanomaterials for Printed Electronics: A Review, Nanoscale. 9 (2017) 7342–7372. https://doi.org/10.1039/C7NR01604B.

[44] G. Grau, J. Cen, H. Kang, R. Kitsomboonloha, W.J. Scheideler, V. Subramanian, Gravure–printed electronics: Recent progress in tooling development, understanding of printing physics, and realization of printed devices, Flex. Print. Electron. 1 (2016) 023002. https://doi.org/10.1088/2058–8585/1/2/023002.

[45] E. Jabari, E. Toyserkani, Micro–scale aerosol–jet printing of graphene interconnects, Carbon N. Y. 91 (2015) 321–329. https://doi.org/10.1016/j.carbon.2015.04.094.

[46] H. Ding, Q. Zhang, H. Gu, X. Liu, L. Sun, M. Gu, Controlled Microstructural Architectures Based on Smart Fabrication StrategiesS, Adv. Funct. Mater. 30 (2020) 1901760. https://doi.org/10.1002/adfm.201901760.

[47] L. Malaquin, T. Kraus, H. Schmid, E. Delamarche, H. Wolf, Controlled particle placement through convective and capillary assembly, Langmuir. 23 (2007) 11513–11521. https://doi.org/10.1021/la700852c.

[48] C.M. Jin, W. Lee, D. Kim, T. Kang, I. Choi, Photothermal Convection Lithography for Rapid and Direct Assembly of Colloidal Plasmonic Nanoparticles on Generic Substrates, Small. 14 (2018) 1803055. https://doi.org/10.1002/smll.201803055.

[49] T. Minari, C. Liu, M. Kano, K. Tsukagoshi, Controlled Self–Assembly of Organic Semiconductors for Solution–Based Fabrication of Organic Field–Effect Transistors, Adv. Mater. 24 (2012) 299–306. https://doi.org/10.1002/adma.201102554.

[50] Q. Xie, G.B. Davies, J. Harting, Direct Assembly of Magnetic Janus Particles at a Droplet Interface, ACS Nano. 11 (2017) 11232–11239. https://doi.org/10.1021/acsnano.7b05550.

[51] J.M. Shapiro, B.W. Drinkwater, A.W. Perriman, M. Fraser, Sonolithography: In–Air Ultrasonic Particulate and Droplet Manipulation for Multiscale Surface Patterning, Adv. Mater. Technol. 6 (2021). https://doi.org/10.1002/admt.202000689.

[52] Z. Chai, J. Seo, S.A. Abbasi, A. Busnaina, Assembly of Highly Aligned Carbon Nanotubes Using an Electro–Fluidic Assembly Process, ACS Nano. 12 (2018) 12315–12323. https://doi.org/10.1021/acsnano.8b06176.

[53] Y. Huang, J. Zhou, B. Su, L. Shi, J. Wang, S. Chen, L. Wang, J. Zi, Y. Song, L. Jiang, Colloidal photonic crystals with narrow stopbands assembled from low–adhesive superhydrophobic substrates, J. Am. Chem. Soc. 134 (2012) 17053–17058. https://doi.org/10.1021/ja304751k.

[54] B. Bangalore Rajeeva, L. Lin, E.P. Perillo, X. Peng, W.W. Yu, A.K. Dunn, Y. Zheng, High–Resolution Bubble Printing of Quantum Dots, ACS Appl. Mater. Interfaces. 9 (2017) 16725–16733. https://doi.org/10.1021/acsami.7b04881.

[55] Z. Chai, S.A. Abbasi, A.A. Busnaina, Scalable Directed Assembly of Highly Crystalline 2,7–Dioctyl[1]benzothieno[3,2– b][1]benzothiophene (C8–BTBT) Films, ACS Appl. Mater. Interfaces. 10 (2018) 18123–18130. https://doi.org/10.1021/acsami.8b01433.

[56] Z. Chai, C. Yilmaz, A.A. Busnaina, C.A. Lissandrello, D.J.D. Carter, Directed assembly–based printing of homogeneous and hybrid nanorods using dielectrophoresis, Nanotechnology. 28 (2017) 475303. https://doi.org/10.1088/1361–6528/aa935f.

[57] J. Xiong, S. Li, J.H. Ciou, J. Chen, D. Gao, J. Wang, P.S. Lee, A Tailorable Spray–Assembly Strategy of Silver Nanowires–Bundle Mesh for Transferable High–Performance Transparent Conductor, Adv. Funct. Mater. (2020) 2006120. https://doi.org/10.1002/adfm.202006120.

[58] H. Zhang, J. Cadusch, C. Kinnear, T. James, A. Roberts, P. Mulvaney, Direct assembly of large area nanoparticle arrays, ACS Nano. 12 (2018) 7529–7537. https://doi.org/10.1021/acsnano.8b02932.

[59] V. Flauraud, M. Mastrangeli, G.D. Bernasconi, J. Butet, D.T.L. Alexander, E. Shahrabi, O.J.F. Martin, J. Brugger, Nanoscale topographical control of capillary assembly of nanoparticles, Nat. Nanotechnol. 12 (2017) 73–80. https://doi.org/10.1038/nnano.2016.179.

[60] J. Wang, L. Wang, Y. Song, L. Jiang, Patterned photonic crystals fabricated by inkjet printing, J. Mater. Chem. C. 1 (2013) 6048–6058. https://doi.org/10.1039/c3tc30728j.

[61] H. Ding, C. Zhu, L. Tian, C. Liu, G. Fu, L. Shang, Z. Gu, Structural Color Patterns by Electrohydrodynamic Jet Printed Photonic Crystals, ACS Appl. Mater. Interfaces. 9 (2017) 11933–11941. https://doi.org/10.1021/acsami.6b11409.

[62] J. Feng, X. Jiang, X. Yan, Y. Wu, B. Su, H. Fu, J. Yao, L. Jiang, "Capillary–Bridge Lithography" for Patterning Organic Crystals toward Mode–Tunable Microlaser Arrays, Adv. Mater. 29 (2017) 1–8. https://doi.org/10.1002/adma.201603652.

[63] J. Han, J. Yang, W. Gao, H. Bai, Ice–Templated, Large–Area Silver Nanowire Pattern for Flexible Transparent Electrode, Adv. Funct. Mater. 31 (2021) 2010155. https://doi.org/10.1002/adfm.202010155.

[64] B.R. Yang, W. Cao, G.S. Liu, H.J. Chen, Y.Y. Noh, T. Minari, H.C. Hsiao, C.Y. Lee, H.P.D. Shieh, C. Liu, Microchannel Wetting for Controllable Patterning and Alignment of Silver Nanowire with High Resolution, ACS Appl. Mater. Interfaces. 7 (2015) 21433–21441. https://doi.org/10.1021/acsami.5b06370.

[65] T. Tokuno, M. Nogi, J. Jiu, T. Sugahara, K. Suganuma, Transparent electrodes fabricated via the self–assembly of silver nanowires using a bubble template, Langmuir. 28 (2012) 9298–9302. https://doi.org/10.1021/la300961m.

[66] V. Sharma, A. Koivikko, K. Yiannacou, K. Lahtonen, V. Sariola, Flexible biodegradable transparent heaters based on fractal–like leaf skeletons, Npj Flex. Electron. 4 (2020) 27. https://doi.org/10.1038/s41528–020–

00091–8.

[67] B. Han, Y. Huang, R. Li, Q. Peng, J. Luo, K. Pei, A. Herczynski, K. Kempa, Z. Ren, J. Gao, Bio–inspired networks for optoelectronic applications, Nat. Commun. 5 (2014) 5674. https://doi.org/10.1038/ncomms6674.

[68] B. Han, K. Pei, Y. Huang, X. Zhang, Q. Rong, Q. Lin, Y. Guo, T. Sun, C. Guo, D. Carnahan, M. Giersig, Y. Wang, J. Gao, Z. Ren, K. Kempa, Uniform self–forming metallic network as a high–performance transparent conductive electrode, Adv. Mater. 26 (2014) 873–877. https://doi.org/10.1002/adma.201302950.

[69] J.H.M. Maurer, L. González–García, B. Reiser, I. Kanelidis, T. Kraus, Templated Self–Assembly of Ultrathin Gold Nanowires by Nanoimprinting for Transparent Flexible Electronics, Nano Lett. 16 (2016) 2921–2925. https://doi.org/10.1021/acs.nanolett.5b04319.

[70] Y. Li, C. Lv, Z. Li, D. Qu, Q. Zheng, From coffee rings to coffee eyes, Soft Matter. 11 (2015) 4669–4673. https://doi.org/10.1039/c5sm00654f.

[71] H. Zhang, A. Ramm, S. Lim, W. Xie, B.Y. Ahn, W.C. Xu, A. Mahajan, W.J. Suszynski, C. Kim, J.A. Lewis, C.D. Frisbie, L.F. Francis, Wettability Contrast Gravure Printing, Adv. Mater. 27 (2015) 7420–7425. https://doi.org/10.1002/adma.201502639.

[72] S.F. Shimobayashi, M. Tsudome, T. Kurimura, Suppression of the coffee–ring effect by sugar–assisted depinning of contact line, Sci. Rep. 8 (2018) 1–9. https://doi.org/10.1038/s41598–018–35998–w.

[73] X. Liu, M. Kanehara, C. Liu, T. Minari, Ultra–high–resolution printing of flexible organic thin–film transistors, J. Inf. Disp. 18 (2017) 93–99. https://doi.org/10.1080/15980316.2017.1298538.

[74] X. Liu, M. Kanehara, C. Liu, K. Sakamoto, T. Yasuda, J. Takeya, T. Minari, High–Resolution Electronics: Spontaneous Patterning of High–Resolution Electronics via Parallel Vacuum Ultraviolet, Adv. Mater. 28 (2016) 6568–6573. https://doi.org/10.1002/adma.201670218.

[75] K. Autumn, Y.A. Liang, S.T. Hsieh, W. Zesch, W.P. Chan, T.W. Kenny, R. Fearing, R.J. Full, Adhesive force of a single gecko foot–hair, Nature. 405 (2000) 681–685. https://doi.org/10.1038/35015073.

[76] L. Ge, S. Sethi, L. Ci, P.M. Ajayan, A. Dhinojwala, Carbon nanotube–based synthetic gecko tapes, Proc. Natl. Acad. Sci. U. S. A. 104 (2007) 10792–10795. https://doi.org/10.1073/pnas.0703505104.

Chapter 2

Experimental methods

2.1 Introduction

This chapter introduces detailed information about the experimental methods used in this study, which have been broadly divided into two sections: sample preparations and methods of characterizations. The first section enumerates the preparation processes, including the DSA strategy, the DSA–triggered high–resolution AuNP circuit and its related application of additively manufactured OTFT, and the DSA–triggered AgNW TC and its related application of arbitrary transparent heater. In the second section, the utilized characterization techniques in this study have been summarized and introduced. A few specific instruments and tools will be further explained in the following chapters.

2.2 Sample preparations

2.2.1 Preparation of dual–surface–architectonic (DSA) substrate

A flexible cyclic olefin polymer (COP, Zeon Corp., ZF–16) with a thickness of 100 μm was chosen as the substrate material owing to its hydrophobicity, moldability, and transparency. The COP substrate with an area of 4 × 4 cm^2 was then selectively irradiated by a parallel vacuum ultraviolet (PVUV) system under atmospheric condition through a contact photomask (150–200 nm, Ushio Inc., SUS740), which includes a PVUV excimer lamp with high energy (~695 kJ mol^{-1}) and mask aligner (**Figure 2.1**).[74] The area of the modified regions on the targeted substrate was depended on the exposure region of the PVUV light, which can be controlled by changing the pattern design of the photomask. The exposure time of PVUV was adjusted from 0 to 600 s to control the oxidation degree of the exposed substrates.

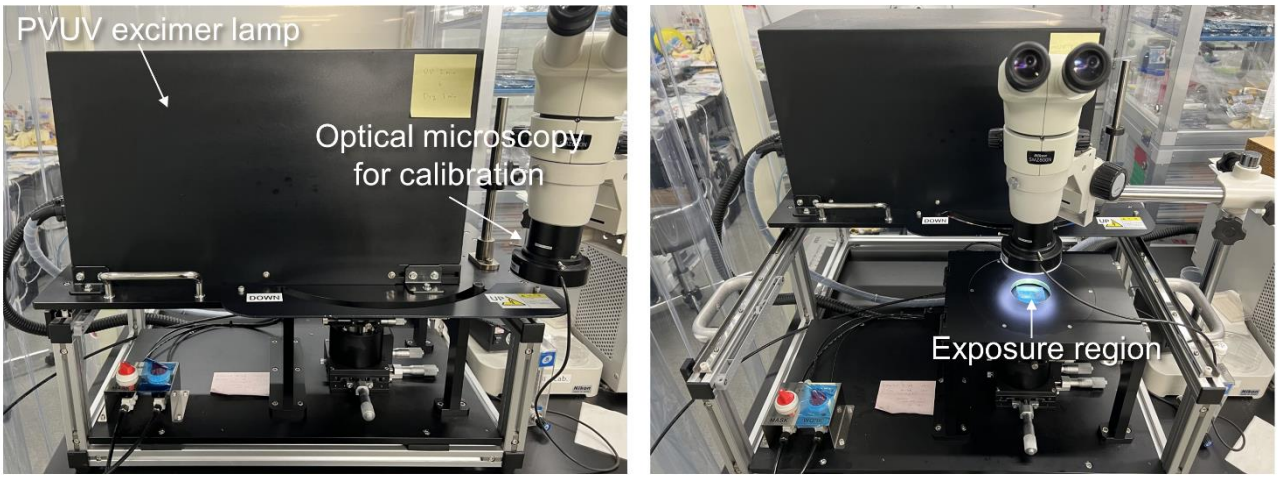

Figure 2.1 Digital images of the parallel vacuum ultraviolet (PVUV) system.

The obtained substrate was then immersed entirely into an alkaline solution (Okuno Chemical Industries Co., OPC–370 Condiclean, MA, pH 8.0) with a polyoxyethylene alkyl ether of 1.1 wt.% and an organic nitrogen

compound of 5 to 10 wt.% at 55 °C to rinse the surface. Different rinsing time ranging from 0 to 600 s was used to treat the irradiated sample for process optimization. Afterwards, the substrate was rinsed again with deionized water (ELGA water purification system, VWS (UK)) and dried thoroughly using a N_2 gas blower. Thus, we obtained the DSA substrate with selectively activated regions.

2.2.2 Spontaneous nanoscale patterning of gold nanoparticle (AuNP) circuits

For patterning conductive circuits, a π–junction AuNP ink (C–INK Co.) was employed owing to its room–temperature processability, long–term reliability and large work function of 4.69 eV. The prominent functionality is attributed to the conductive ligand using a derivative of metal–free phthalocyanine (**Figure 2.2**), which not only decreases the interparticle distance between AuNPs by the highly planer molecular structure for an enhanced electronic coupling, but also provides additional electrical pathways through the π orbitals of the aromatic ligand to lower the electrical percolation threshold.[77] The AuNP ink was spread over the DSA substrate via a common slit–coating process,[78–79] where it was spontaneously separated and assembled onto the activated regions on the DSA substrate. The swiping speed of the coating bar was 100 μm s^{-1}. Afterwards, the patterned functional AuNP ink was dried into complex electronic circuits directly under atmospheric conditions with no other post–treatment.

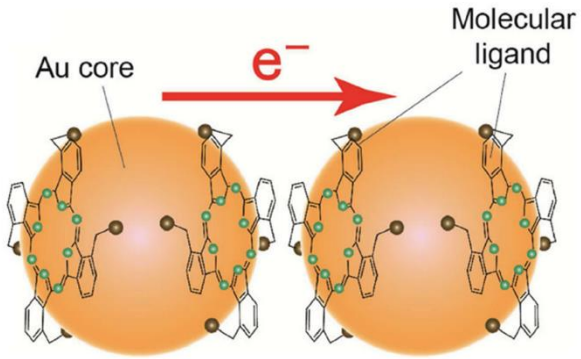

Figure 2.2 Schematic illustration of the utilized π–junction AuNPs.[77]

2.2.3 Fabrication of high–resolution organic thin–film transistor (OTFT) arrays

The staggered top–gate thin–film transistor (OTFT) was demonstrated on the obtained self–assembled AuNP circuit. After the DSA modification of the COP substrate, the functional AuNP ink was self–assembled and spontaneously formed into the high–resolution source (S)/drain (D) electrodes on the designated regions on the substrate. Prior to the solution casting of the semiconductor layer, a lyophobic guide layer of Cytop (Asahi Glass Co.) with a depth of 500 nm was formed as the bank arrays above the S/D electrodes via screen printing. An organic semiconductor solution prepared by dissolving hexyl–substituted dinaphtho[2,3–b:2',3'–d]thiophene derivative (C6–DNT–VW, JNC Petrochemical Corp.) in anisole (Fujifilm Wako Pure Chemical Corp.) at a concentration of 0.3 wt.% was cast into the banks and dried under ambient conditions. Afterwards, the guide layer was rinsed thoroughly with CT–Solv 180 solvent (Asahi Glass Co.), allowing the semiconductor layer to precisely crystallize on the channel region above the S/D electrodes. A dielectric layer of parylene–C (KISCO) with a thickness of 600 nm and a relative capacitance of approximately 3.0 nF cm^{-2} was coated over the entire substrate by chemical vapor deposition. Finally, the obtained sample was again treated using the proposed DSA strategy to define the top–gate

area above the integrated functional layers, followed by the slit–coating of AuNP ink to pattern the top–gate electrodes.

2.2.4 Spontaneous patterning of silver nanowire (AgNW) transparent conductors (TCs)

The AgNWs were dispersed in ultrapure water (Guangzhou Nano Chemical Technology Co.) at a concentration of 20 wt%. A series of AgNWs were used to adjust the liquid surface tension, which have the same average diameter of 50 nm and gradually increased average lengths of 5, 20, 50, and 100 μm. Before each use, a mild sonication for 2 min was carried out to prevent agglomeration of the AgNWs and ensure a uniform concentration distribution.

The DSA strategy was used again for the substrate preparation. In detail, the hydrophobic COP substrate (100 μm in thickness and 4 × 4 cm^2 in area) with a pristine low–surface–energy (γ_s^-) surface was irradiated by a selective PVUV exposure under a N_2 atmosphere. The exposure time was controlled from 0 to 1200 s to adjust the extent of oxidation. Afterwards, the PVUV–exposed substrate was rinsed with an alkaline solution and subsequently with deionized water to create the high–surface–energy (γ_s^+) region on the COP substrate. The activated substrate was dried thoroughly using a N_2 gas blower.

AgNW functional ink with 5 μL was deposited onto the DSA substrate and swiped over by a commercial slit–coating process. The swiping speed was adjusted according to the AgNW functional ink being used. In detail, the swiping speed of the coating bar was 10 cm s^{-1} for patterning the AgNWs with 50 μm in length, whereas the speed was changed to 5 cm s^{-1} and 15 cm s^{-1} in cases where the length of the AgNWs was 20 μm and 100 μm, respectively. The coated functional ink formed a cross–border overlayer above the DSA substrate irrespective of the surficial difference in the solid surface energy. Almost simultaneously, the dispersed AgNWs began to align themselves at the γ_s^- regions under the instantaneous flow field and spontaneously stacked layer–by–layer under the room–temperature evaporation flow (23 °C), resulting in the spontaneously patterned AgNW TCs with a cross–linked network structure.

Intense pulsed light (IPL) (PulseForge® Invent, NovaCentrix) was used to irradiate the as–prepared AgNW conductors to dry the residual moisture as well as compact the quasi–3D–stacked AgNW network (**Figure 2.3**). The reason we chose this technic is that IPL irradiation, as an optical sintering method, offers a broad–spectrum (200–1500 nm) pulse of white light to generate instantaneous (ten of microseconds) and strong local heat toward the surface of the object upon the light absorptivity. In the case of sintering AgNW TCs, IPL irradiation can heat AgNW network selectively stemming from the strong light absorption by AgNWs with less damage to the heat–sensitive transparent polymer substrate. The samples were placed 5 mm beneath the crystal filter light under ambient conditions. The optical energy from 0 to 1.5 J cm^{-2} was generated by adjusting the pulse duration from 100 to 150 μs, and the constant applied voltage from 600 to 750 V. With the appropriate control of the irradiation parameters, residual moisture among the AgNW network is expected to be evaporated, and the junctions of the quasi–3D stacked AgNW network could be sintered, leading to a rapid enhancement on the electrical conductivity without affecting the optical property of AgNW TCs.

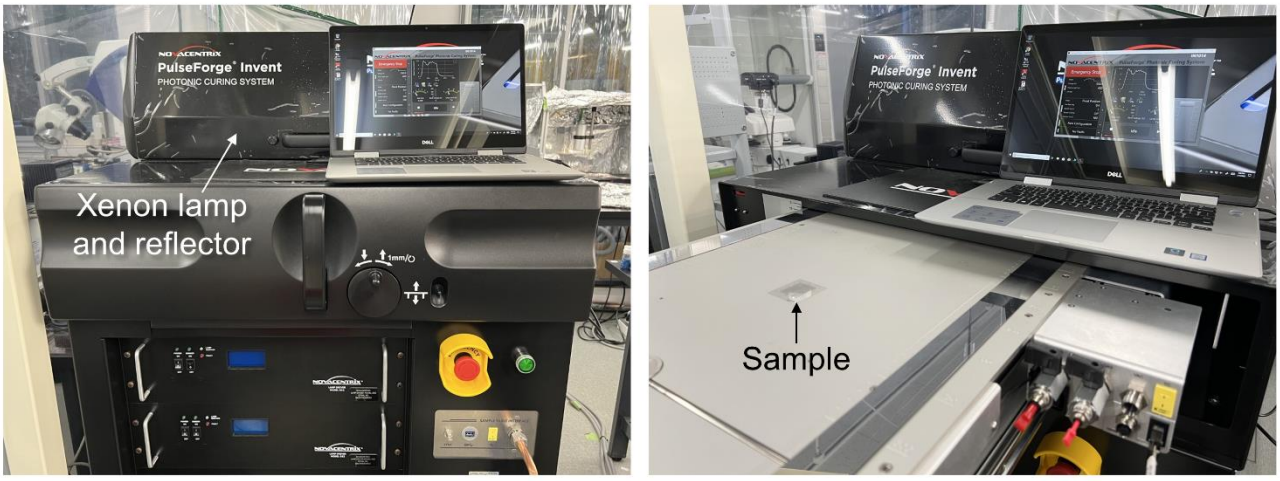

Figure 2.3. Digital images for Intense pulsed light (IPL) irradiation and the sample placement.

2.2.5 Fabrication of arbitrary AgNW–patterned transparent heaters

With the reasonable circuit design, the patterned AgNW circuits exhibited high transmittance and high flexibility, resulting in high–performance and customizable TCs. The patterned AgNW TCs with customized microstructures have been further tried to be used as flexible transparent heaters without post–treatment. The two ends of the samples were plastered with Cu foil tape (TERAOKA Co.) using silver nanoparticle (AgNP) paste (TK paste CR–2800, KAKEN TECH Co.) and then fixed by metal clamps to suppress the contact resistance (**Figure 2.4**). After a voltage was applied to the TCs (Benchtop DC Power Supply P4K–80, Matsusada Precision Inc.), the temperature evolution was recorded by a portable IR camera (sensitivity: 0.05 °C, 875–1i, testo Co.) with a fixed working distance.

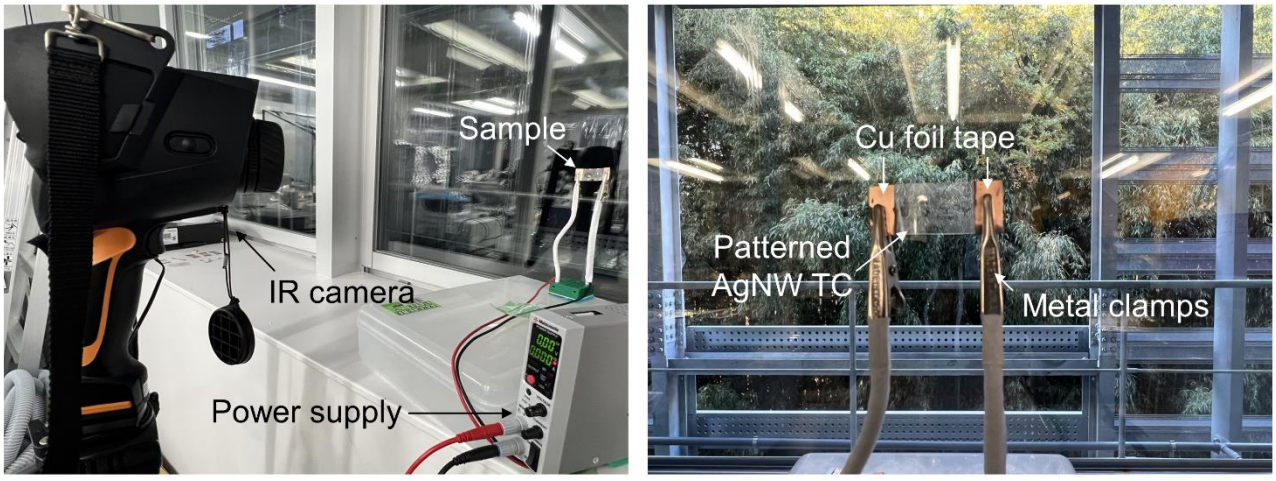

Figure 2.4. Digital image for the setting up for the AgNW–based transparent heater (left) and the sample fixation (right).

2.3 Methods of characterizations

2.3.1 Microscopic surface state characterizations during DSA strategy

The samples for surficial characterization were all prepared without the patterned photomask, in other words, the

homogenous DSA modification has been applied onto the COP substrate to avoid the localization issue. Furthermore, several parallel samples with multiple detection points have been prepared for ensuring the validity and reliability of the characterization results.

2.3.1.1 Physical characterizations

The morphologies of the modified substrate were observed using a digital optical microscope (OM, VHX–2000, Keyence Co.) and a field–emission scanning electron microscope (SEM, S–4800 EDX, Hitachi). The dimensions were obtained using a white–light interference microscope (VS1530, Hitachi). The configuration and the related height profile of the COP surface were explored using a scanning probe microscope with a dynamic force microscope (SPA400–DFM, Seiko Instruments).

2.3.1.2 Chemical characterizations

The surface chemical state was studied by X–ray photoelectron spectroscopy (XPS) with monochromatic Al–Kα radiation (20 W, 15 kV) (Quantum 2000, ULVAC–PHI, Inc.) and attenuated total reflectance Fourier transform infrared (ATF–FTIR) spectroscopy (Nicolet4700DR, Thermo Fisher Scientific).

2.3.2 Macroscopic surface state characterizations during DSA strategy

2.3.2.1 Solid surface energy evaluation

In this study, the solid surface energy was investigated by the contact angle, dyne test pen, and a model computation according to the equation of extended Fowkes. Because these three kinds of tools have respective characteristics and applicable scope, we can thus have a specified and comprehensive understanding of the solid surface states by utilizing these measurements flexibly.

Firstly, the contact angle was measured using a contact–angle analyzer (DMe–211, Kyowa Interface Science Co.) to provide a straightforward and rapid wettability evaluation of the modified substrates toward different kinds of functional solutions. Through depositing the functional droplet onto the substrate, the variation of the liquid surface tension of the functional ink affected by the solid surface energy and interfacial energy between liquid and solid at the three–phase contact line determines the drop shape, resulting in a measurable contact angle and disclosing the wettability relationship between the modified substrate and the specific solution.

Secondly, dyne test pens were utilized to quantify the solid surface energy directedly (EnerDyne Dyne Pens, Enercon Industries Co.). In detail, we used the dyne test pens, which inks are in a range of liquid surface tension values from 30 to 72 mJ m^{-2}, to draw across the different samples and observed the morphology changes of the remained Dyne test solution on the substrates. Through changing the use of the dyne pens with different liquid surface tension, the accurate solid surface energy can be read out when the dyne solution is held for exactly 4 s before the solution shrinks or draws back into droplets. The exact surface energy not only reveals the solid surface energy by the DSA strategy, but also contributes to the detailed quantitative calculation.

Thirdly, the variation of the solid surface energy has been further explored by the three–component model according to the extended Fowkes.[80–81] In this model, the surface energy has been divided into three individual interactions, including disperse fraction, dipole–dipole fraction, and hydrogen bridge bonding fraction. Through

measuring the contact angle of the different solutions on the modified substrates, the fraction change can be calculated, and the reason for inducing the surface state variation can be therefore clarified. The related information will be further explained in Section 3.2.4.

2.3.2.2 Sliding angle evaluation

To evaluate the surface adhesion of the substrate, the sliding angle values were measured using a contact–angle analyzer (Drop Master–SA–Cs1, Kyowa Interface Science Co.). In detail, the sample with the functional droplet was placed on an external tilting stage (maximum tilting angle: 90°). During the rotation of the tilting stage, the sliding angle, the critical angle that the deposited droplet begins to move, can be observed. At the same time, based on the captured image, the contact angle hysteresis can be obtained by calculating the difference between the advancing angle and receding angle for evaluating the surface adhesion force toward the functional solution over different substrates.

2.3.2.3 Liquid surface tension evaluation

The liquid surface tension has been detected by the pendant drop method using a contact analyzer (Drop Master–SA–Cs1, Kyowa Interface Science Co.). During the practical measurement, the detections started from capturing a shape profile of the functional drop hanging from a needle and followed by a subsequently numerical calculation via the built–in software.

2.3.3 Demonstrations of directed self–assembly property

To trigger the directed self–assembly, the designated regions on the targeted surface are expected to initially adsorb and firmly pin the dispersed functional materials. Therefore, we designed two different conditions to individually observe the capacities of selective adsorbing and selective pinning for a comprehensive evaluation. Particularly, water was selected to demonstrate the directed self–assembly property. This is because water has higher liquid surface tension than almost any other solution (72.8 mJ m^{-2} at 20 °C), which not only reduce evaporation rate to give plenty of time for liquid–mediated patterning of the dispersed functional materials but also gain easy adjustment toward the fluid flowing according to different solid surface states owing to its strong polarity. At the same time, the water–based inks with varying kinds of dispersed functional solutes are available in large quantities, which make water an ideal candidate for fundamental study of the designed directed self–assembly systems.

For the selective adsorbing property, a semi–modified substrate – half with pristine repellent surface and half with DSA modified surface – were prepared by using a half–covered photomask. Afterwards, water emitted from a syringe with a Teflon–coated needle (22G, Kyowa Interface Science Co.) was input onto the DSA substrate. The distance between the needle and the substrate was 1 mm. The liquid flow was recorded by a contact–angle analyzer (DMe–211, Kyowa Interface Science Co.).

For the selective pinning evaluation, a modified substrate with selectively patterned DSA regions was prepared. Water emitted from the syringe was then spread over the modified substrate. The distance between the needle and the substrate was decreased to 700 μm to ensure the continuous water flowing at a moving speed of 100 μm s^{-1}. The attracting and pinning behavior of the emitted water droplet affected by the variable surface energy states was

recorded and analyzed.

2.3.4 Experiment for coffee–ring demonstrative test

We used rhodamine–modified silica microparticles (AGC Si–Tech Co., SUNSPHERE NP–100) to intuitively observe and trace the flow of the dispersed solutes during room–temperature evaporation. The particle powder was dispersed in water at a concentration of 0.1 wt.%. During observation, 0.2 μL of the prepared solvent was deposited onto the substrate directly and dried under ambient conditions. The aggregation process of the silica microparticles drifted by the evaporative convection and the patterned structures after evaporation were *in–situ* recorded using a digital OM (VHX–2000, Keyence Co.).

2.3.5 Performance characterizations of self–assembled soft electronics

2.3.5.1 Physical performance evaluation

The morphologies of the patterned circuits and the patterning process were observed using a digital OM (VHX–2000, Keyence Co.) and a field–emission SEM (S–4800 EDX, Hitachi). The captured AgNW alignment was further analyzed by particle image velocimetry (FLOW–PIV, Library Co.) for microflow velocity analysis. The orientation analysis of the aligned AgNWs was conducted using the OrientationJ plug–in for the ImageJ software.[82] The transmittance was measured using a UV–visible near–infrared spectrophotometer (UV–2600, SHIMADZU Co.). The haze factor was determined using a UV–visible near–infrared spectrophotometer (SolidSpec–3700, SHIMADZU Co.).

2.3.5.2 Electrical performance evaluation

The conductivity of the patterned AuNP lines and the electric performances of the assembled OTFT transistors were tested using a vacuum prober station (Nagase Techno–Engineering Co.) and a semiconductor parameter analyzer (B1500A, Agilent Technologies) (**Figure 2.5**). The resistivity (ρ) was used to characterize the conductivity according to Equation 2.1:

$$\rho = R\frac{A}{l} \tag{2.1}$$

where R is the electrical resistance, A is the cross–sectional area, and l is the length of the printed lines.

Figure 2.5. Digital image for vacuum prober station.

The charge–carrier mobility (μ) of the additively manufactured OTFTs was calculated in the saturation regime according to Equation 2.2:

$$\mu = \frac{2L}{WC_{\mathrm{i}}}\left(\frac{\sqrt{I_{\mathrm{ds}}}}{V_{\mathrm{gs}}-V_{\mathrm{th}}}\right)^2 \tag{2.2}$$

where L and W are the length and width of the channel region, C_{i} is the capacitance per unit area of dielectric layer, I_{ds} is the source–drain current, V_{gs} is the gate voltage, and V_{th} is the threshold voltage.

The sheet resistance of the AgNW TCs was measured by a four–probe analysis with a surface resistivity meter (Lorestra–GP, MCP–T610, Mitsubishi Chemical Co.). The bending test was performed on a desktop–model endurance test machine (DMLHB–FS, Tension–FreeTM U–shape Folding Test, YUASA SYSTEM Co.) at a speed of 10 rounds min^{-1} with a bending radius of 7.5 mm. The variation in the relative resistance was recorded in time by a resistance meter (RM3545–02, HIOKI Co.).

Reference

[74] X. Liu, M. Kanehara, C. Liu, K. Sakamoto, T. Yasuda, J. Takeya, T. Minari, High–Resolution Electronics: Spontaneous Patterning of High–Resolution Electronics via Parallel Vacuum Ultraviolet, Adv. Mater. 28 (2016) 6568–6573. https://doi.org/10.1002/adma.201670218.

[77] T. Minari, Y. Kanehara, C. Liu, K. Sakamoto, T. Yasuda, A. Yaguchi, S. Tsukada, K. Kashizaki, M. Kanehara, Room–temperature printing of organic thin–film transistors with π–junction gold nanoparticles, Adv. Funct. Mater. 24 (2014) 4886–4892. https://doi.org/10.1002/adfm.201400169.

[78] M. Kanehara, J. Takeya, T. Uemura, H. Murata, K. Takimiya, H. Sekine, T. Terannishi, Electroconductive π–Junction Au Nanoparticles, Bull. Chem. Soc. Jpn. 85 (2012) 957–961. https://doi.org/10.1246/bcsj.20120103.

[79] D. Khim, H. Han, K. Baeg, J. Kim, S. Kwak, D. Kim, Y. Noh, Simple Bar–Coating Process for Large–Area ,

High– Performance Organic Field–Effect Transistors and Ambipolar Complementary Integrated Circuits, Adv. Mater. 25 (2013) 4302–4308. https://doi.org/10.1002/adma.201205330.

[80] J.R. Chen, T. Wakida, Studies on the surface free energy and surface structure of PTFE film treated with low temperature plasma, J. Appl. Polym. Sci. 63 (1997) 1733–1739. https://doi.org/https://doi.org/10.1002/(SICI)1097–4628(19970328)63:13<1733::AID–APP4>3.0.CO;2–H.

[81] F.M. Fowkes, Attractive Forces at Interfaces, Ind. Eng. Chem. 56 (1964) 40–52. https://doi.org/10.1109/CHICC.2008.4605198.

[82] A. Takemoto, T. Araki, T. Uemura, Y. Noda, S. Yoshimoto, S. Izumi, S. Tsuruta, T. Sekitani, Printable Transparent Microelectrodes toward Mechanically and Visually Imperceptible Electronics, Adv. Intell. Syst. (2020) 2000093. https://doi.org/10.1002/aisy.202000093.

Chapter 3

DSA strategy for liquid–mediated directed self–assembly

3.1 Introduction

Self–assembly patterning driven by a difference in the surface free energies (γ_s) of substrates is attracting increasing attention in the field of additively manufactured electronics.[34,83–84] Modified hydrophobic and hydrophilic regions on the surface can effectively guide fluidic inks to flow onto the designated regions spontaneously and result in the directly self–assembled functional patterns.[49] The benefits of this process include facile operation, low equipment requirements, and large–scale producibility; as such, there is enormous potential for the fabrication of electronic devices, i.e., large–area organic photodiodes,[85] disposable sensors,[86–87] and flexible OTFTs.[88]

However, thus far, the practical applicability of self–assembly patterning has been severely limited because the achievable resolution is lower than those fabricated by conventional lithography technologies.[40,43] This lack of high–resolution performance can be attributed to the difference in the γ_s between the designated regions and the substrate diminishing with decreasing the pattern size, which results in a lower driving force to trigger the self–assembly. At the same time, the aggravated horizontal Laplace pressure caused by the shrinkage of the substrate–ink interface produces an upward pressure that pushes the ink away from the substrate.[89–90] Diverging from the prevailing studies based on honing the difference between hydrophilicity and hydrophobicity, we conceive that the directed self–assembly process driven merely by modifying the γ_s contrast may not be sufficient for spontaneously patterning functional structures with higher resolution.

In this chapter, we report a DSA strategy, where the γ_s as well as the surface adhesion force (F_A) are found to be the critical factors for facilitating the directed self–assembly technology. We developed a two–step process to selectively create hydrophilic regions with enhanced polarity, leading to the simultaneous improvement of both γ_s and F_A with a remarkable wetting–pinning effect toward the functional inks. The premise of our strategy is to transform the designated regions *in situ* from the pristine substrate with an ultrahigh–resolution, provide strong shear stresses to attract fluidic selectively, and pin fluid firmly to accomplish the high–resolution and high–performance directed self–assembly. We expect the proposed strategy can lay a firm and versatile foundation for promoting the development of liquid–mediated additively manufacturing technology.

3.2 Results and discussion

3.2.1 Design principles for DSA with selective adsorbing and pinning properties

The DSA substrate for high–resolution self–assembly was designed according to the following three criteria: (1) the pristine substrate should repel fluidic ink; (2) the ink should flow preferentially to the designated regions; and (3) the ink should be firmly pinned onto the designated regions. The first criterion can be satisfied by using

hydrophobic polymer substrates, which tend to provide a low γ_s and therefore repel the fluidic ink.[91]

To satisfy the second criterion, we compared the total interfacial energies per unit area between the repellent region (E_A) and the designated region after depositing a liquid onto them. The key point to trigger the selective adsorbing is that the interfacial energy of the designated region (E_B) must be lower than that of the repellent region (E_A), so that the deposited ink can flow toward the designated region preferentially. Therefore, we analyze the change of the total interfacial energy at the individual area on a simplified surface (**Figure 3.1**). Configuration A refers to the repellent state where the liquid moves freely, and Configuration B refers to the designated state where the liquid can be adsorbed. The idea here is to find that Configuration B provides a lower interfacial energy state than that of Configuration A, so that the liquid is prone to gathering from Configuration A to Configuration B. By comparing these two states, we could quantify the difference to ensure the self–assembly patterning can be triggered.

In the below figure, E_A and E_B represent the total interfacial energy per unit area of Configuration A and B. In detail, R_f represents the roughness factor of the textured solid, which is defined as the ratio of the actual to the projected surface area. γ_{AL}, γ_{BL}, and γ_L represent the interfacial energy of the Liquid–Solid A, Liquid–Solid B, and liquid surface tension, respectively.

The following assumptions are proposed to derive the working condition: 1) the thickness of the liquid is much less than the capillary length of the liquid; 2) the surface roughness and the surface energy are uniformly distributed in both configurations; 3) the width of the unit area is much smaller compared with the width of solid–liquid interface in both area ($L<L_A<L_B$), in other words, the liquid is covered on the investigated surface entirely in each configuration.

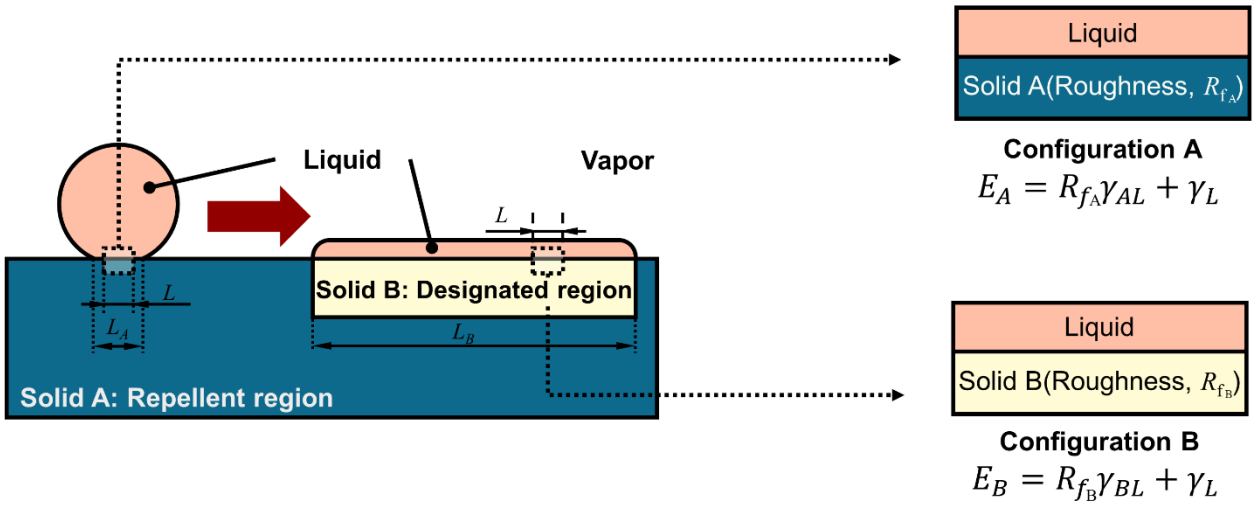

Figure 3.1. Derivation of the working conditions for selective adsorbing.

To find the condition that the Configuration B has the lower surface energy state than Configuration A, we have $\Delta E = E_A - E_B > 0$, which can be referred to,

$$\Delta E = R_{f_A}\gamma_{AL} - R_{f_B}\gamma_{BL} > 0 \qquad \text{(Equation 3.1)}$$

The variables of Equation 3.1 can be further converted according to Young's relation,[92–93] which can be expressed as,

$$\gamma_{SV} = \gamma_{SL} + \gamma_{LV}cos\theta \qquad \text{(Equation 3.2)}$$

where γ_{SV}, γ_{SL}, and γ_{LV} represent the interfacial energies of solid–vapor, solid–liquid, and liquid–vapor interfaces. Also, θ represents the contact angle of the deposited liquid on the solid surface.

By transforming Equation 3.1 into a measurable form using Equation 2.2, we have,

$$\Delta E = (\gamma_{AV} - \gamma_{LV}cos\theta_A)R_{f_A} + (\gamma_{LV}cos\theta_B - \gamma_{BV})R_{f_B} > 0 \qquad \text{(Equation 3.3)}$$

where γ_{AV} and γ_{BV} are the solid surface energy of the repellent region (A) and the designated region (B), respectively, θ_A and θ_B are the contact angles of the liquid on the corresponding surfaces, γ_{LV} is the liquid surface tension, and R_{fA} and R_{fB} are the corresponding roughness factors (the ratio between the actual and projected surface areas). According to Equation 3.3, the difference in γ_s can be increased by maintaining a high surface roughness (high R_f) on both regions and decreasing the contact angle of the designated region (low θ_B), which will drive the liquid to flow into the designated regions.

Regarding the third criterion, to guarantee the designated region (Configuration B) exhibits higher adhesive force (F_A) than that of the repellent region (Configuration A), the deposited liquid is expected to roll off at the repellent region and be pinned at the designated region along the tilted substrate (**Figure 3.2**).[94] Thus, we introduce the sliding angle (α) to quantify the pinning behaviors, which stands for the critical angle of inclination.[95] It has been demonstrated that the width of the drop (ω), γ_{LV}, the gravity of the deposited liquid, and the contact angle difference between the advancing angle (θ_{adv}) and the receding angle (θ_{rec}) of the liquid on the designated region determine the sliding angle by,[96–97]

$$\sin(\alpha) = \gamma_{LV}\frac{k\omega}{mg}(\cos\theta_{rec} - \cos\theta_{adv}) \qquad \text{(Equation 3.4)}$$

where m is the mass of the liquid; g is the gravitational acceleration; and k is the dimensionless factor, which can be further calculated to be between 1/2 and π/2.

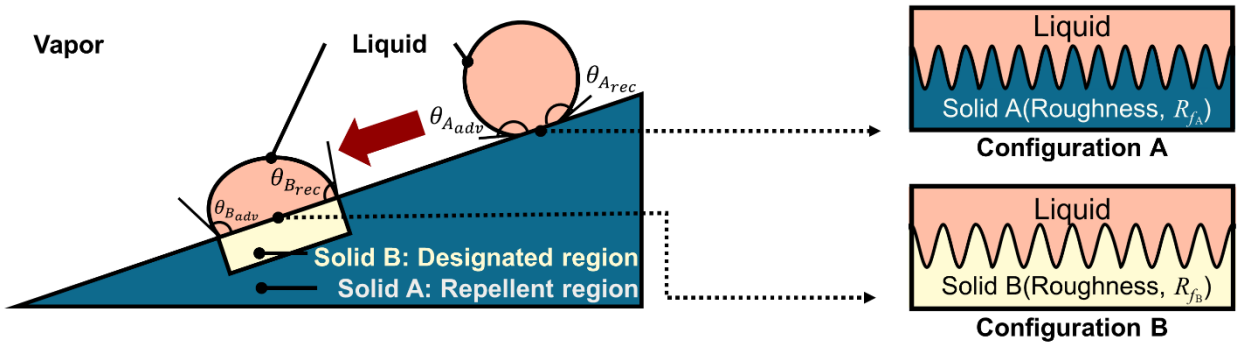

Figure 3.2. Derivation of the working conditions for fluidic pinning.

To derive the working condition, the surface textures are assumed to be uniform in each region. According to Equation 3.4, the solid surfaces are designed into the configurations with homogenous protuberances (**Figure 3.2, right**) for achieving the large γ_s contrast. Considering the ultrahigh–resolution printing, the repellent region seeks to avoid the excessively low–surface–energy materials forming Cassie–Baxter liquid–solid interface, in another word, the configurations of liquid–solid interfaces are all Wenzel states in this study.

Under the own gravity, the deposited liquid is supposed to move down the repellent surface at a slightly tilted angle while standing still on the designated surface even at a large–tilted angle. Therefore, we have $\Delta\alpha=\alpha_B-\alpha_A>0$,

which can be expressed as,

$$\Delta\alpha = \omega_B(\cos\theta_{rec} - \cos\theta_{adv})_B - \omega_A(\cos\theta_{rec} - \cos\theta_{adv})_A > 0 \qquad \text{(Equation 3.5)}$$

where ω_A and ω_B are the widths of the deposited liquid on the repellent and designated surfaces, respectively. According to Equation 3.5, we elucidate that a large liquid width (ω_B) and high contact angle hysteresis ($cah = \theta_{adv} - \theta_{rec}$) of the designated regions are the two main indicators for imparting the designated regions with high F_A.

3.2.2 Two–step modification of cyclic olefin polymer (COP) for DSA substrate preparation

On the basis of the defined principles, we fabricated the DSA substrate with large γ_s and F_A contrast to realize ultrahigh–resolution spontaneous patterning. COP was selected as the homogenous repellent (HR) substrate material to take advantage of its low γ_s, high surface roughness, and, most importantly, huge potential for surface modification and micromachining (**Figure 3.3(i)**).[98] The substrate was then exposed selectively to PVUV exposure through a photomask to increase the local γ_s and to obtain the surface–architectonic (SA) substrate (**Figure 3.3(ii)**). The PVUV system can generate precise well–collimated incident light, which yields submicron arrays of irradiated domains on the substrate and leads to efficient surficial oxidization. The SA substrate was further rinsed with an alkali solution to partially remove the oxidized moieties and increase the surface polarity, resulting in a DSA substrate with further enhanced surface adhesion force (**Figure 3.3(iii)**).

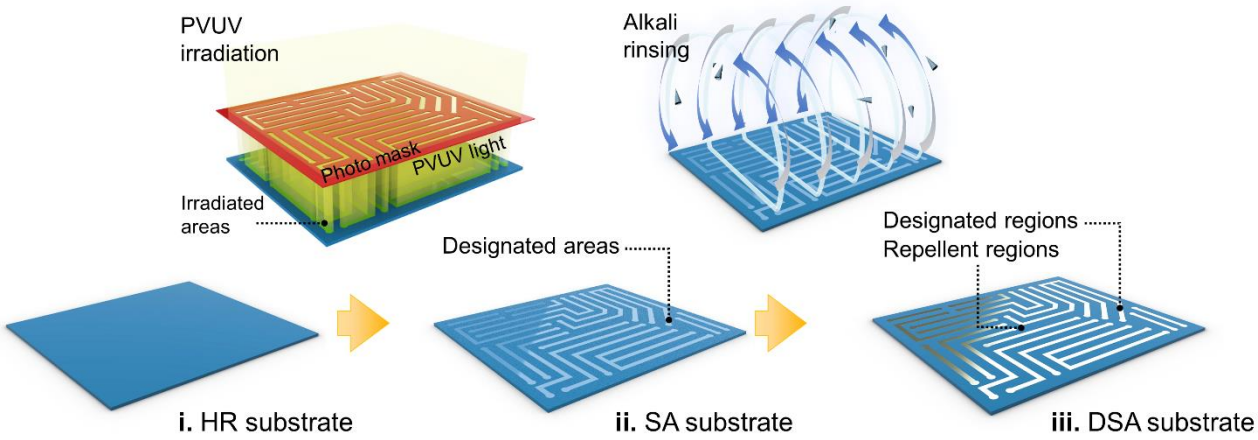

Figure 3.3. Schematic depicting the manufacturing process from (i) the homogenous repellent (HR) substrate to (ii) the surface architectonic (SA) substrate to (iii) the dual–surface–architectonics (DSA) substrate.

3.2.3 Characterizations of surface chemical states

The variations of surface states via DSA strategy were explored with the macroscopic examination and chemical composition analyses. The contact angle was observed to substantially decrease from 100.5° to 51.5° with an increasing sliding angle from 42.0° to 58.1° (**Figure 3.4 a and b**), indicating that both γ_s and F_A were enhanced.[99] After the SA substrate was further rinsed with an alkali solution, even though the contact angle remained unchanged, the sliding angle improved from 58.1° to 90°, which is the maximum measurable value (**Figure 3.4 a and b**). At the same time, a continuous increase of the *cah* from 14.2 to 29.5° was achieved during the DSA process (**Figure 3.4 b insets**). The observation indicates that the alkali rinsing strengthened the F_A significantly without dampening the enhanced γ_s.

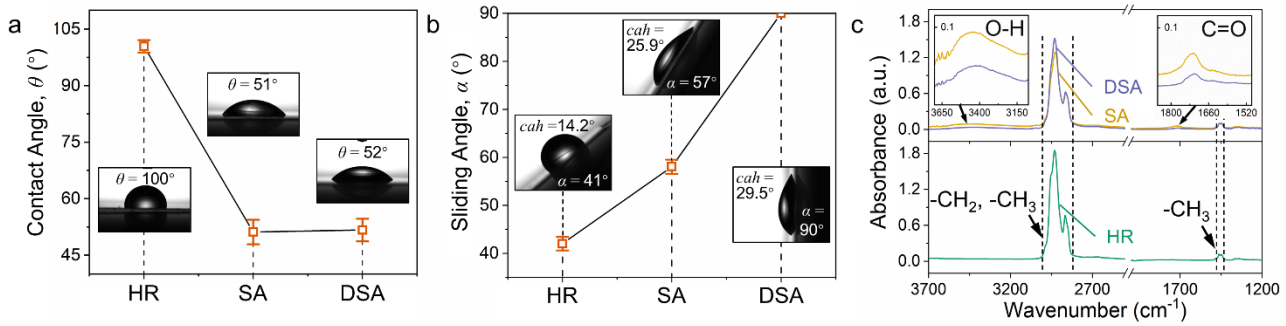

Figure 3.4. (a) Temporal dependence of the characteristic contact angle (θ) profiles. Insets show the corresponding θ measured with a 5.0 μL droplet. (b) Temporal dependence of the characteristic sliding angle (α) profiles. Insets show the corresponding α and contact angle hysteresis (*cah*) measured with a 1.0 μL droplet. Error bars in both (a) and (b) indicate the standard deviations from five independent samples. (c) Comparison of the attenuated total reflectance Fourier transform infrared (ATR–FTIR) spectra of the HR, SA, and DSA surfaces.

As shown in the characterizations of the surface chemical status by ATR–FTIR spectroscopy, the bands in the spectra of HR substrate, including the wagging mode of $–CH_3$ at 1447 cm^{-1} and the $–CH_3$ and $–CH_2$ stretches at 2868 and 2947 cm^{-1}, decreased in intensity after PVUV irradiation. The decrease was accompanied by the appearance of oxygen polar functional groups (OPFGs), including the carbonyl (C=O) stretching band from 1500 to 1850 cm^{-1} and a broad hydroxyl (H–O) stretching band from 3075 to 3700 cm^{-1} (**Figure 3.4 c**).[100–101] These results indicate that the PVUV exposure can disrupt the oxygen–free bonds and induce oxidation of the substrate, leading to a change in the surface structure and to increases of the γ_s and the F_A.

The intensities of both the carbonyl and hydroxyl peaks in the ATR–FTIR spectra decreased after alkali rinsing, which indicates that the partial OPFGs were removed by the scission of the photo–oxidized/photocleaved SA substrate. Closer inspection (**the right inset of Figure 3.4 c**) reveals that the carbonyl bands were slightly red–shifted, indicating that the carboxyl groups (1780–1710 cm^{-1}) were partially substituted with electron–donating groups.[102–103] Combing the decrease in intensity of the hydroxyl bands (**the left inset in Figure 3.4 c**), these results suggest that hydrogen cations were likely dissociated from the carboxyl groups via alkali neutralization, leading to a polarity enhancement and a strong F_A.[104–105]

The surface chemical states were further analyzed by XPS, as shown in **Figure 3.5**. For the HR substrate, only non–oxygenated carbon bonds (C–C/C–H at 284.8 eV) can be detected. After PVUV exposure, a clear oxygen peak (O 1s) began to appear, which comprised the peaks of OPFGs, including hydroxyl (C–O, 286.2 eV), carbonyl (C=O, 288.1 eV), and carboxyl (COOH, 289.1 eV). The variation illustrates that the optical energy of PVUV was sufficient to disrupt the oxygen–free bonds (C–C= 348 kJ mol^{-1} and C–H= 413 kJ mol^{-1}) and arouse the oxidization on the COP substrate.[106] After alkali rinsing, the share of the OPFGs decreases from 35.3 to 28.4 %, which indicates the cleavage and removal of the oxidized moieties. In detail, the share of carboxyl dropped off significantly compared to the hydroxyl and carbonyl, which suggests the disbands of the hydrogen cations in the hydroxyl band via alkali neutralization.

Overall, the results of these chemical composition analyses indicate that the proposed DSA strategy not only triggered the selective oxidation, but also implied that the surface polarization was progressed on the PVUV–

irradiated regions via alkali neutralization with no effect on the non–modified regions.

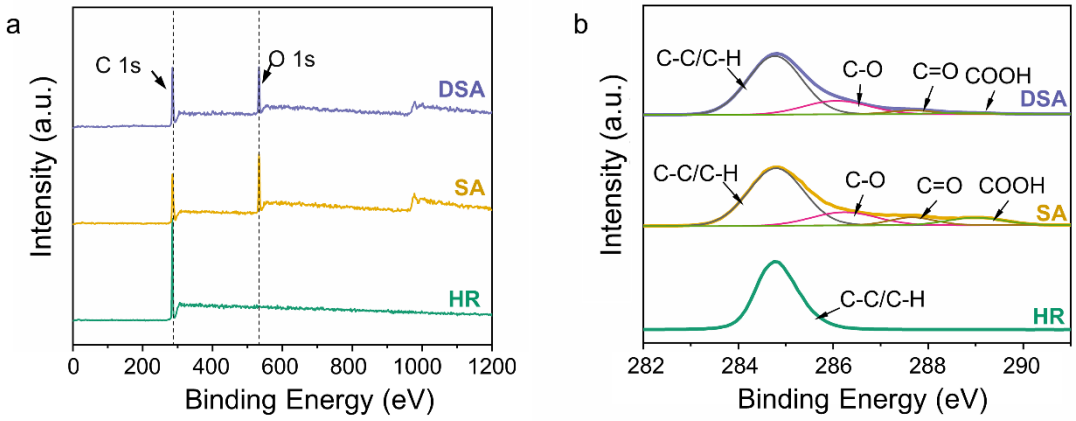

Figure 3.5. Comparison of X–ray photoelectron spectroscopy (XPS) (a) wide–scan and (b) C 1s spectra (right) of the HR, SA, and DSA surfaces.

3.2.4 Surface adhesion analysis via interfacial interaction analysis

Interfacial interaction analysis was carried out to evaluate the changes in the surface polarity during the DSA process (**Figure 3.6**). Based on the model of extended Fowkes, the liquid–solid interfacial tension (attracting force) can be studied according to the sum of the γ_s, which is further split up into three individual interactions, including the disperse fraction (γ_s^d), the dipole–dipole fraction (γ_s^p), and the hydrogen bridge bonding fraction (γ_s^h).[81]

The disperse interaction, also known as the London dispersion force, is a temporary attractive force that can be found in everything, occurring when one molecule, typically non–polar at the beginning, forms a temporary dipole and then creates an induced dipole in another molecule. Because the disperse interactions are temporary, they are weaker than the other two permanent polar intermolecular interactions. When the surface of the substrate becomes polar, the dipole–dipole interactions occur, and the positive side (δ^+) of either substrate or functional ink can be attracted to the negative side (δ^-) of another. The large electronegativity difference between electron–deficient and electron–rich components strengthens the presented attraction force. Hydrogen bridge bonding interaction, also known as hydrogen bonding interaction, is a kind of specific dipole–dipole interaction. It only occurs when the partially positive hydrogen atom is attracted to the negative atom of nitrogen, oxygen, and fluorine. Notably, the electronegativity difference is very large due to the combined effect of high electronegativity and small size of the above atoms. Therefore, hydrogen bridge bonding is more polarizable and has a stronger electrostatic force than the other dipole–dipole bonding, predominating liquid–solid interfacial interaction. The relationship among these interactions can be summarized as geometric mean values:

$$\gamma_{ls} = \gamma_l + \gamma_s - 2\left(\sqrt{\gamma_l^d \cdot \gamma_s^d} + \sqrt{\gamma_l^p \cdot \gamma_s^p} + \sqrt{\gamma_l^h \cdot \gamma_s^h}\right) \quad \text{(Equation 3.6)}$$

where γ_{ls} represents the liquid–solid interfacial interaction, and γ_l and γ_s represent the surface energy of the liquid and solid phases. γ_l^d, γ_l^p, γ_l^h, and γ_s^d, γ_s^p, γ_s^h refer to the disperse, dipole–dipole, and hydrogen bridge bonding interactions for the liquid and solid phases, respectively.

By convert the interfacial interactions between solid–liquid phases by Young's relation (Equation 3.2), the equation can be converted into:

$$\gamma_l(1 + \cos\theta) = 2\left(\sqrt{\gamma_l^d \cdot \gamma_s^d} + \sqrt{\gamma_l^p \cdot \gamma_s^p} + \sqrt{\gamma_l^h \cdot \gamma_s^h}\right) \quad \text{(Equation 3.7)}$$

in which, θ represents the contact angle of the deposited test liquid on the solid surfaces with different modified states. Accordingly, three test liquids, water, glycerin, and ethylene glycol (EG) were selected to deposit on the substrates for measuring the contact angles. **Table 3.1** summarizes the parameter information of the test liquids and the measured results.[80] In this case, each sample was measured at five different points and three parallel samples were utilized for determining the average values.

Table 3.1. Surface tensions of test liquids and measured contact angles.

	Liquid surface tension ($\times 10^{-5}$ N cm^{-1})				**Measured contact angle (°)**		
	γ	γ^d	γ^p	γ^h	HR substrate	SA substrate	DSA substrate
Water	72.8	29.1	1.3	42.4	99.8±1.0	49.5±0.7	49.6±0.9
Glycerin	63.4	37.4	0.2	25.8	85.3±1.6	41.7±2.5	45.8±1.2
EG	47.7	30.1	0	17.6	73.2±1.2	8.4±1.5	22.9±0.6

After putting the relevant parameters into Equation 3.7, the results were calculated and present in **Figure 3.6 a**. We have only found the non–polar disperse fraction on the HR substrate, verifying the weak liquids–solid interfacial interaction on the hydrophobic COP substrate. After PVUV irradiation, the disperse fraction was observed to be decreased, and the hydrogen bridge bonding fraction began to appear on the SA substrate. This can be attributed to the photo–oxidization by PVUV irradiation, which generated OPFGs on the surface and therefore produced the electrostatic force on the SA substrate. Strikingly, even though the surface energy remains unchanged after alkali rinsing, the hydrogen bridge bonding fraction was further increased with the rapid decrease of the disperse fraction. This variation can be explained by the neutralization with photo–induced carboxyl groups during alkali rinsing, which converted the carboxyl groups into carboxylate anions (COO^-) and further widened the electronegativity difference.

The expected change in molecular structures of the modified substrate has been presented in **Figure 3.6 b**. It is worth mentioning that we use pure water molecules in the schematics to illustrate the solid–liquid interfacial interaction generally. In the actual self–assembly systems using different functional inks, the effect of the solutes toward liquid surface tension as well as the polarity of the utilized solvent requires additional consideration. After exposing the HR substrate using PVUV, the OPFGs, including carboxyl (as shown in the schematic), hydroxyl, and carbonyl, generate on the SA substrate, which pull the water molecules toward the substrate via the formation of interfacial hydrogen bridge bonds. After further alkali rinsing, the negatively charged carboxylate anions with higher electronegativity (δ^{--}) can be achieved, which convert the hydrogen bridge bonding interactions into ion–dipole interactions and provide superior attraction force between the liquid and solid phases. The results of the interfacial interaction analysis reveal that intense surface polarization can be achieved by the DSA strategy, leading to the F_A improvement.

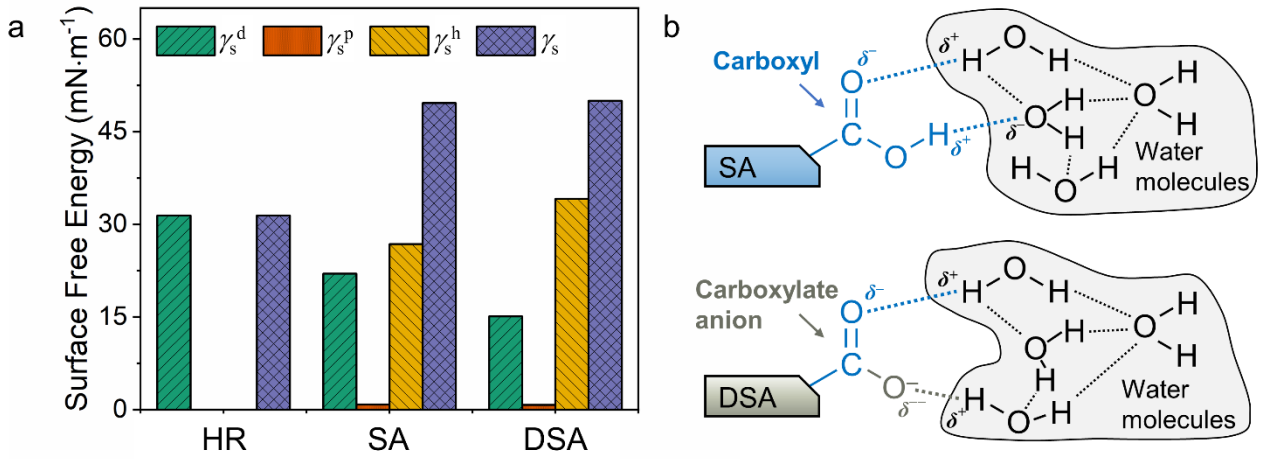

Figure 3.6. (a) Interfacial interaction analysis between solid and liquid phases based on the extended Fowkes model. (b) Schematic depicting the interfacial interactions between water molecules and the SA substrate (upper) and the DSA substrate. The straight lines represent the covalent bonds. The dashed lines represent the hydrogen bonding and ion–dipole bonding.

3.2.5 Surface morphology and roughness of DSA substrate

The variations of surface roughness and topography were characterized by DFM. The pristine HR substrate reveals a microtexture with sharp–tapered spikes with a ten–point mean roughness (R_z) of 0.7 nm (**Figure 3.7 a**), which is attributed to the high repellency of the hydrophobic substrate. After the PVUV exposure, the spikes were rearranged into blunt but dense protuberances, and the R_z was slightly decreased to 0.5 nm (**Figure 3.7 b**). Combining with the previous surficial chemical analyses, this topological change can be explained by the PVUV–induced surface oxidation.

After the SA substrate was rinsed with an alkali solution, its surface was transformed into a submicron–scale rough configuration with a high R_z value of 0.6 nm (**Figure 3.7 c**). This observation revealed that the DSA strategy finally increased the surface roughness again due to the partial removal of the photocleaved SA substrate via alkali neutralization, which is contributed to achieving high γ_s and F_A.

The comprehensive variations trigged by the DSA strategy of the smaller θ, higher R_f, wider ω, and larger *cah* demonstrate a remarkable effect of directly building the designated regions with both high γ_s and strong F_A, in conformance with our premise.

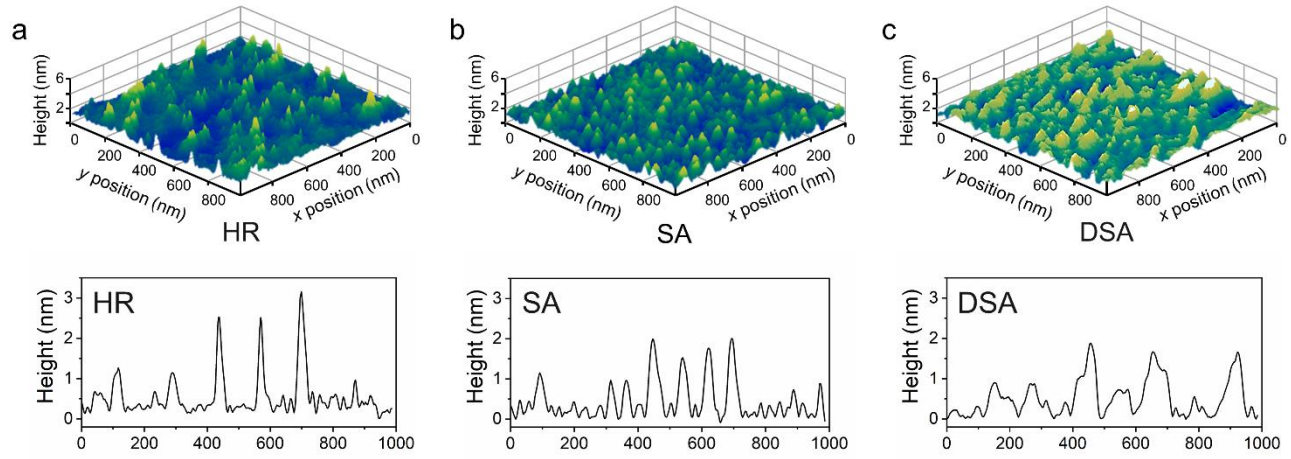

Figure 3.7. Topographies of the (a) HR substrate with 0.7 nm in R_z, (b) SA substrate with 0.5 nm in R_z, and (c) DSA substrate with 0.6 nm in R_z observed by dynamic force microscope (DFM).

3.2.6 Controlling of DSA strategy

Based on a series of topological and chemical characterizations, the effect of the proposed DSA substrate toward polymer substrate can be summarized as shown in **Figure 3.8**, where the PVUV exposure creates high γ_s regions and rinsing with an alkali solution endows the regions with strong F_A. Many factors can influence the final effect of the DSA strategy, including diversified optical processing technics with different light wavelengths, alkali solutions with various chemical components, and process parameter adjustment. To testify the applicability and find out the optimal parameter in the DSA strategy, process factors of the PVUV exposure time exposure toward the surficial chemical states were discussed.

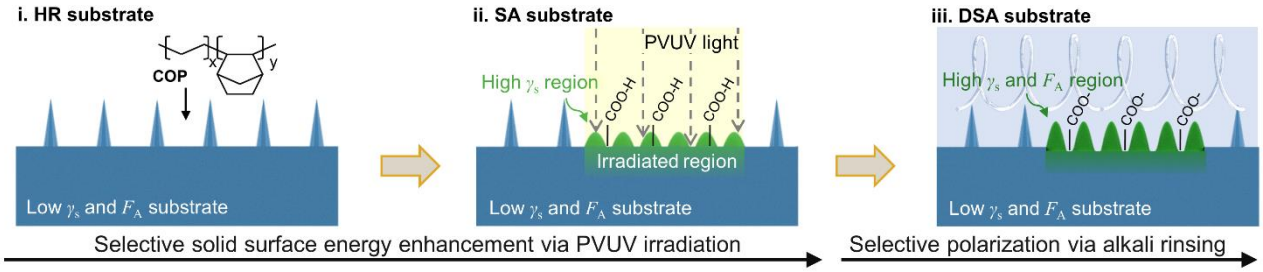

Figure 3.8. Sequence for surficial modification via DSA strategy.

In detail, a series of PVUV exposure ranging from 0 to 600 s were used to treat the HR substrates. The surface chemical states of the pristine HR and the obtained SA substrates were investigated based on the XPS spectra, as shown in **Figure 3.9 a**. With the increase of PVUV exposure time, the intensity ratio of OPFGs kept increasing, indicating that the γ_s can be enhanced facilely and controllably. After rinsing the PVUV–irradiated SA substrate by alkali solution, the peak intensity and area containing OPFGs were decreased (**Figure 3.9 b**). Notably, among different OPFGs, a rapid intensity decrease of carboxyl was observed, which can be attributed to the alkali neutralization and the magnified surface polarization. Taken together, these results suggest that the proposed DSA strategy can manipulate the solid surface energy and surface polarization effectively via simply adjusting the PVUV exposure time, showing strong potential in putting into the practical liquid–mediated directed self–assembly system.

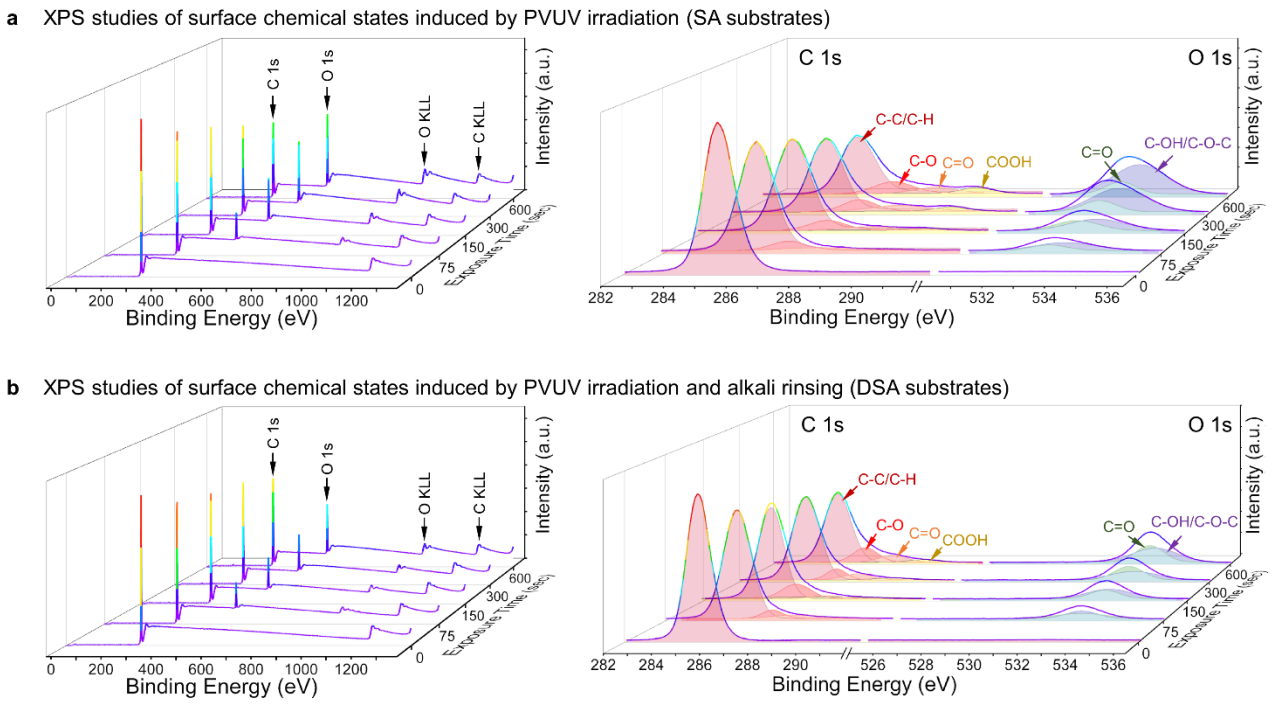

Figure 3.9. XPS wide spectra and high–resolution spectra of C 1s and O 1s of modified substrates induced by (a) PVUV exposure and (b) PVUV exposure and alkali rinsing.

3.2.7 Evaluation of directed self–assembly property

To evaluate the directed self–assembly property of the proposed DSA substrate directly, two different demonstrations have been designed to assess the behaviors of selective adsorbing and selective pinning, respectively. **Figure 3.10** shows time–resolved observations of water flow on the semi–modified surface. When the pendant drop approaches the substrate, the drop spontaneously flows toward the modified DSA region, demonstrating the effect of PVUV and alkali rinsing for increasing the γ_s and F_A to guide the fluidic flow.

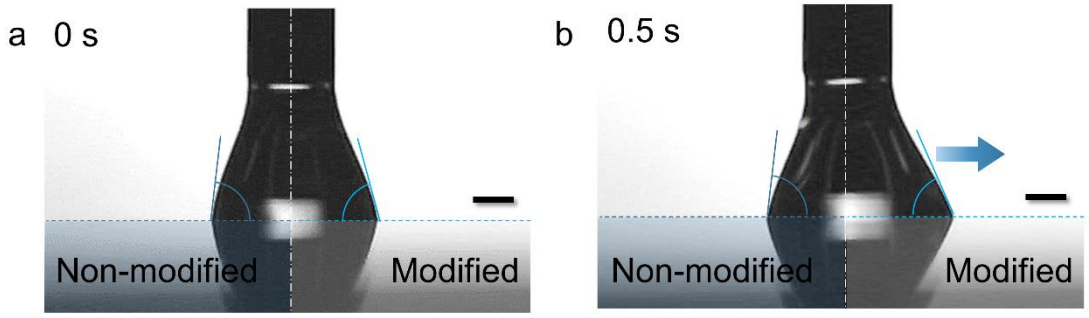

Figure 3.10. Time–resolved flow of a pendant drop on the semi–modified DSA surface. Scale bars: 350 μm. Drop volume: 2.0 μL.

A drop–sliding test based on the liquid friction force measurement was carried out to evaluate the F_A of the DSA substrate.[94] As shown in **Figure 3.11 a**, the drop presents both high θ_{adv} and θ_{rec} during flowing above the HR substrate, confirming the high liquid repellency. For the SA substrate with the designated modified regions, the slightly increased θ_{adv} and decreased θ_{rec} of the drop were observed during flowing, indicating the self–assembly

property with wetting/dewetting behavior has been generated (**Figure 3.12 b**). However, the effect of the SA modification was not strong enough to pin the liquid on the designated areas. Strikingly, we observed the initiative wetting with vastly increased θ_{adv}, hysteretic dewetting with significantly decreased θ_{rec}, and distinct pinning on the designated regions were observed in the drop flowing over the DSA substrate (**Figure 3.12 c**). Therefore, we conclude that the directed self–assembly property has been significantly improved by the DSA process, which generates the selectively strong shear stresses for pinning the liquid on the designated regions firmly.

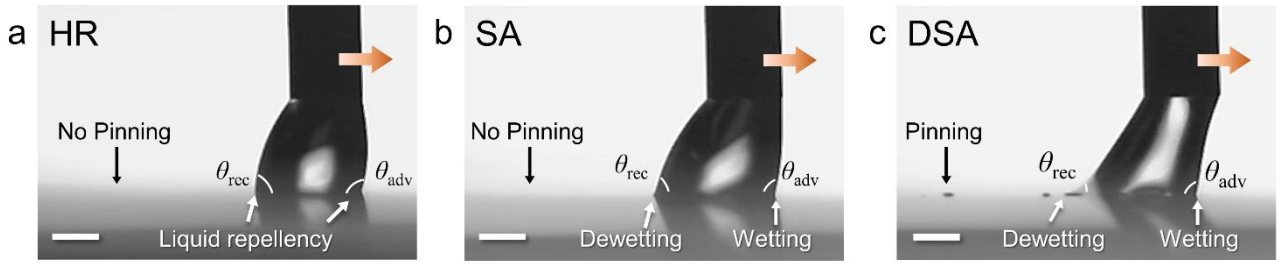

Figure 3.11. Photographs of drop–sliding tests above the (a) HR, (b) SA and (c) DSA surfaces. Scale bars: 350 μm. Drop volume: 2.0 μL.

3.3 Conclusion

The issue of the low resolution of self–assembled electronics has long been a crucial problem hindering practical applications. In this chapter, a DSA strategy has been demonstrated, where the γ_s as well as the F_A are found to be two critical factors for amplifying the directed self–assembly property. We designed a serial treatment of optically oxidation and chemical polarization to create hydrophilic regions with enhanced polarity, leading to the simultaneous improvement of both γ_s and F_A with a remarkable attracting–pinning effect toward the functional inks. Furthermore, the modified surface states can be optimized facilely by parameter adjusting, providing a versatile platform in patterning different kinds of functional materials onto the targeted substrates for the fabrication of additively manufactured electronic (AME).

Reference

[34] J. Bae, J. Lee, Q. Zhou, T. Kim, Micro–/Nanofluidics for Liquid–Mediated Patterning of Hybrid–Scale Material Structures, Adv. Mater. 31 (2019) 1804953. https://doi.org/10.1002/adma.201804953.

[40] Y. Chu, C. Qian, P. Chahal, C. Cao, Printed Diodes: Materials Processing, Fabrication, and Applications, Adv. Sci. 6 (2018) 1801653. https://doi.org/10.1002/advs.201801653.

[43] W. Wu, Inorganic Nanomaterials for Printed Electronics: A Review, Nanoscale. 9 (2017) 7342–7372. https://doi.org/10.1039/C7NR01604B.

[49] T. Minari, C. Liu, M. Kano, K. Tsukagoshi, Controlled Self–Assembly of Organic Semiconductors for Solution–Based Fabrication of Organic Field–Effect Transistors, Adv. Mater. 24 (2012) 299–306. https://doi.org/10.1002/adma.201102554.

[80] J.R. Chen, T. Wakida, Studies on the surface free energy and surface structure of PTFE film treated with low temperature plasma, J. Appl. Polym. Sci. 63 (1997) 1733–1739. https://doi.org/https://doi.org/10.1002/(SICI)1097–4628(19970328)63:13<1733::AID–APP4>3.0.CO;2–H.

[83] C. Cummins, R. Lundy, J.J. Walsh, V. Ponsinet, G. Fleury, M.A. Morris, Enabling future nanomanufacturing through block copolymer self–assembly: A review, Nano Today. 35 (2020) 100936. https://doi.org/10.1016/j.nantod.2020.100936.

[84] D. Karnaushenko, T. Kang, V.K. Bandari, F. Zhu, O.G. Schmidt, 3D Self–Assembled Microelectronic Devices : Concepts , Materials , Applications, Adv. Mater. 32 (2020) 1902994. https://doi.org/10.1002/adma.201902994.

[85] A. Falco, L. Cina, G. Scarpa, P. Lugli, A. Abdellah, Fully–Sprayed and Flexible Organic Photodiodes with Transparent Carbon Nanotube Electrodes, ACS Appl. Mater. Interfaces. 6 (2014) 10593–10601. https://doi.org/https://doi.org/10.1021/am5022123.

[86] M.G. Mohammed, R. Kramer, All–Printed Flexible and Stretchable Electronics, Adv. Mater. 29 (2017) 1604965. https://doi.org/10.1002/adma.201604965.

[87] C. Yeom, K. Chen, D. Kiriya, Z. Yu, G. Cho, A. Javey, Large–Area Compliant Tactile Sensors Using Printed Carbon Nanotube Active–Matrix Backplanes, Adv. Mater. 27 (2015) 1561–1566. https://doi.org/10.1002/adma.201404850.

[88] X. Liu, C. Liu, K. Sakamoto, T. Yasuda, P. Xiong, L. Liang, T. Yang, M. Kanehara, J. Takeya, T. Minari, Homogeneous dewetting on large–scale microdroplet arrays for solution–processed electronics, NPG Asia Mater. 9 (2017) e409. https://doi.org/10.1038/am.2017.123.

[89] É. Lorenceau, D. Quéré, Drops on a conical wire, J. Fluid Mech. 510 (2004) 29–45. https://doi.org/10.1017/S0022112004009152.

[90] J. Ju, H. Bai, Y. Zheng, T. Zhao, R. Fang, L. Jiang, A multi–structural and multi–functional integrated fog collection system in cactus, Nat. Commun. 3 (2012) 1–6. https://doi.org/10.1038/ncomms2253.

[91] T. Wong, S.H. Kang, S.K.Y. Tang, E.J. Smythe, B.D. Hatton, A. Grinthal, J. Aizenberg, Bioinspired self–repairing slippery surfaces with pressure–stable omniphobicity, Nature. 477 (2011) 443–447. https://doi.org/10.1038/nature10447.

[92] T. Young, An Essay on the Cohesion of Fluids, Philos. Trans. R. Soc. III (1997) 65–87. https://doi.org/10.5840/faithphil201027329.

[93] D. Kim, N.M. Pugno, S. Ryu, Wetting theory for small droplets on textured solid surfaces, Sci. Rep. 6 (2016) 37813. https://doi.org/10.1038/srep37813.

[94] N. Gao, F. Geyer, D.W. Pilat, S. Wooh, D. Vollmer, H.J. Butt, R. Berger, How drops start sliding over solid surfaces, Nat. Phys. 14 (2018) 191–196. https://doi.org/10.1038/nphys4305.

[95] E. Pierce, F.J. Carmona, A. Amirfazli, Understanding of sliding and contact angle results in tilted plate experiments, Colloids Surfaces A Physicochem. Eng. Asp. 323 (2008) 73–82. https://doi.org/10.1016/j.colsurfa.2007.09.032.

[96] C.G.L. Fumridge, Studies At Phase Interfaces I. the Sliding of Liquid Drops on Solid Surfaces and a Theory for Spray Retention, J. Colloid Sci. 17 (1962) 309–324. https://doi.org/10.1016/j.ultrasmedbio.2012.04.007.

[97] H.B. Eral, D.J.C.M. Mannetje, J.M. Oh, Contact angle hysteresis : a review of fundamentals and applications, COLLOID Polym. Sci. (2013) 247–260. https://doi.org/10.1007/s00396–012–2796–6.

[98] Y.J. Kim, Y. Taniguchi, K. Murase, Y. Taguchi, H. Sugimura, Vacuum ultraviolet–induced surface

modification of cyclo–olefin polymer substrates for photochemical activation bonding, Appl. Surf. Sci. 255 (2009) 3648–3654. https://doi.org/10.1016/j.apsusc.2008.10.009.

[99] M. Delmas, M. Monthioux, T. Ondarçuhu, Contact angle hysteresis at the nanometer scale, Phys. Rev. Lett. 106 (2011) 136102. https://doi.org/10.1103/PhysRevLett.106.136102.

[100] T. Yamada, K. Fukuhara, K. Matsuoka, H. Minemawari, J. Tsutsumi, N. Fukuda, K. Aoshima, S. Arai, Y. Makita, H. Kubo, T. Enomoto, T. Togashi, M. Kurihara, T. Hasegawa, Nanoparticle chemisorption printing technique for conductive silver patterning with submicron resolution, Nat. Commun. 7 (2016) 11402. https://doi.org/10.1038/ncomms11402.

[101] G. Schelcher, C. Guyon, S. Ognier, S. Cavadias, E. Martinez, V. Taniga, L. Malaquin, P. Tabeling, M. Tatoulian, Cyclic olefin copolymer plasma millireactors, Lab Chip. 14 (2014) 3037–3042. https://doi.org/10.1039/c4lc00423j.

[102] G. Xiao–hong, C. Guang–hao, S. Chii, ATR–FTIR and XPS study on the structure of complexes formed upon the adsorption of simple organic acids on aluminum hydroxide, J. Environ. Sci. 19 (2007) 438–443. https://doi.org/10.1007/978–1–84628–282–9_43.

[103] S. Zou, J. Liu, H. Kobayashi, X. Hu, L. Xiao, J. Fan, A new reaction between common compounds: Lead oxide reacts with formaldehyde, Chem. Commun. 50 (2014) 6316–6318. https://doi.org/10.1039/c3cc49239g.

[104] Y.L. Chen, C.A. Helm, J.N. Israelachvili, Molecular mechanisms associated with adhesion and contact angle hysteresis of monolayer surfaces, J. Phys. Chem. 95 (1991) 10736–10747. https://doi.org/10.1021/j100179a041.

[105] L. Qian, F. Tian, X. Xiao, Tribological properties of self–assembled monolayers and their substrates under various humid environments, Tribol. Lett. 15 (2003) 169–176. https://doi.org/10.1023/A:1024868532575.

[106] L. Rebohle, S. Prucnal, W. Skorupa, A review of thermal processing in the subsecond range: Semiconductors and beyond, Semicond. Sci. Technol. 31 (2016) 103001. https://doi.org/10.1088/0268–1242/31/10/103001.

Chapter 4

Ultrahigh–resolution self–assembled electrodes for additively manufactured OTFTs

4.1 Introduction

Directed self–assembly of functional materials appears to be a promising alternative to photolithography due to its high process compatibility toward soft electronic manufacturing and simple fabrication process.[107–108] As such, the technology of directed self–assembly has been gathering increasing attention in the field of next–generation AMEs. However, under the rapid development of the AMEs market, the low resolution of the self–assembled pattern has become a serious problem. The current resolution of the self–assembled pattern remains around 10 μm. Very few studies reach the submicron resolution at the expense of severe coffee–ring effect and poor electrical performance.

In this chapter, by utilizing the proposed DSA strategy, we demonstrate the fabrication of ultrahigh–resolution AuNP patterns (600 nm) by directed self–assembly technology for the first time, with suppression of the coffee–ring effect and the realization of high conductivity (14.1 ± 0.6 μΩ cm). In addition, the resultant patterns can be used as high–resolution electrodes for the fabrication of fully additively manufactured OTFTs with 1 μm–wide short channels; these OTFTs exhibit a large on–off ratio of 10^6 and a high field–effect mobility of 0.5 $cm^2\ V^{-1}\ s^{-1}$. We expect these results to promote the practical applications of directed self–assembly technologies in AME manufacturing.

4.2 Results and discussion

4.2.1 Directed self–assembly of ultrahigh–resolution soft electrodes

The fabrication of self–assembled electronic circuits has been illustrated in **Figure 4.1**. The substrate was treated by DSA strategy using 150 s PVUV exposure and 30 s alkali rinsing. A π–junction AuNP ink was utilized to pattern the conductive electrode on the flexible DSA substrate under ambient atmospheric conditions.[77] In detail, the AuNP ink was swiped above the entire substrate using a commercial slit coating process (**Figure 4.1(i)**). The AuNP ink was then spontaneously assembled on the designated regions owing to the high surface energy state by DSA strategy (**Figure 4.1(ii)**). After the ink was dried at room temperature, the self–assembled flexible circuit could be formed facilely with no additional sintering benefitted by the conductive ligands of the utilized AuNPs (**Figure 4.1(iii)**).

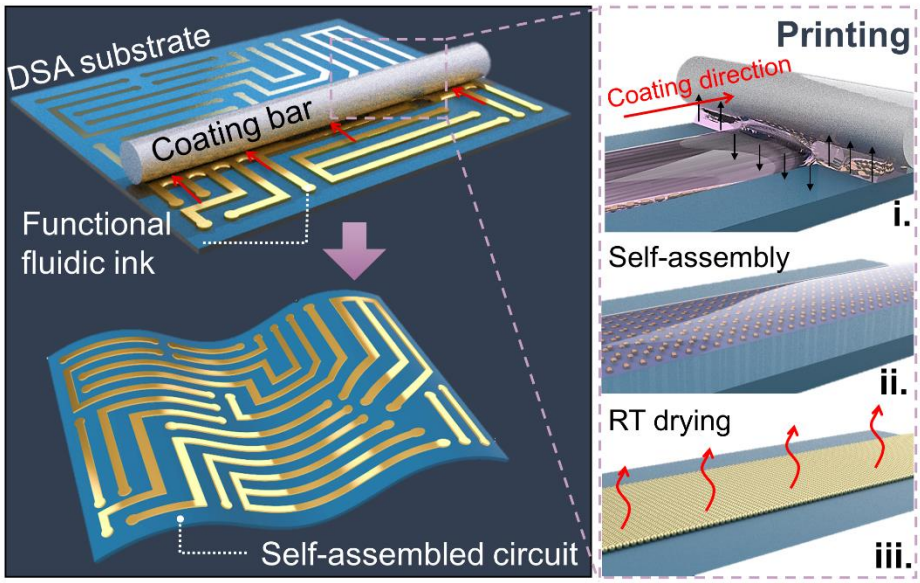

Figure 4.1. Schematic of the patterning procedures for the self–assembled AuNP circuit using a DSA substrate.

As shown in **Figure 4.2 a**, fine patterns with various shapes, including dots, polylines, curves, and straight lines, were formed on the DSA substrate in a single printing process. The designated regions were covered by the AuNP lines ranging from 5 μm to 600 nm in width, with well–defined boundaries and clear edges (**Figure 4.2 b**). No residual particles were observed on the repellent regions, indicating high–definition patterning. Notably, in this process, a submicron resolution (600 nm) was first achieved using non–lithographic directed self–assembly patterning (**Table 4.1**).

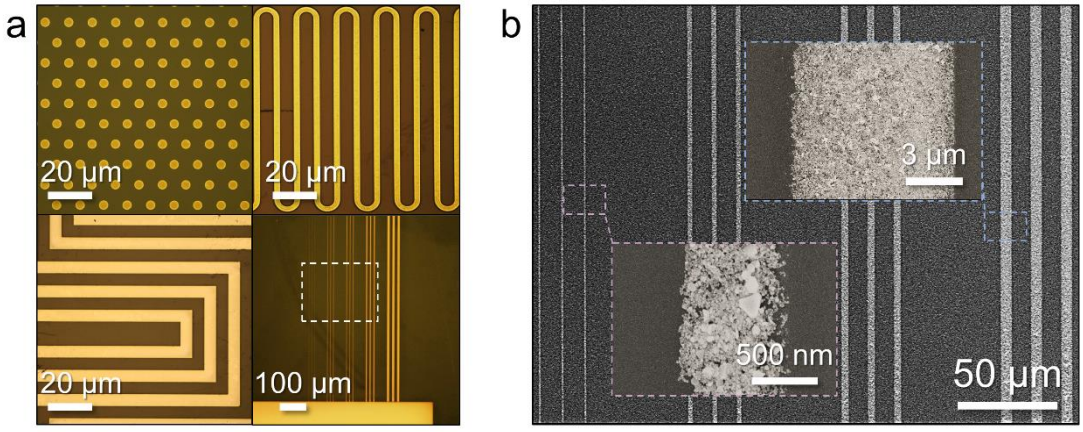

Figure 4.2. (a) Optical micrographs of the multiform electrodes. (b) Morphology observations of the lower–right circuit in Figure 4.2 (a) by scanning electron microscopy (SEM).

Table 4.1. Comparison of resolution, resistivity, patterning procedure and process factor with those state–in–the–art works using additively manufactured electrodes.

Electrode	Resolution [μm]	Resistivity [μΩ cm]	Coffee–ring effect	Ancillary structure/construction	Ref.
Electroplated CuNP	150	2.0	NA[b)]	Anti–adhesive template	[109]
Electroplated CuNP	10	1.93	NA	Photoresist template	[38]
Electroless–plated AgNP	2	4.7 Ω sq^{-1}	No	DMA template catalysis	[110]
Electroless–plated AuNP	10	120	NA	Ag template catalysis	[111]
Electroless–plated CuNP	18	3.2	NA	Ag template catalysis	[112]
Electroless–plated CuNP	1	3.2	No	Pd template catalysis	[113]
Electrostatic–interacted AgNP self–assembly	10	94.9	Serious	APTES template	[114]
Interfacial convective self–assembly	0.025	85.8	NA	Photoresist template	[115]
Chemisorption self–assembly AgNP	0.8	100	No	Perfluorinated template	[100]
SFE–triggered self–assembly AgNW	10	6.1	NA	CYTOP template	[64]
SFE–triggered self–assembly AgNP	0.3	NA	Serious	Photoresist template	[116]
SFE–triggered self–assembly AgNW	20	25 Ω sq^{-1}	NA	NR[c)]	[82]
SFE–triggered self–assembly AuNP	10	~9	Serious	NR	[77]
SFE–triggered self–assembly AuNP	1	NA	Serious	NR	[74]
DSA[a)] self–assembly AuNP	0.6	14.1	No	NR	This work

[a)] dual–surface–architectonics; [b)] not available; [c)] not required.

The reproducibility of the ultrahigh–resolution patterned structure was further investigated. **Figure 4.3** shows the SEM observations of the submicrometer structures on four parallel samples. The self–assembled high–resolution electrodes ranging from 600 nm to 3 μm exhibited distinct boundary lines and highly organized patterning structures. At the same time, the AuNPs were observed to be distributed evenly and stacked compactly with each other. These

observations indicate the high reproducibility and conductivity of the proposed DSA process. It is worth mentioning that the AuNPs exhibit the intrinsic high corrosion resistance than the other electrode materials, which also facilitate the electrical conductivity of the self–assembled patterns.

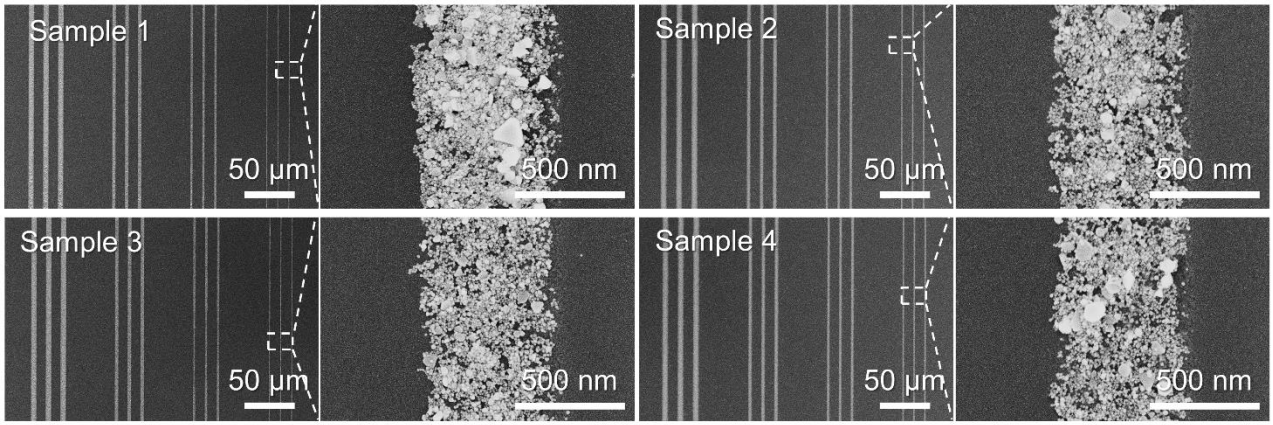

Figure 4.3. SEM observations of the self–assembled high–resolution patterns and the magnified regions of the submicrometer AuNP patterns among four parallel samples.

4.2.2 Mitigation of coffee–ring effect via DSA strategy

The performance of self–assembled electronics commonly suffers from the coffee–ring effect, where a drying droplet of the functional ink leaves a ring of solute deposits on a substrate rather than a uniform pattern, which leads to serious degradation of the electrical properties and poor interfacial contact in electronic devices.[117] In detail, during the solvent evaporation process, the radial–outward flow induced by the surface tension gradients carriers the solute from the center to the edge of the droplet.[118–119] Because the three–phase contact line of a droplet on a substrate with a high γ_s possesses a higher evaporating speed, the suspended solute is then drawn to the edge vicinity, where it forms a ring–shaped particle deposit (**Figure 4.4 a(i)**). As a demonstration, we show in **Figure 4.4 a (ii and iii)** that the microparticles were stacked at the droplet periphery on the SA substrate, consistent with the mechanism of the coffee–ring effect.[120] In addition, the particles were also deposited at the center of the droplet, resulting in a spot–inside–ring pattern, which is attributed to the weak substrate–solvent interactions.[121] By contrast, when the γ_s and F_A are increased simultaneously, the aggregation of the solute toward the three–phase contact line is expected to be harnessed through the high surface roughness and enhanced *cah*,[117,122] resulting in an interrupted radial–outward flow and a homogeneous arrangement of the solute (**Figure 4.4 b(i)**). Therefore, the particles were uniformly deposited onto the DSA substrate after evaporation without the severe coffee–ring pattern or the central spot, as shown in **Figure 4.4 b(ii) and b(iii)**.

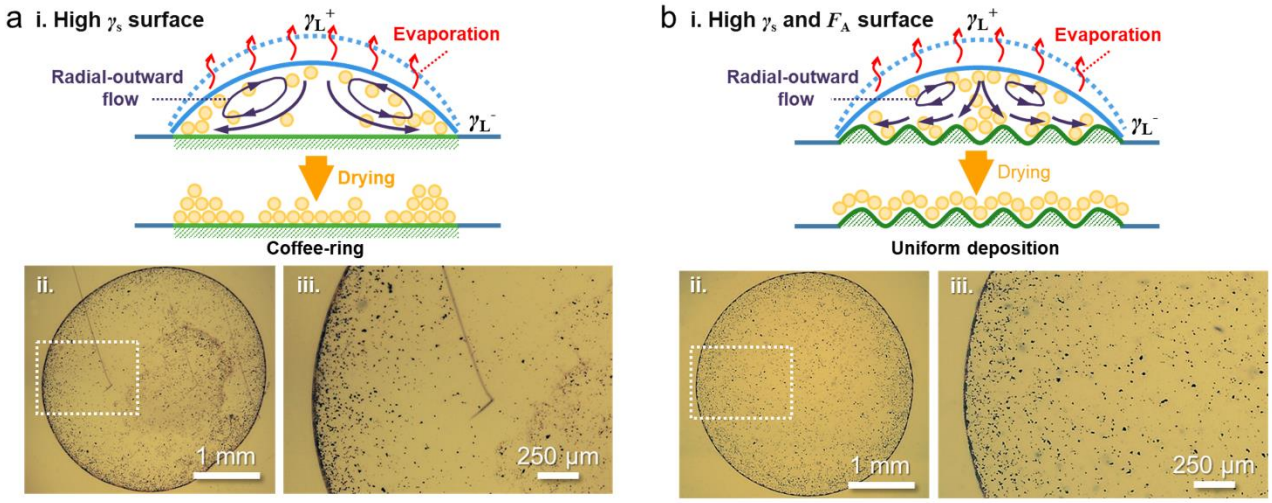

Figure 4.4. Effect of DSA process toward the coffee–ring effect. Schematics and optical micrography observations of the solute movement and the dried solution films using on the a) SA and b) DSA substrates.

We here discuss the difference between the patterned electrodes on the SA and DSA substrates. For the SA substrate, the patterned AuNPs piled up around the edge of the electrodes, resulting in a considerable height difference (0.5 μm) between the edge and the central area (**Figure 4.5 a**). In addition, an area of missing AuNP patterns and unclear boundaries were observed, in accordance with the weak self–assembly property. By contrast, the electrode patterned on the DSA substrate exhibits not only a flat topography with a dramatically decreased height difference (0.1 μm) but also high integrity of the self–assembled pattern (**Figure 4.5 b**). These results indicate that the proposed DSA technology can suppress the inherent problem of the coffee–ring effect as well as improve the patterning performance during self–assembly printing.

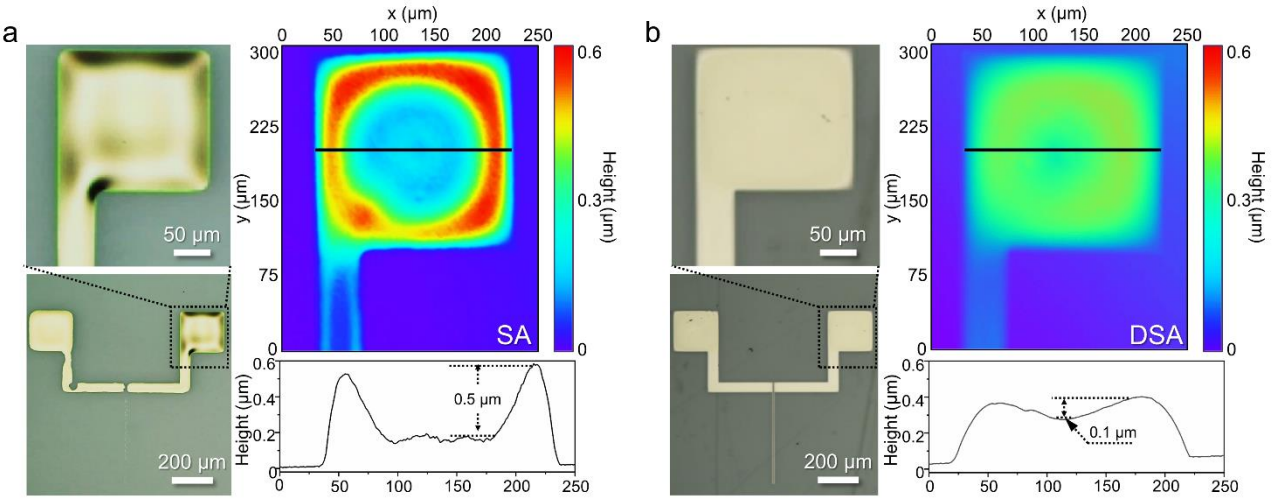

Figure 4.5. Optical micrographs, 3D interferometry images, and height profiles of the self–assembled patterns on the (a) SA and (b) DSA substrates.

4.2.3 Conductivity and reliability evaluations of self–assembled electrodes

To extend the self–assembly technology to a more realistic manufacturing environment, we investigated the

conductivity and reliability of the patterned AuNP electrodes. **Figure 4.6 a** shows the resistivity variations of AuNP electrodes according to the different linewidths and ink concentrations (test set shown in Figure 4.6 inset). In the case of the fluidic ink with 25 wt.% AuNPs, the self–assembled lines varying in the width from 20 μm to 2 μm exhibit a low resistivity (14.1 ± 0.6 μΩ cm) similar to that of pure Au (2.2 μΩ cm), indicating high and reliable conductivity. The resistivity increases exponentially when the linewidth is reduced to 1 μm. According to the topographical observation as shown in **Figure 4.6 b**, the height of self–assembled AuNP patterns keeps decreasing with the dimension shrinkage of the electrodes, suggesting a reduction of the charge transports among the stacked AuNPs. The mechanism of wettability–contrast–induced directed self–assembly changes with dimensional minimization of the self–assembled electrodes. Under the interaction effect among the decreased interfacial shear stresses, the aggravated horizontal Laplace pressure, and the rheology property of the AuNP ink, the volume of the pinned functional ink is not directly proportional to the electrodes with high–resolution linewidth, which leads to the decreased density of the stacked AuNPs and the irregularly increased resistivity after room–temperature evaporation.

At the same time, a higher resistivity with a similar trend change was observed from the lines patterned using the 15 wt.% AuNP ink, which further verifies certain relationship exists between the dimension of the patterned electrodes and the resistivity. Nevertheless, due to the rough gradient of the prepared electrode linewidths, the number of the data points is not sufficient for curve fitting, especially during the abrupt resistivity degradation among the high–resolution self–assembled electrodes (linewidth below 2 μm). The relationship will be studied and discussed by increasing the gradient of the electrode linewidths in the range from 600 nm to 2 μm in our further research. – Based on the change in the trend of the resistivity, we chose the fluidic ink with 25 wt.% AuNPs for the following electronic manufacturing.

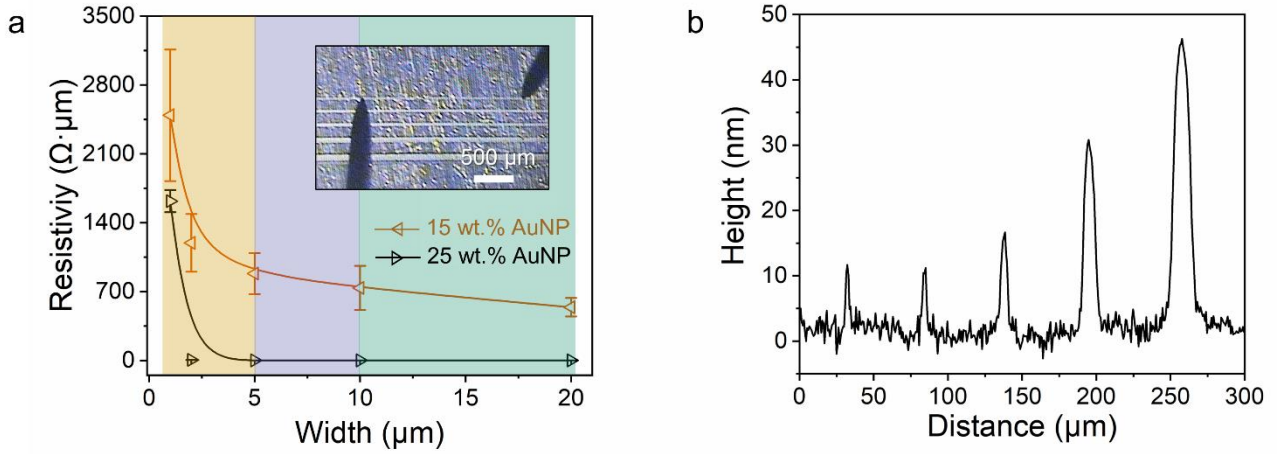

Figure 4.6. (a) Comparison of the resistivity with respect to ink concentration as a function of the patterned linewidths. Error bars indicate standard deviations of the results for seven independent samples; Inset: Photograph of the specimen testing for resistivity evaluation. The distance between two probes is 2000 μm. (b) The related height profile of the self–assembled AuNP patterns.

On the other hand, the long–term reliability of the high–resolution electrodes was further characterized by evaluating the resistivity variations after 500–day room–temperature and ambient atmospheric storage. As shown

in **Figure 4.7**, the long–term ageing had little effect on the AuNP self–assembled patterns with different linewidths, and the resistivities remained constant, which reveals the high reliability of the fabricated AuNP electrodes and the broad applicability to functional electronic manufacturing.

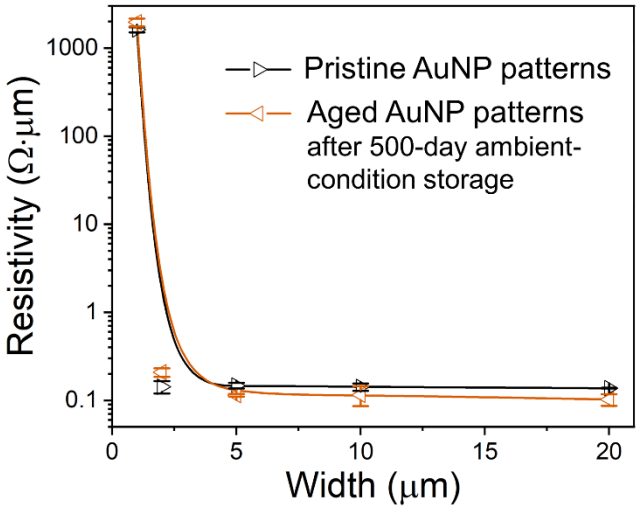

Figure 4.7. Comparison of the resistivity of just fabricated and aged (500–day storage under room temperature and ambient atmospheric pressure) 25 wt. % AuNP electrodes as a function of the self–assembled linewidths. Error bars indicate standard deviations of the results for seven parallel samples.

4.2.4 Additively manufacturing of high–resolution short–channel OTFT array

Owing to the large work function of the utilized AuNPs (4.69 eV), the applicability of the patterned high–resolution AuNP circuits is further examined by integrating them into an OTFT array as electrode materials. First, the bottom–contact S/D electrodes with a linewidth from 1 to 10 μm and short channel width (1 μm) were fabricated on the DSA substrates (**Figure 4.8(i) and 4.9**). The organic semiconductor solution (C6–DNT–VW) was then deposited onto the channel regions upon the screen–printed removable guide layer, resulting in a discrete array of semiconductor crystal islands (**Figures 4.8(ii) and 4.10 a**). After the insulating dielectric layer (parylene–C) was laminated on the top of the substrate (**Figure 4.8(iii)**), the gate (G) electrodes were assembled precisely with clear morphology and distinct boundaries using the proposed self–assembly patterning process (**Figure 4.8(iv) and 4.10 b and 4.10 c**).

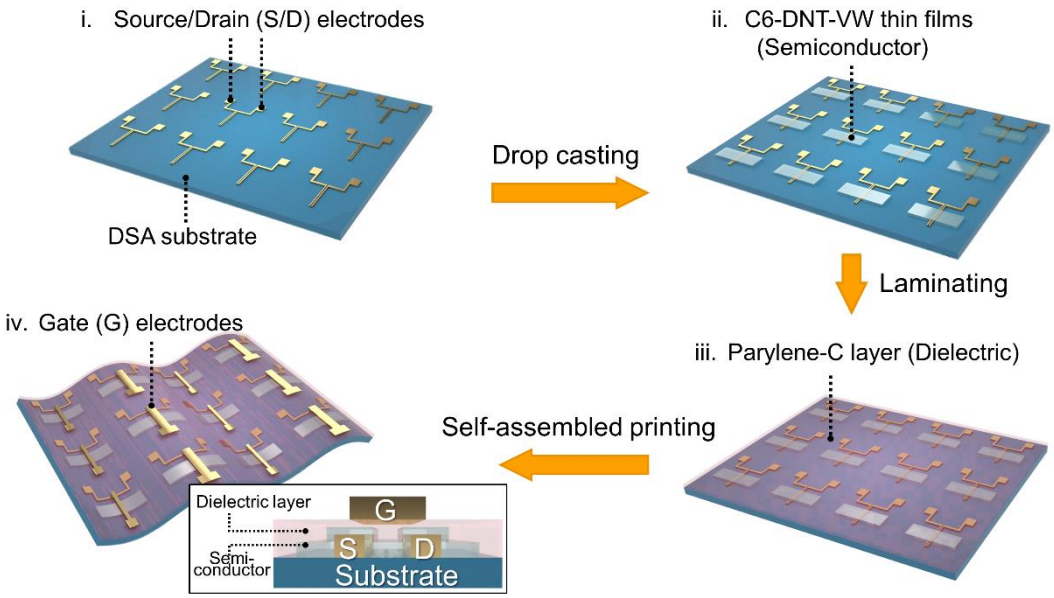

Figure 4.8. Platform for fabricating high–resolution organic thin–film transistor (OTFT) arrays. Fabrication process flow for the integration of OTFT arrays: (i) Spontaneous patterning of high–resolution S/D electrode circuit on the DSA substrate. (ii) Drop–casting semiconductor (C6–DNT–VW) crystal islands above the S/D electrodes. (iii) Laminating a dielectric (parylene–C) layer. (iv) Spontaneous patterning gate (G) electrodes to complete the transistor structure; the inset shows the multilayered structure of the integrated transistor.

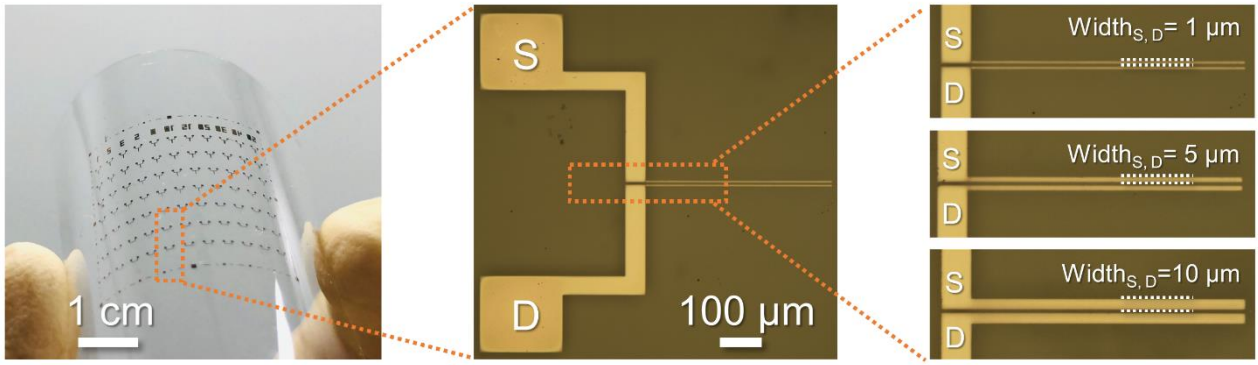

Figure 4.9. Digital image and optical micrographs of a flexible S/D electrode circuit, and magnified regions with different electrode widths.

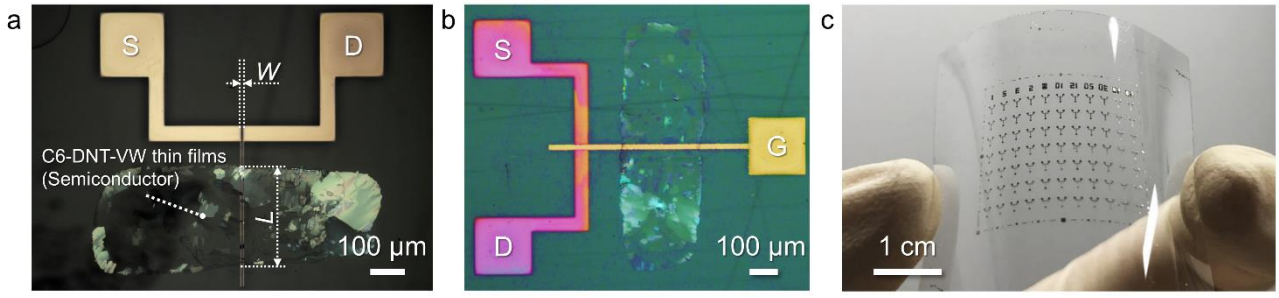

Figure 4.10. (a) Optical micrograph of S/D electrode with the channel width of 1 μm after semiconductor deposition. The channel region has been marked with length (L) of 300 μm and width (W) of 1 μm. (b) Optical micrograph of a top–gate OTFT. (c) Digital image of the integrated OTFT arrays.

4.2.5 Typical output and transfer characteristics of integrated OTFTs

We investigated the variation in the electrical performances of the OTFTs depending on the electrode linewidth by characterizing their typical output and transfer characteristics. As shown in **Figure 4.11 a**, approximately linear dependences of I_{DS} in the low $-V_{DS}$ regime were observed and finally saturated with V_{DS} beyond the pinch–off point. This behavior was unified among the patterned OTFTs using the S/D electrodes with different linewidths of 10, 5, and 1 μm, suggesting that the channel majority free charge carrier distribution in these additively manufactured OTFTs was uniform, with few fixed charged defects.

Since the potential applications of these OTFTs are massively used as electronic switches, we also evaluated the transistor function of the switching capacity (**Figure 4.11 b**). The transistors with electrode widths of 10 and 5 μm exhibited a large on–off ratio of 10^6 with a steep increase in I_{DS} and an average mobility as high as 0.5 $cm^2\ V^{-1}\ s^{-1}$ in the saturated regime. Meanwhile, the on–off ratio of the transistor with 1 μm–wide electrodes decreased to 10^4, with a relatively small subthreshold slope and lower mobility ($4.9 \times 10^{-4}\ cm^2\ V^{-1}\ s^{-1}$). These variations are attributed to the limited charge carrier transport and increased contact resistance between the interfaces of the semiconductor and high–resolution electrodes, which requires further optimization for reducing the surface roughness. Nevertheless, we note that the integrated OTFTs with 1 μm–wide high–resolution electrodes exhibit decent electrical performance in both electronic characterizations, which demonstrates the potential of the DSA strategy in the fabrication of transistors or other optoelectronics/bioelectronics with shrunken dimensions.

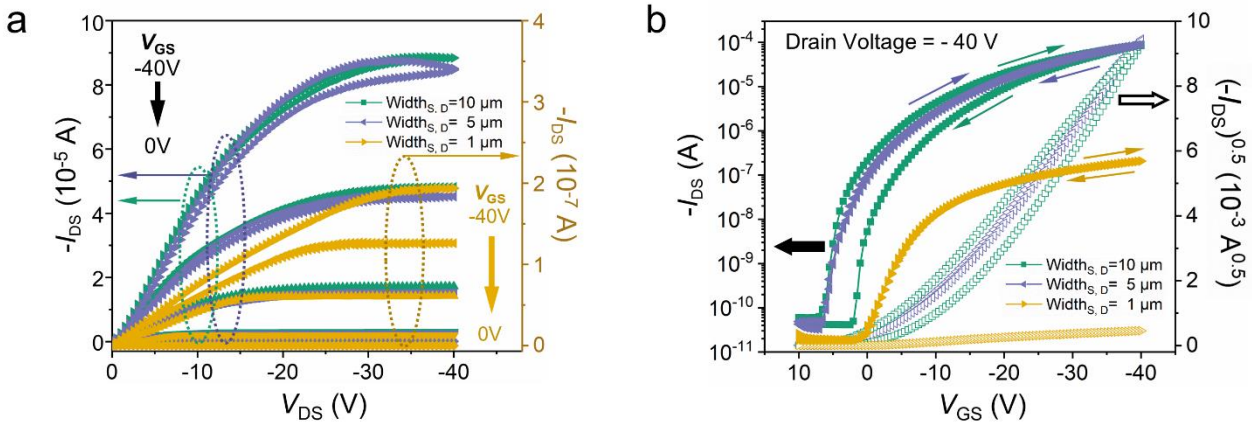

Figure 4.11. Comparisons of typical (a) output and (b) transfer characteristics of high–resolution OTFTs with different electrode linewidths.

4.3 Conclusion

In this chapter, a directed self–assembled AuNP electrode fabricated using the DSA strategy has been reported with all of the high–performance characteristics, including high–resolution (submicron–scale) printability, high–definition forming for multiform circuits, a suppressed coffee–ring effect, stable electrical properties, and reliable

practical application prospects. The DSA substrates with high–γ_s and strong–F_A designated regions provide a versatile and reliable platform for the spontaneous patterning of high–resolution electronics. Because high–repellency polymer materials are commercially available in great diversity, one can transform different kinds of these solids into the DSA surfaces without the use of cumbersome and expensive fabrication procedures. Furthermore, by testing the wide variety of liquid–mediated manufacturing technologies, fluidic inks and their diversified physical and chemical properties, we are currently exploring the limitations of submicron–textural architecturing for miniaturizing self–assembled electrodes as well as the compatibility with other printing systems. We anticipate that the DSA process will be further developed to serve as an indispensable procedure that satisfies emerging criteria in the rapidly developing electronic market.

Reference

[77] T. Minari, Y. Kanehara, C. Liu, K. Sakamoto, T. Yasuda, A. Yaguchi, S. Tsukada, K. Kashizaki, M. Kanehara, Room–temperature printing of organic thin–film transistors with π–junction gold nanoparticles, Adv. Funct. Mater. 24 (2014) 4886–4892. https://doi.org/10.1002/adfm.201400169.

[107] K. Fukuda, T. Someya, Recent Progress in the Development of Printed Thin–Film Transistors and Circuits with High–Resolution Printing Technology, Adv. Mater. 29 (2017) 1602736. https://doi.org/10.1002/adma.201602736.

[108] W. Lee, T. Someya, Emerging trends in flexible active multielectrode arrays, Chem. Mater. 31 (2019) 6347–6358. https://doi.org/10.1021/acs.chemmater.9b00165.

[109] Y. Chang, Z. Yang, Additive Fabrication of Conductive Patterns by a Template Transfer Process Based on Benzotriazole Adsorption As a Separation Layer, ACS Appl. Mater. Interfaces. 8 (2016) 14211–14219. https://doi.org/10.1021/acsami.6b00499.

[110] Q. Qiang, J. Qin, Z. Wang, C. Zhao, Robust Conductive Micropatterns on PTFE Achieved via Selective UV–Induced Graft Copolymerization for Flexible Electronic Applications, ACS Appl. Mater. Interfaces. 11 (2019) 5517–5525. https://doi.org/10.1021/acsami.8b18209.

[111] T. Makita, R. Nakamura, M. Sasaki, S. Kumagai, T. Okamoto, S. Watanabe, J. Takeya, Electroless–Plated Gold Contacts for High–Performance, Low Contact Resistance Organic Thin Film Transistors, Adv. Funct. Mater. 2003977 (2020) 1–9. https://doi.org/10.1002/adfm.202003977.

[112] J. Marques–hueso, T.D.A. Jones, D.E. Watson, A. Ryspayeva, M.N. Esfahani, M.P. Shuttleworth, R.A. Harris, R.W. Kay, M.P.Y. Desmulliez, A Rapid Photopatterning Method for Selective Plating of 2D and 3D Microcircuitry on Polyetherimide, Adv. Funct. Mater. 28 (2020) 1704451. https://doi.org/10.1002/adfm.201704451.

[113] W. Li, L. Li, Q. Sun, X. Liu, M. Kanehara, T. Nakayama, J. Jiu, K. Sakamoto, T. Minari, s Direct fabrication of high–resolution and high–performance flexible electronics via surface–activation–localized electroless plating, Chem. Eng. J. (2020) 1–20. https://doi.org/10.1016/j.cej.2020.127644.

[114] A. Kim, Y. Jo, J.C. Won, Y. Choi, K.S. Jang, S. Jeong, Y.H. Kim, Site–Selective Multi–Stacked Assembly of Silver Nanoparticles on Amine–Functionalized Printed Patterns: Comparative Studies on the Role of Electrostatic Interaction and Meniscus, Adv. Mater. Interfaces. 2 (2015) 1500129.

https://doi.org/10.1002/admi.201500129.

[115] Z. Chai, A. Korkmaz, C. Yilmaz, A.A. Busnaina, High–Rate Printing of Micro / Nanoscale Patterns Using Interfacial Convective Assembly, Adv. Mater. 32 (2020) 2000747. https://doi.org/10.1002/adma.202000747.

[116] S.A. Abbasi, Z. Chai, A. Busnaina, Scalable Printing of High–Resolution Flexible Transparent Grid Electrodes Using Directed Assembly of Silver Nanoparticles, Adv. Mater. Interfaces. 6 (2019) 1900898. https://doi.org/10.1002/admi.201900898.

[117] H. Hu, R.G. Larson, Marangoni effect reverses coffee–ring depositions, J. Phys. Chem. B. 110 (2006) 7090–7094. https://doi.org/10.1021/jp0609232.

[118] H. Ko, J. Park, H. Shin, J. Moon, Rapid Self–Assembly of Monodisperse Colloidal Spheres in an Ink–Jet Printed Droplet, Chem. Mater. 16 (2004) 4212–4215. https://doi.org/10.1021/cm035256t.

[119] Á.G. Marín, H. Gelderblom, D. Lohse, J.H. Snoeijer, Order–to–disorder transition in ring–shaped colloidal stains, Phys. Rev. Lett. 107 (2011) 085502. https://doi.org/10.1103/PhysRevLett.107.085502.

[120] R.D. Deegan, O. Bakajin, T.F. Dupont, G. Huber, S.R. Nagel, T.A. Witten, Capillary flow as the cause of ring stains from dried liquid drops, Nature. 389 (1997) 827–829. https://doi.org/https://doi.org/10.1038/39827.

[121] D. Mampallil, H. Burak, A review on suppression and utilization of the coffee–ring effect, Adv. Colloid Interface Sci. 252 (2018) 38–54. https://doi.org/10.1016/j.cis.2017.12.008.

[122] A. Gençer, C. Schütz, W. Thielemans, Influence of the particle concentration and marangoni flow on the formation of cellulose nanocrystal films, Langmuir. 33 (2017) 228–234. https://doi.org/10.1021/acs.langmuir.6b03724.

Chapter 5

Internal microflow manipulation by velocity field gradients: spontaneous patterning of AgNWs for flexible TCs

5.1 Introduction

Flexible TCs enable electron transport without blocking the passage of light; they are therefore widely applied in the ongoing development of soft optoelectronics, including flexible photovoltaics,[123–124] displays,[125–126] smart windows,[127–128] transparent heaters,[129] and electromagnetic interference shielding.[22,130] Among a large number of compositive nanomaterials, one–dimensional (1D) nanowires (NWs), such as AgNWs,[131] gold nanowires (AuNWs),[132] and metallic alloyed NWs,[133] are well known for their good conductivity, variable light–blocking efficiency, and inherent flexibility. However, the large–scale, facile fabrication of high–performance NW TCs is still required for achieving practical production. Currently, NW TCs are fabricated by overcoating[57,134–135] or templated assembly,[63–69] which either lowers the transmittance or complicates the process.

In the present study, by using an NW–structured solute to introduce capillary force into the system, the DSA strategy was extended to create a continuous internal microflow field to maneuver the dispersed NWs and spontaneously form the patterned NW TCs. We achieved this by manipulating the entire microflow velocity field at the interface between the functional ink and target surface using the surface energy contrast of the DSA substrate. In this proposed system, after overcoating the DSA substrate with the AgNW functional ink, the dispersed AgNWs in ink are effectively trapped onto the designated regions in a layer–by–layer alignment fashion by periodically changed internal microflow, resulting in self–organized AgNW patterns with a cross–linked structure and precise fixation. The combination of the microflow velocity–field–gradient manipulation and optical sintering allows for the fabrication of various patterned NW TCs at different scales. We demonstrate the fabrication of honeycomb–structured NW patterns, which can be used as flexible TCs with an ultrahigh transmittance (98.2%, excluding the substrate), low sheet resistance (29.7 Ω sq−1), and excellent mechanical durability during 5000 bending cycles. The performance of the proposed flexible TC is much better than those of previously reported TCs using the state–of–the–art NW or even NP patterning technologies. Apart from NW patterns with regular structures, patterns with arbitrary structures can also be self–assembled directly using the proposed technique.

As a proof of concept, we demonstrate the potential application of the structured NW TCs with customized irregular patterns as flexible transparent heaters with adjustable localized heat sources. More importantly, AgNWs with different aspect ratios can be patterned into highly ordered structures for high–performance flexible TCs. Quantitative experiments and relevant simulations indicated that the proper surface energy contrast regulated by DSA strategy generates a periodically changed interfacial velocity field, which leads to the observed directed self–assembly behavior. We believe that the proposed strategy is versatile and can enable the spontaneous patterning of diverse 1D materials into a wide range of composites with tailored topologies and functions, leading to the

development of novel high–performance soft electronics.

5.2 Results and discussion

5.2.1 Fabrication of self–assembled AgNW patterns by microflow velocity–field–induced alignment

In this study, we extended the DSA strategy to spontaneously pattern TCs with aligned 1D NWs by using NWs as solute to introduce capillary force into the directed self–assembly system. An aqueous functional ink containing AgNWs was used to demonstrate the utility of the proposed strategy. First, using a cascade of photoirradiation and chemical polarization via PVUV exposure and alkali rinsing, we produced a DSA polymer film with activated high–surface–energy (γ_s^+) regions and low–surface–energy (γ_s^-) regions (**Figure 5.1(i) and (ii)**). The AgNW functional ink was then spread across the DSA film via a simple slit coating. Unlike in the conventional self–assembly process, in which the liquid is trapped on the γ_s^+ regions, the AgNW functional ink overlaid on the DSA film formed a cross–border solution layer (**Figure 5.1(iii)**). Subsequently, the AgNWs dispersed in the functional ink migrated toward the γ_s^- regions and exhibited directional stacking during room–temperature evaporation, generating a metal circuit with a spontaneously aligned AgNW network (**Figure 5.1(iv)**). Time–resolved OM observations of spontaneous AgNW alignment in the aqueous cross–border solution layer has been shown in **Figure 5.2**. After spreading the AgNW functional ink over the DSA substrate (**Figure 5.2(i)**) by commercial slit–coating process, the functional ink overcoated the surface entirely irrespective of the surface states of the DSA substrate (**Figure 5.2(ii)**). In the absence of any net external force, the dispersed AgNWs migrated toward the γ_s^- regions and anchored on the sites in less than 2 s (**Figure 5.2(iii)**). Then, the dispersed AgNWs drifted with the subsequently generated microflow and stacked above the γ_s^- regions repeatedly, resulting in a circuit with spontaneously aligned AgNW network after room–temperature evaporation (**Figure 5.2(iv–vi)**). Afterwards, the AgNW film was further dried by IPL irradiation (**Figure 5.1(v)**). Thus, we fabricated large–area conductive films via directed self–assembly of AgNWs, in this case, honeycomb–structured patterns. This technique offers unprecedented opportunities for scaling up the production of high–performance transparent optoelectronics (**Figure 5.1(vi)**).

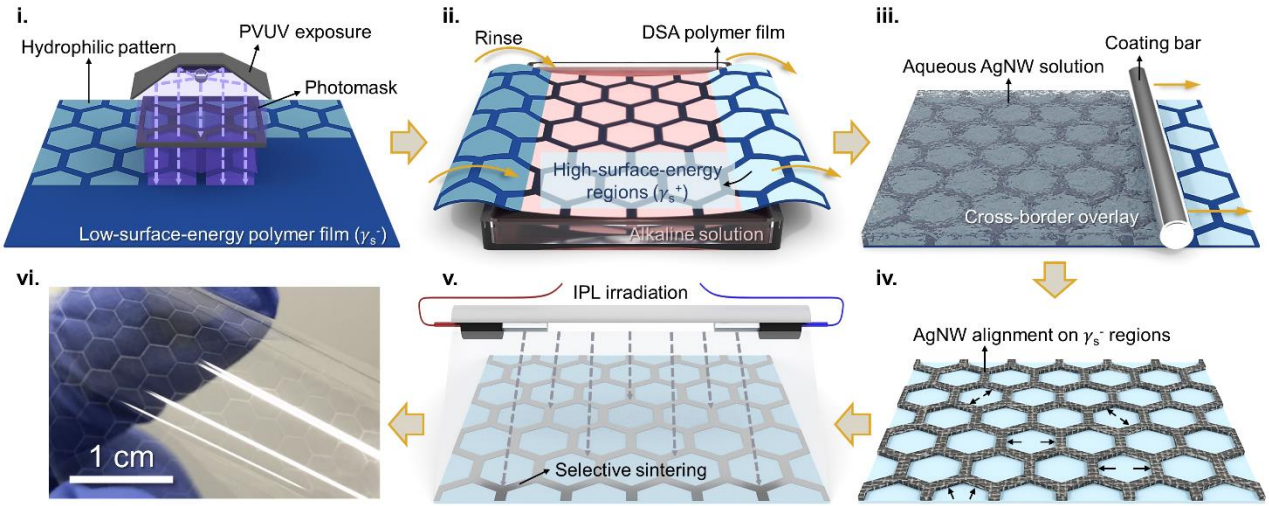

Figure 5.1. Schematics of the directed self–assembly process of 1D silver NWs (AgNWs), which involves the DSA substrate modification (i and ii) via a cascade of photochemical reactions using PVUV exposure and alkali rinsing,

(iii) deposition of the AgNW functional ink on the DSA substrate via slit coating, (iv) spontaneous alignment of the dispersed AgNWs, (v) drying, and (vi) digital image of a patterned AgNW transparent conductor (TC).

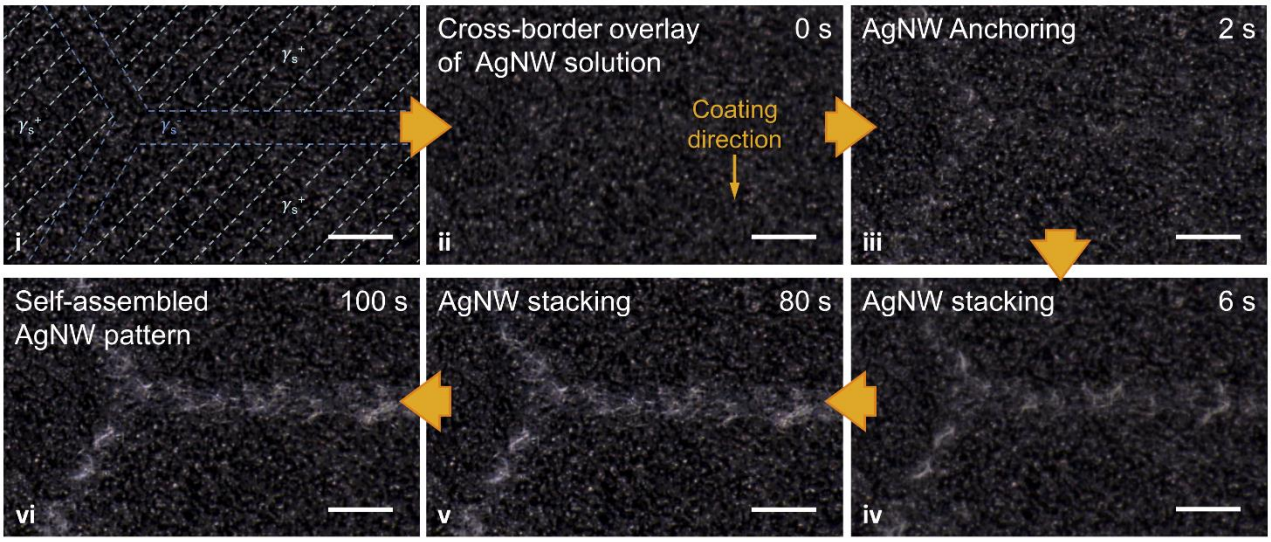

Figure 5.2. Time–resolved optical microscopy (OM) observations of spontaneously AgNW alignment process in the aqueous cross–border solution layer. Scale bars: 200 μm.

5.2.2 Mechanism of self–assembled AgNW patterns by microflow velocity–field–induced alignment

Uneven surface energy creates periodic shear force variations,[94] which are beneficial for the in–plane stacking of 1D NWs. To understand this AgNW stacking behavior, we analyzed the dynamics of the flow inside the cross–border solution layer over the DSA substrate using ANSYS Fluent 2021 R1 software package. The flow was considered laminar according to the calculated low Reynolds Number (≈3×10^3), as given in,

$$Re = \frac{\rho u x}{v} \qquad \text{(Equation 5.1)}$$

where ρ is the density of the fluid, u is the flow speed, x is the local distance from the leading edge along with the flat plate as the characteristic length, and v is the dynamic viscosity of the fluid. The bulk temperature was 300 K, and the height of overlaid fluid layer was assumed to be 250 μm which is consistent with the spacing between the substrate and the coating bar. The flow contains the same fluid water so that we can focus on exploring the effect of solid surface energy toward the microflow velocity field manipulation. To simulate the internal microflow in the entire overlaid solution layer, the microstructural 2D geometry of laminar flow over a flat plate was developed and meshed as a structured grid with rectangle volume elements. The substrate was separated into two areas with high and low flow friction factors according to their different surface energies. The widths of γ_s^+ regions and γ_s^- regions were set to be1500 and 100 μm, respectively, which are the same as the practical patterns. And the flow was set to be a periodic, incompressible laminar water flow because of the low Reynolds number. Considering that the fluid flows over a periodically changed substrate, the translational periodic boundary condition was applied in this fluid domain with a mass flow rate of 0.5 g s^{-1} instead of using inlet and outlet conditions. To define the boundary at the liquid/solid interface, the entire solid surface overcoated by the solution layer was considered to be wettable, leading

to the Wenzel model. According to Wenzel state, a relationship exists between contact angle and surface roughness of the modified surface,

$$\cos\theta^* = r'\cos\theta \qquad \text{(Equation 5.2)}$$

where θ is the contact angle, θ* is the contact angle with the smooth surface, and r' is the roughness coefficient specified by the ratio of the size of the overall surface to the surface projected geometrically onto a plane. This indicates that the large roughness can reduce the contact angle, and therefore increase the solid surface energy. We thus endowed the γ_s^+ regions with high surface roughness and remained the smooth surface condition on the γ_s^- regions to mimic the DSA surface state. In detail, the roughness height (K_s) in zero for the γ_s^- surface and in 200 μm for the γ_s^+ surface, default roughness constant, and no–slip boundary conditions were applied. The Coupled algorithm was selected for ensuring pressure–velocity coupling. The implicit under–relaxation Pseudo transient was employed to stabilize the steady–state laminar flow.

To initiate the calculation, we assumed that the velocity of the flow inlet was consistent with the slit–coating speed (10 cm s^{-1}) because the driving force is much greater than the surface friction. The resultant velocity distribution revealed that the liquid flow decelerates at the liquid–solid interface with low surface energy and accelerates at the interface with high surface energy (**Figure 5.3(i)**). This difference can be attributed to the low shear force at the γ_s^- regions and the high shear force at the γ_s^+ regions.[136] Because of the variations in the velocity field, the flow compresses and then decompresses over the γ_s^- regions, indicating that the DSA substrate drags the flow toward the γ_s^- region and lifts the flow at the γ_s^+ region (**Figure 5.3(ii)**). Consequently, the dispersed AgNWs selectively align on the γ_s^- regions under the resultant force of the gravitational force and weakened velocity–field–induced inertia force, and drift from the γ_s^+ regions owing to the increased inertia force (**Figure 5.3(iii)**). Thus, the microflow velocity field at the liquid–solid interface, which is responsible for guiding the movement of the dispersed AgNWs, was effectively manipulated.

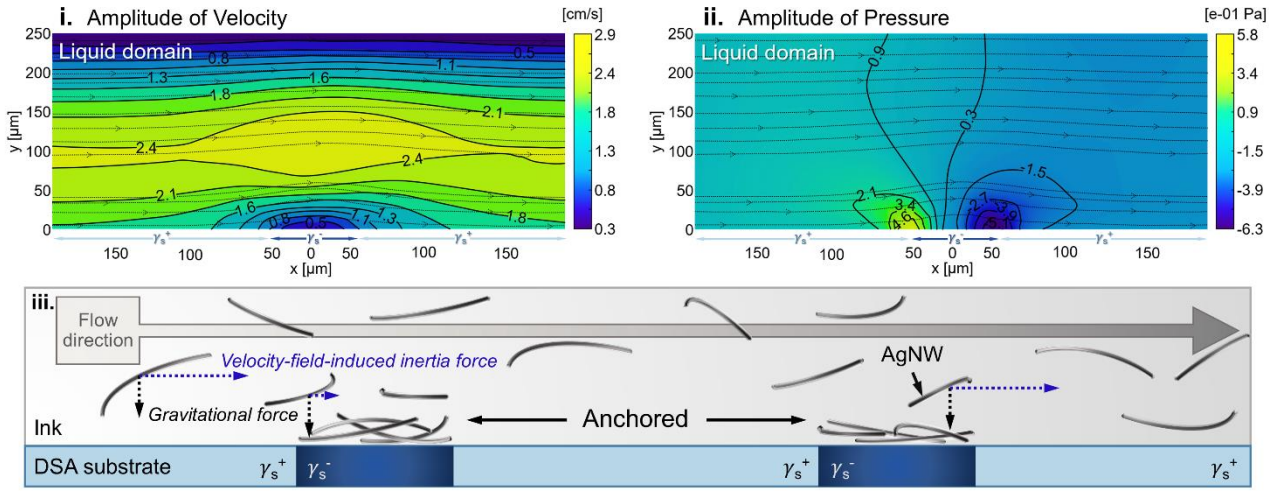

Figure 5.3. Results of the simulations (i,ii) and schematic (iii) of the microflow velocity–field–induced alignment of AgNWs in the cross–border solution layer on the DSA substrate. In the simulation graphs, the lines with arrow heads represent the internal microflow path lines, while the thick lines represent the contour plots.

To initiate the directed 1D NW self–assembly, the cross–border overlaying of the functional solution is a critical

prerequisite. Because the AgNWs effectively lower the surface tension of the liquid functional ink(γ_l), the liquid domains coalesce with each other under capillary force,[137] leading to the formation of a cross–border solution layer irrespective of the surface states of the DSA substrate (**Figure 5.4 a**). In detail, we dispersed the different aspect ratios of AgNWs with the same width (50 nm) and the varied length ranging from 50 nm to 100 μm into the water, resulting in a series of the aqueous AgNW functional inks with a concentration of 20 wt.%. As shown in **Figure 5.4 b**, the contact angle and the γ_l decreased with the gradual increase of the AgNW length, revealing that γ_l can be manipulated effectively by regulating the profiles of AgNWs.

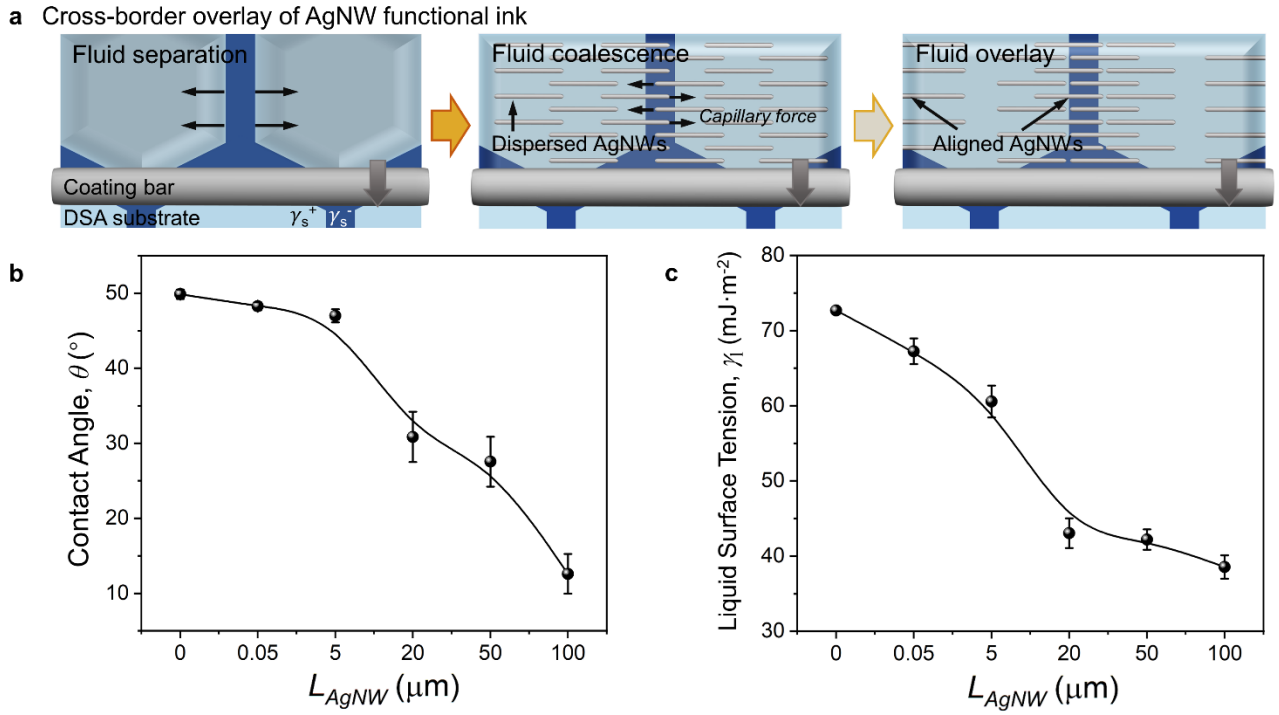

Figure 5.4. (a) Illustrations of the cross–border overlay of a AgNW solution on the DSA substrate. Effect of AgNW profiles toward the liquid surface tension (γ_l) of the functional inks: (b) Temporal dependence of the characteristic θ profiles and (c) Temporal dependence of the characteristic γ_l profiles. Error bars indicate standard deviations of the results for five independent samples.

After the initial anchoring of AgNWs via the instantaneous flow field, the remaining dispersed AgNWs, which drift under Rayleigh–Bénard convection and Marangoni convection in opposite directions (**Figure 5.5**), continue to stack on the already anchored AgNWs at the γ_s^- regions, resulting in the spontaneous formation of an AgNW circuit in a layer–by–layer manner.

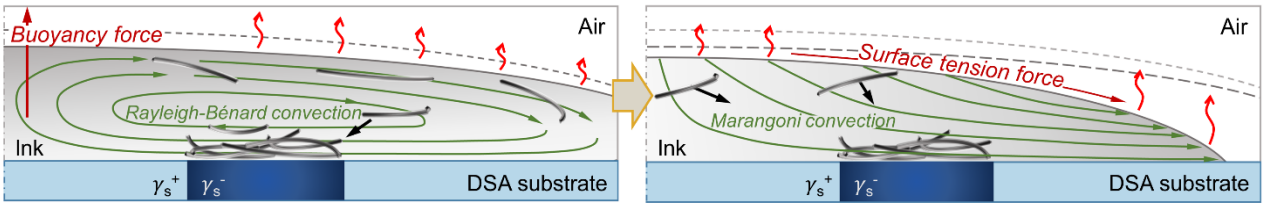

Figure 5.5. Subsequent selective AgNW stacking on the γ_s^- region drifted in Rayleigh–Bénard convection (left) and

Marangoni convection (right) during room–temperature evaporation.

The dynamics of the flow has been illustrated by particle image velocimetry (PIV), as shown in **Figure 5.6**. The PIV analysis was conducted using video images from the OM observation (**Figure 5.2**). Each image is correlated with its successor image, and the velocity contours for each time frame is constant. As soon as the AgNW functional ink spread over the DSA substrate, the dispersed AgNWs overlaid the entire substrate with no directional movement (**Figure 5.6(i)**). For the next two seconds, several slight displacements were found to gather around the γ_s^- regions at a low velocity, leading to the spontaneous alignment of the dispersed AgNWs under the instantaneous flow field generated by slit–coating process (1st stacking, **Figure 5.6(ii)**).

After a few more seconds, an internal flow was observed undergoing the rapidly directional movement from right to left, which is perpendicular to the coating direction (**Figure 5.6 iii**). The phenomenon might be related to the Rayleigh–Bénard convection during the room–temperature evaporation. Strikingly, the flow was observed to be decelerated over the γ_s^- regions, indicating the layer–by–layer alignment behavior triggered by the DSA substrate (2nd stacking).

One minute later, the internal flow changed in the reversed left–to–right direction with the same deceleration phenomenon over the γ_s^- regions (3rd stacking, **Figure 5.6(iv)**). The opposite direction can be explained by the gradually strengthened Marangoni convection. One more thing to stress here is that the alignment ability of the DSA substrate still existed, which guarantees a reliable and precise layer–by–layer self–assembly property during the entire patterning process. The Marangoni convection continued to drift the AgNWs until the solution layer dried completely (**Figure 5.6(v–vi)**).

The PIV results show that during the directed self–assembly of the dispersed AgNWs, the flow direction experienced a three–stage variation. Furthermore, the deceleration behaviors over the γ_s^- regions can be observed in all three stages. These two observations not only exhibit the prominent layer–by–layer self–assembly property for fabricating the high–performance AgNW circuits but also imply the formation of cross–linked AgNW network, which will be detailed discussed in Section 5.2.4.

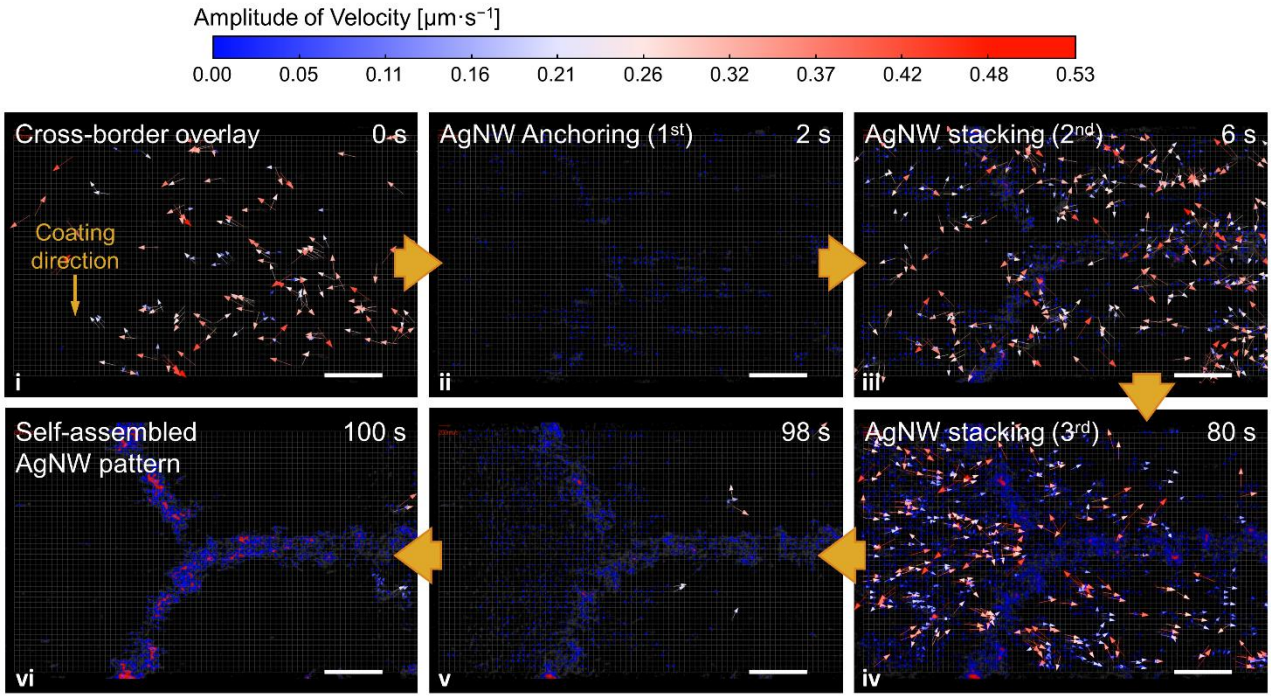

Figure 5.6. Velocity contours and vector plots for internal microflow visualization employing particle image velocimetry (PIV) in the cross–border overlaid AgNW solution layer on the DSA substrate. Scale bars: 200 μm.

5.2.3 Manipulation of onside patterning of dispersed AgNWs

The surface energy difference between the γ_s^+ regions and the γ_s^- regions on the DSA substrate is critical for manipulating the liquid−solid interfacial velocity field and precisely patterning the dispersed functional materials. According to the experimental conditions, a 3D simulation scenario was created to restore the internal microflow in the cross–border solution layer over the honeycomb–structured DSA substrate and emphatically explore the velocity field at the liquid–solid interface. As shown in **Figure 5.7**, the 3D simulation scenario was built with symmetric boundary conditions according to the dimension in the existing proposed system and meshed with hexahedral volume elements. The meshed geometry was exported to solve the viscous equations governing the balance of velocity, momentum, and transport of the internal microflow.

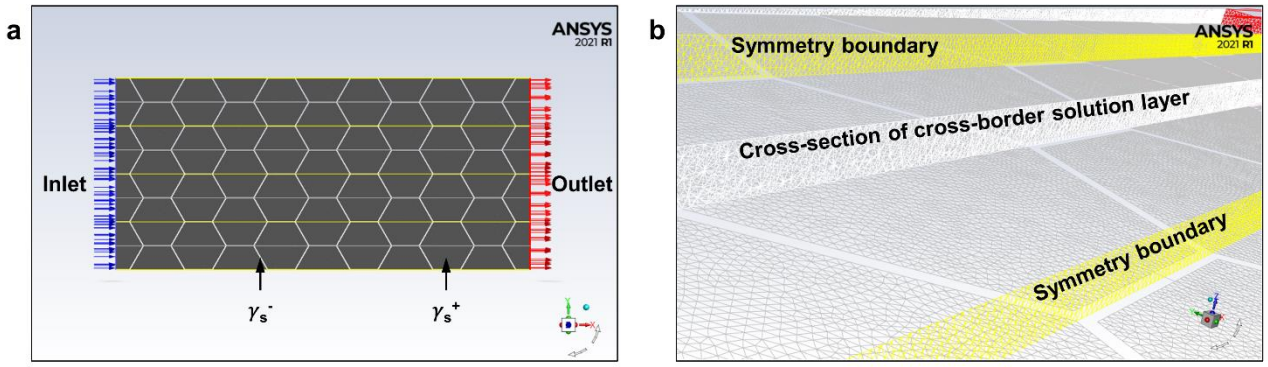

Figure 5.7. Meshed geometry of the 3D simulation scenario.

Instead of the translational periodic boundary condition, constant inlet mass flow with a velocity magnitude of

10 cm s^{-1} and constant outlet outflow were applied to simulate the actual flow state during the directed self–assembly process. Pressure–velocity terms were coupled using semi–implicit pressure linked equations (SIMPLE) algorithm. Gradient was discretized using the green–gauss cell based method. Convective terms in the momentum–conservation equations were discretized using the second–order upwind scheme. For defining the boundary conditions at the liquid–solid interface, because of the relationship between K_s and γ_s as $K_s \propto \gamma_s$, the ratio of the K_s on either surface region can be adjusted to imitate the numerical γ_s difference on the DSA substrate. Hence, we assigned an increasing K_s from 25 to 250 μm to the hexagonal γ_s^+ regions and gave a constant K_s of 25 μm to the γ_s^- regions with no–slip shear conditions for constructing the surface energy difference in the simulations.

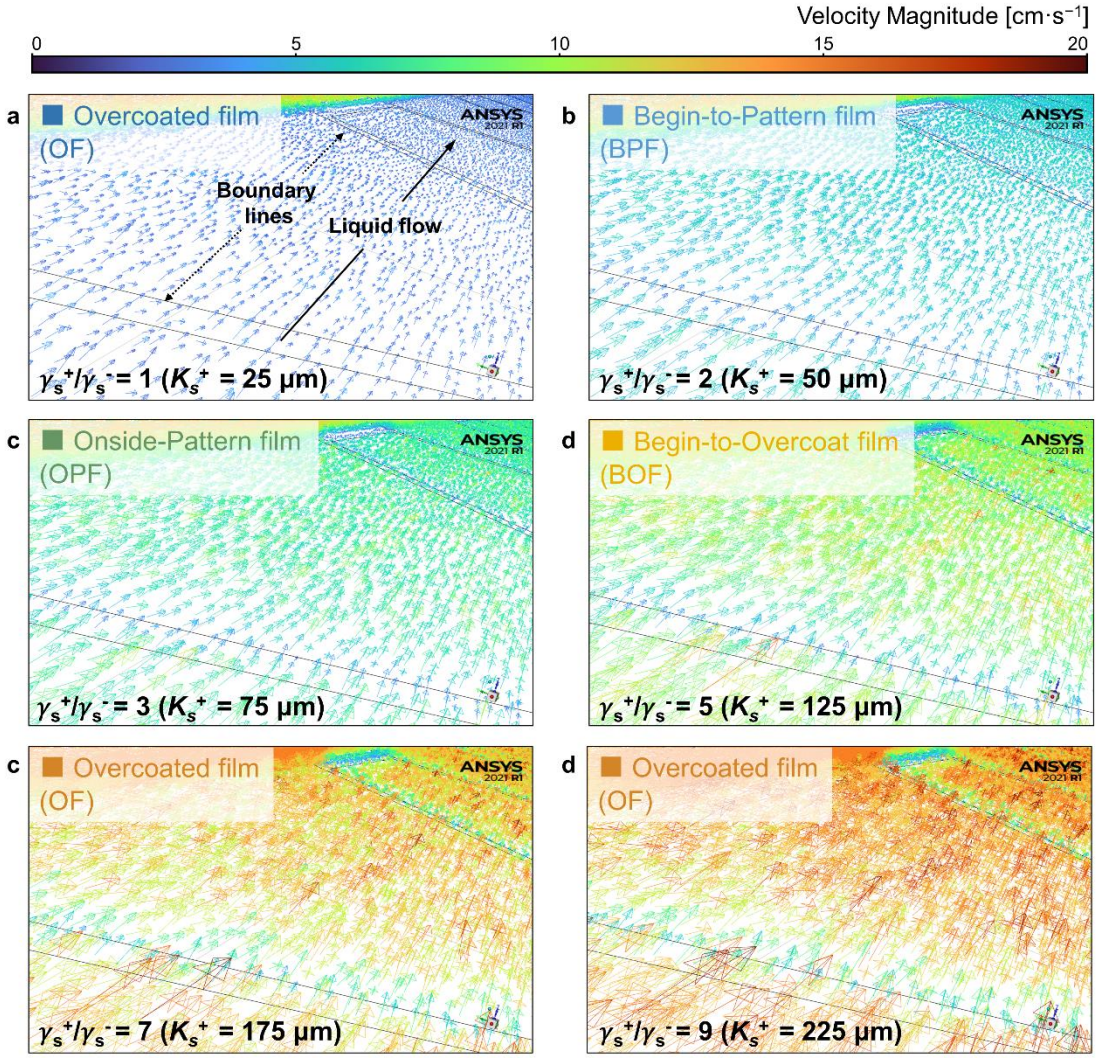

Figure 5.8. Quantitative simulation of microflow velocity gradient at the interface of the water and the DSA substrate. The surface energy ratio of γ_s^+/γ_s^- is used to regulate the γ_s difference on the DSA substrate.

By regulating the surface energy difference, we studied the flow movement at the liquid–solid interface over the simulated DSA substrates and computed the area–weighted average velocity gradient on both γ_s^+ and γ_s^- regions to study the impact toward the alignment of the dispersed AgNWs (**Figure 5.8 and 5.9**). The quantitative simulations revealed that an onside–pattern film (OPF) with zero velocity gradient in the γ_s^+ regions can only be achieved at an

appropriate surface energy ratio (γ_s^+/γ_s^-) of 3, indicating that the increased speed generated by the strong shear stresses at the γ_s^+ regions can be efficiently offset by the low shear stresses at the γ_s^- regions. An excessively small surface energy difference, which induces a negative velocity gradient at the γ_s^+ regions, fails to generate sufficient shear stresses against the surface friction, leading to an overcoated film (OF) or a begin–to–pattern film (BPF). An excessively large surface energy difference with a positive velocity gradient, on the other hand, produces an excess shear force that flushes the liquid from the γ_s^- regions, leading to a begin–to–overcoat film (BOF) or an OF. Taken together, these results elucidate that with the proper γ_s contrast, the distribution of the interfacial velocity can be varied periodically with constant acceleration and deceleration corresponding to the designated γ_s^+ and γ_s^- regions on the DSA substrate.

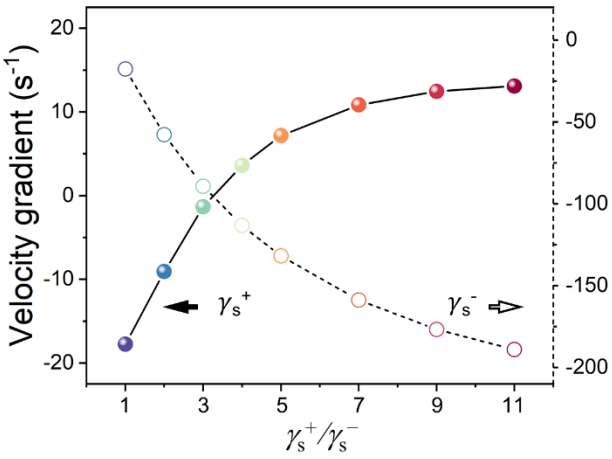

Figure 5.9. Calculated velocity gradient over the γ_s^+ regions and the γ_s^- regions as a function of the increased γ_s^+/γ_s^- ratio.

According to the simulation results, we regulated the surface energy of the substrate via DSA strategy and overcoated it with a functional ink consisting of AgNWs with a diameter and length of 50 nm and 50 μm, to explore the onside–pattern self–assembly feature. In detail, The COP substrates were treated by the PVUV exposure with increasing exposure time and then rinsed with an alkaline solution to fabricate the DSA substrates with varied surface energy difference. The contact angle observations were used to intuitively reflect the γ_s of the modified COP substrates (**Figure 5.10**). The pristine COP substrate exhibited a large contact angle (96.7 °), verifying the low γ_s. The contact angle decreased gradually with prolonging the PVUV exposure, corresponding to the increase of the γ_s. The rapid variation can be contributed by the surface oxidization, polarization, and surficial roughness enhancement by the proposed DSA strategy.

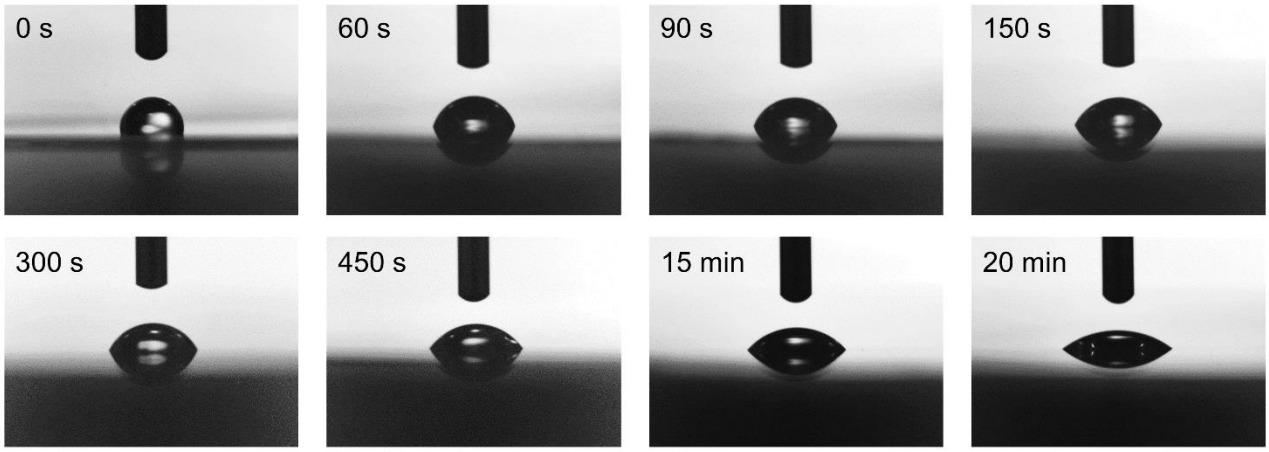

Figure 5.10. Corresponding contact angle measurement of the COP substrates with a 2.0 μL water droplet affected by the DSA strategy.

At the same time, we used the dyne pen to detect the specific value of the solid surface energy on the modified substrate. As shown in **Figure 5.11**, the pristine COP substrate exhibited a low γ_s of about 29.7 mJ m^{-2}. With the increase of the PVUV exposure time, the γ_s has been increased gradually, which is consistent with the contact angle characterization. The largest γ_s, about 56.1 mJ m^{-2}, was achieved by modifying the COP substrate with 1200 s PVUV exposure. Based on the upward trend, the higher γ_s is expected to be obtained by further prolonging the PVUV exposure time for generating the stronger velocity–field–induced inertia force.

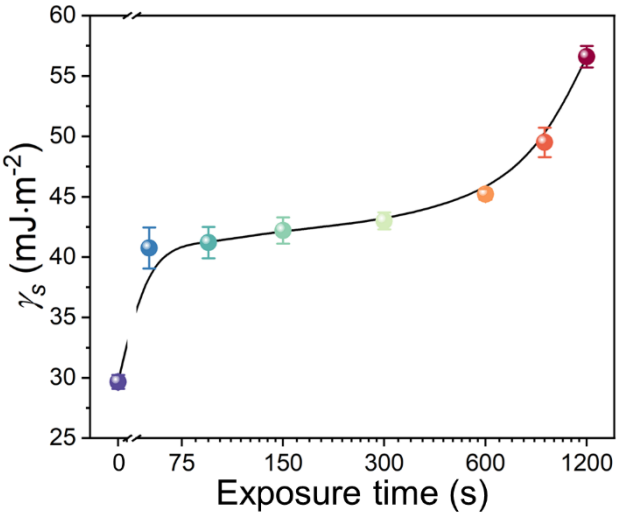

Figure 5.11. Variation of the γ_s as a function of the PVUV exposure time. Error bars indicate standard deviations of the results for five independent samples

After overcoating the AgNW functional ink above the DSA substrate with gradually enlarged γ_s difference, the morphologies of the self–assembled AgNW patterns have been observed systematically. As shown in **Figure 5.12**, the optimal surface energy for fabricating an AgNW OPF is 42.2 mJ m^{-2} at the γ_s^+ regions when 150 s of PVUV exposure is performed and 29.7 mJ m^{-2} at the γ_s^- regions, which can be attributed to the formation of the cyclically

changed interfacial velocity field. Furthermore, the excessively small γ_s difference using the PVUV exposure less than 150 s cannot generate enough velocity–field–induced inertia force to precisely pattern the dispersed AgNWs onto the γ_s^- regions. On the other hand, the excessively large γ_s difference exerts too much driving force, which flushes the AgNWs away from the designated regions and leave the faint patterns. Overall, these experimental results indicate that the precision of the AgNW patterns can be obtained efficiently.

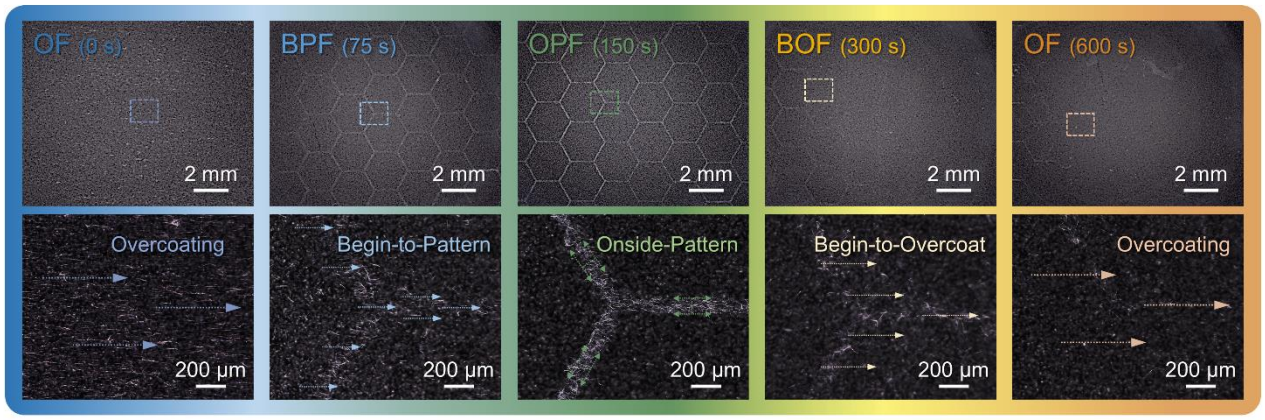

Figure 5.12. Optical microscopy (OM) images showing the different states of the self–assembled AgNW circuits with increasing PVUV exposure time.

Besides patterning the AgNWs with the diameter of 50 nm and the length of 50 μm, two other kinds of AgNWs with the same diameter but different lengths of 20 to 100 μm were used to explore the technical reliability and versatility of the proposed directed self–assembly system. The detailed information of the contact angle and the liquid surface tension of the AgNW functional inks affected by the dispersed AgNW length have been illustrated in **Figure 5.13 a and b**.

In the case of 20–μm–length AgNWs as shown in **Figure 5.13 c**, the PVUV with an exposure time of 110 s left an inadequate acceleration at the activated regions, causing the AgNWs stacked at the rear of the γ_s^- regions and thus forming a BPF. The long exposure time of PVUV (130 s) generated an excessive amount of shear force, which pushed the AgNWs out of the γ_s^- regions and left a BOF film. Only with the 120 s PVUV exposure can achieve an OPF, indicating that the acceleration by the γ_s^+ regions counteracted the deceleration by the γ_s^- regions, and the dispersed AgNWs can be therefore aligned on the γ_s^- regions precisely.

Furthermore, for longer AgNWs with a length of 100 μm, stronger shear stress is required to generate a more intensive velocity–field–induced inertia force for transporting the heavier functional materials. In detail, we have prolonged the PVUV exposure to 200 s for achieving an OPF (**Figure 5.13 d**). The PVUV exposure with shorter (190 s) and longer (210 s) left a BPF and BOF, respectively. This feature can be attributed to the shape effect of the dispersed AgNWs with greater weight and larger surface area, which is expected to be further clarified in follow–up studies. Together these results suggest that the proposed directed self–assembly strategy is promising for controllably patterning a variety of 1D functional micro–/nanomaterials by simply regulating the γ_s contrast of the utilized substrate.

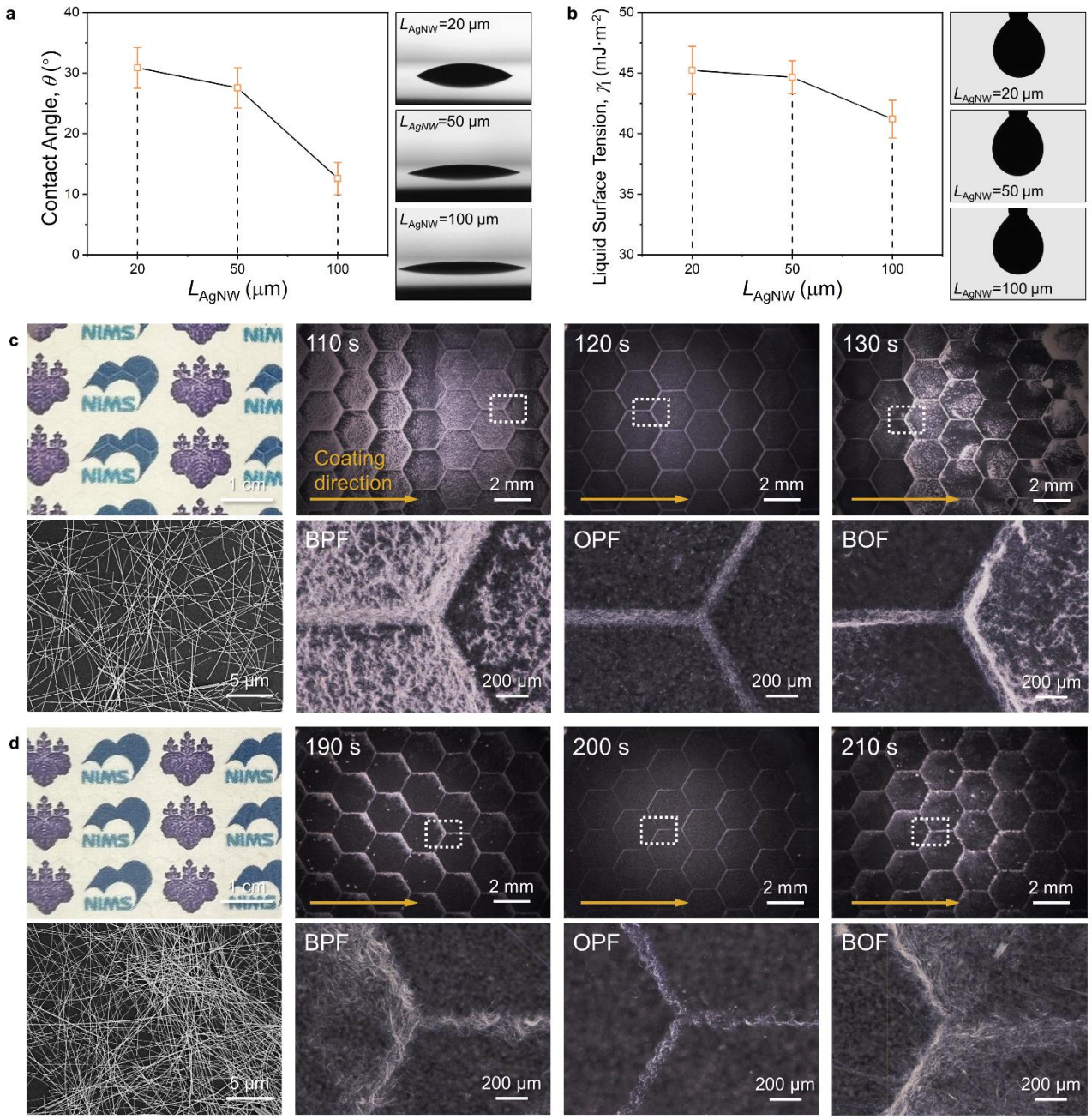

Figure 5.13. (a and b) Temporal dependence of the characteristic θ and γ_l and the corresponding measurement using a 5.0 μL droplet of AgNW functional ink with different AgNW length. Error bars indicate standard deviations of the results for five independent samples. (c and d) Digital (upper left), SEM (lower left), and OM images of the self–assembled AgNW patterns with different AgNW length.

It is worth mentioning that the concentration of the functional ink has little effect on the directed self–assembly behavior in the proposed system. In detail, we chose the AgNWs with 50 nm in diameter and 50 μm in length, and dispersed the different amounts of the AgNWs into the water to prepare the AgNW functional inks with different concentrations of 5 and 20 wt. %, respectively. Next, the formulated inks were overcoated onto the DSA substrates after 150 s PVUV exposure. After room–temperature evaporation, the AgNWs in both cases were observed to be

aligned on the γ_s^- regions selectively, resulting in the self–assembled OPFs (**Figure 5.14 a and b**). Just the patterned AgNW network formed by the 5 wt.% functional ink was loosely aligned, while that using 20 wt.% functional ink exhibited a dense alignment. These observations suggest that the on–side patterning behavior is mainly determined by the velocity–field–induced inertia force.

On the other hand, the functional inks with the silver nanoparticle (AgNP) solutes (**Figure 5.14 c**) and the alcohol solvent (**Figure 5.14 b**) all failed in forming continuous functional patterns and left the isolated aggregations of the functional materials on the γ_s^+ regions after evaporation. These can be attributed to the lack of capillary force in the water–based AgNP ink, as well as the low liquid surface tension in the alcohol–based AgNW ink–. Further studies are needed to confirm the critical factor for controlling the solute movement in a continuously changing microflow field. In detail, the effect of functional solvent and solute species such as CNTs or AuNWs dispersed in alcohol or isopropanol (IPA) toward the spontaneous patterning behavior in the microflow field are planned to be discussed. Moreover, we are also looking for an optimized microscopically observation technique, which can provide high–resolution viewing angles toward the liquid–solid interface without producing heat.

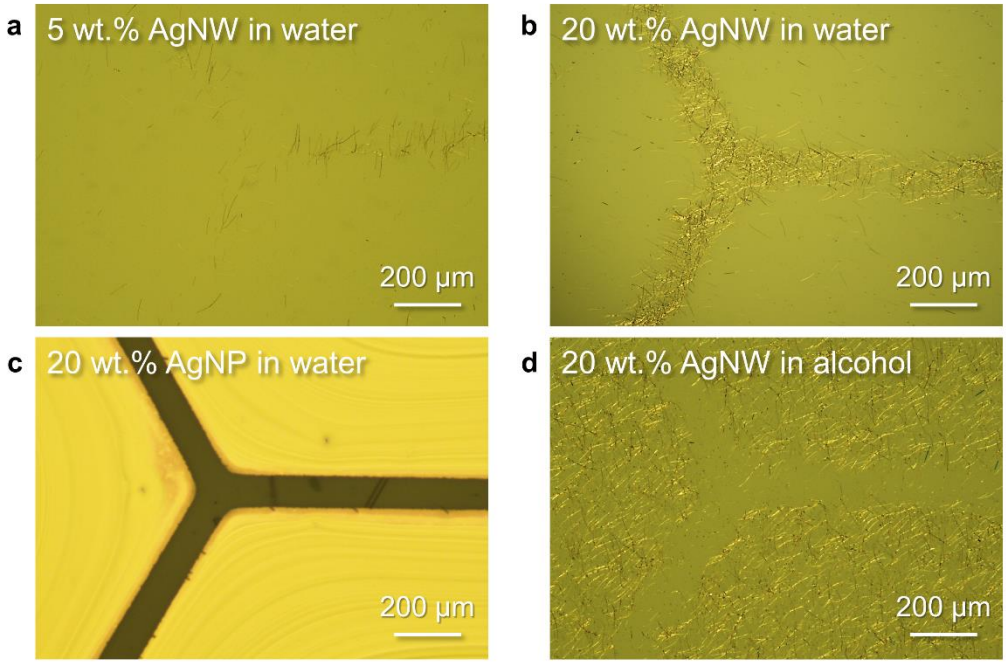

Figure 5.14. OM observations of the self–assembled patterns on the DSA substrates using different functional inks, (a) 5 wt.% water–based AgNW ink, (b) 20 wt.% water–based AgNW ink, (c) 20 wt.% water–based silver nanoparticle (AgNP) ink, and (d) 20 wt.% alcohol–based AgNW ink. The DSA substrates were all modified with 150 s PVUV exposure and 30 s alkali rinsing. The diameter and length of the AgNWs are 50 nm and 50 μm. The particle size of the AgNP is from 10 to 30 nm.

5.2.4 Layer–by–layer alignment of directly self–assembled AgNW network

The topography of the AgNW network during its three–stage alignment process was systematically studied by *in situ* OM observation and the corresponding orientation analysis. When the AgNW functional ink was overlaid on the DSA substrate, the dispersed AgNWs aligned themselves on the γ_s^- region, in a direction parallel to the coating

direction under the instantaneous flow field (**Figure 5.15 a(1st)**). As the room–temperature evaporation of the cross–border solution layer proceeded, buoyancy–induced flow occurred in the self–assembly system,[48] triggering a clockwise Rayleigh–Bénard convection that aid the alignment of the AgNWs on the γ_s^- region (direction describing the flow field in the central–right half of the liquid layer, **Figure 5.15 a(2nd)**). Because the volume of the cross–border solution layer was diminished as the liquid evaporated, the buoyancy–induced flow weakened and a counterclockwise Marangoni convection caused by the surface tension difference dominated the microflow field,[138] inducing the alignment of the AgNWs on the γ_s^- region in a direction opposite that induced by the Rayleigh–Bénard convection, and thus generating a unique cross–linked network structure (**Figure 5.15 a(3rd)**).

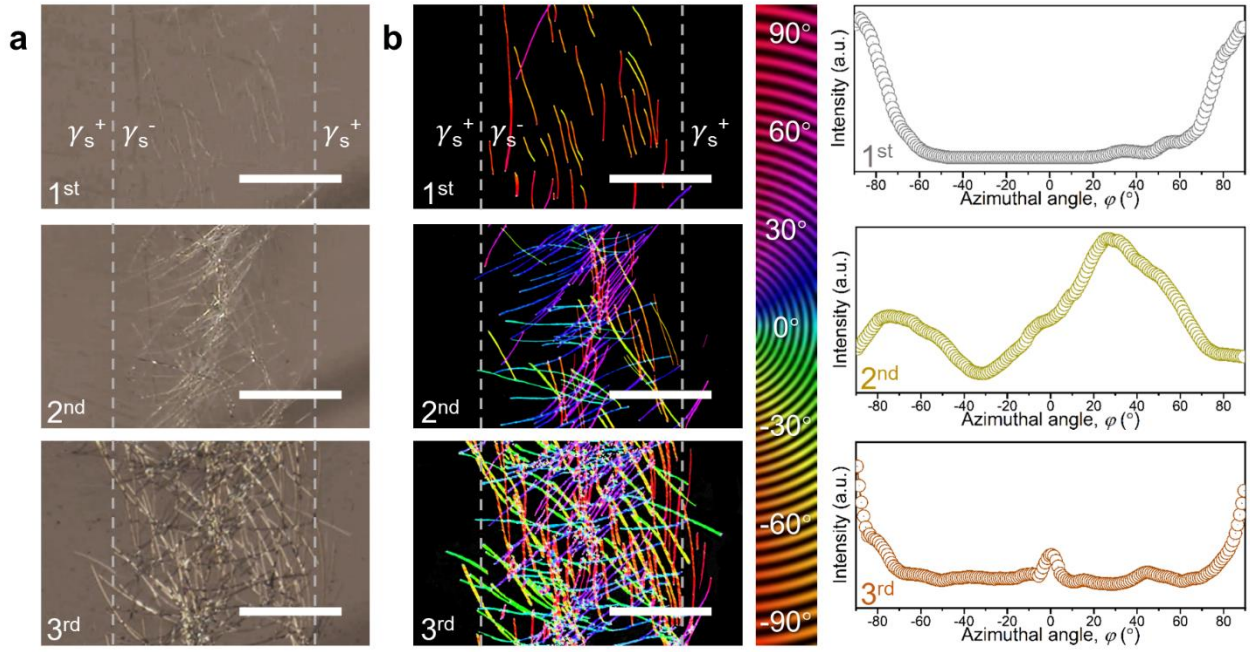

Figure 5.15. Investigation of the layer–by–layer NW alignment in the directed self–assembly of AgNW networks. (a) Time–resolved spontaneous patterning of the dispersed AgNWs on a DSA substrate. The DSA substrate trapped the dispersed AgNWs three times according to the three–stage redirected flowing, generating a cross–linked AgNW network. Scale bars: 50 μm. b) Color–coded OMs (left) and plots of the azimuthal angle (φ) of the self–assembled AgNWs (right) during different NW alignment stages.

The oriented alignment of AgNWs was further quantitatively studied based on the angular distribution using color–coded images. The initially anchored AgNWs had an alignment parallel to the coating direction (**Figure 5.15 b(1st)**). The corresponding azimuthal angle (φ) plot shows two peaks at 90° and −90°, indicating that the AgNWs were concurrently drifted by the instantaneous flow over the DSA substrate. The subsequently stacked AgNWs, driven by the Rayleigh–Bénard convection and Marangoni convection, had a perpendicular alignment, and a gradually shifted φ plot was obtained with three peaks at −90°, 0°, and 90° (**Figure 5.15(2nd) and (3rd)**). Therefore, we could know that the dispersed AgNWs were aligned onto the γ_s^- regions repeatedly, leading to a cross–linked AgNW network. The schematics for the layer–by–layer alignment have been further illustrated in **Figure 5.16**.

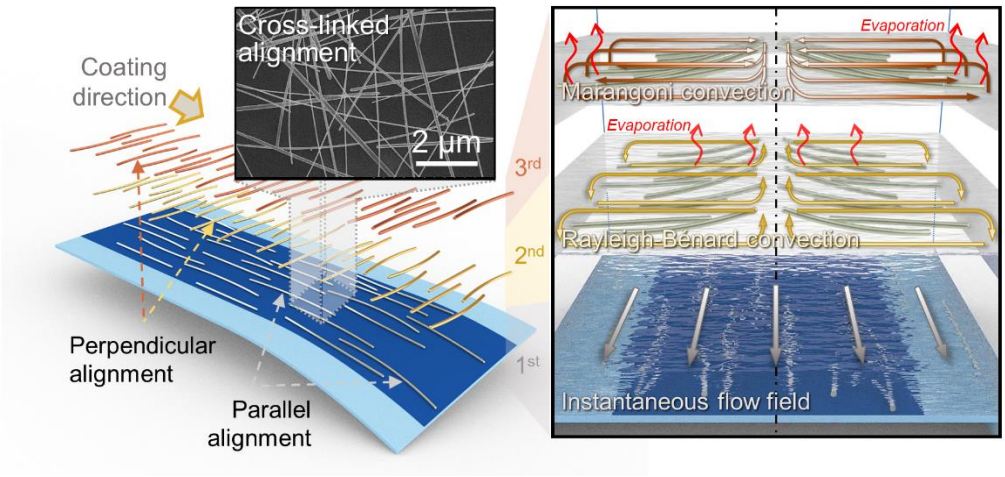

Figure 5.16. Schematics of the three–stage alignment during the directed self–assembly process. Inset: SEM image of the cross–linked AgNW network.

In addition, we studied the situations when the direction of the γ_s^- region was not consistent with the coating direction and when the γ_s^- region was located on the periphery of the circuit. The corresponding topographies and φ plots indicated a highly ordered cross–linked structure in all the self–assembled circuits (**Figure 5.17**). These observations reveal that the proposed directed self–assembly strategy can facilitate layer–by–layer stacking and precise cross–linked fixation of the dispersed functional nanomaterials, which are pivotal for manufacturing self–assembled electronic circuits with high electrical conductivity and high resolution.

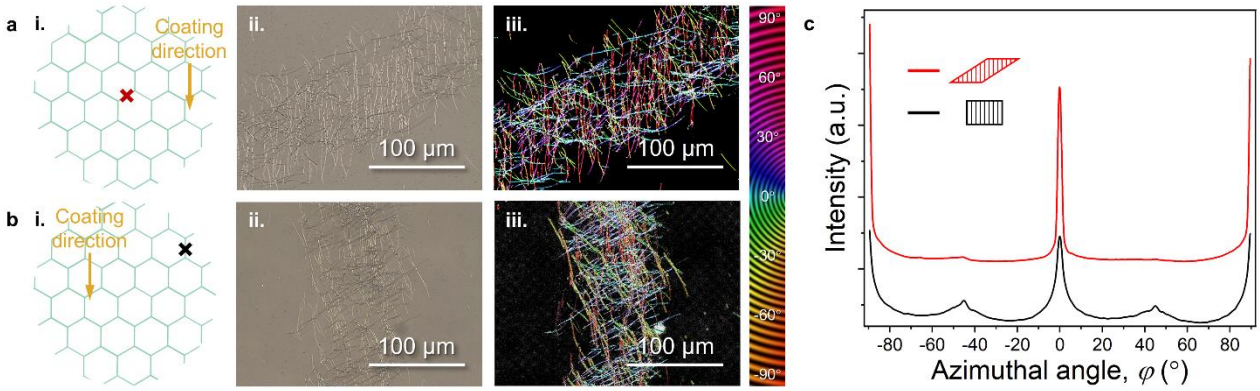

Figure 5.17. Schematics (i), OM images (ii) and color–coded OM images (iii) of the self–assembled AgNW circuits in the circumstances of a) the direction of the γ_s^- region was not consistent with the coating direction and b) the γ_s^- region was located on the periphery of the circuit. c) Comparison of the related azimuthal angle (φ) of the self–assembled AgNWs.

5.2.5 Performance characterizations of patterned AgNW TCs

High–performance flexible TCs were therefore fabricated via the directed self–assembly of AgNW patterns. IPL irradiation was used to evaporate the residual moisture and thus compact the quasi–3D–stacked AgNWs by exploiting the selective heating ability stemming from the strong light absorption by AgNWs.[139–140] The use of

AgNWs with a diameter and length of 50 nm and 50 μm, respectively, and a honeycomb–patterned photomask with 92% open area ratio enabled the directed self–assembly of a honeycomb–structured closed circuit with well–defined boundaries. Strikingly, the use of IPL irradiation significantly improved the electrical performance without affecting the optical properties. By optimizing the optical energy of the IPL irradiation, we achieved high-performance AgNW TCs with a low sheet resistance (29.7 Ω sq^{-1}) and ultrahigh transmittance (98.2% at 550 nm wavelength) (**Figure 5.18 a and b**).

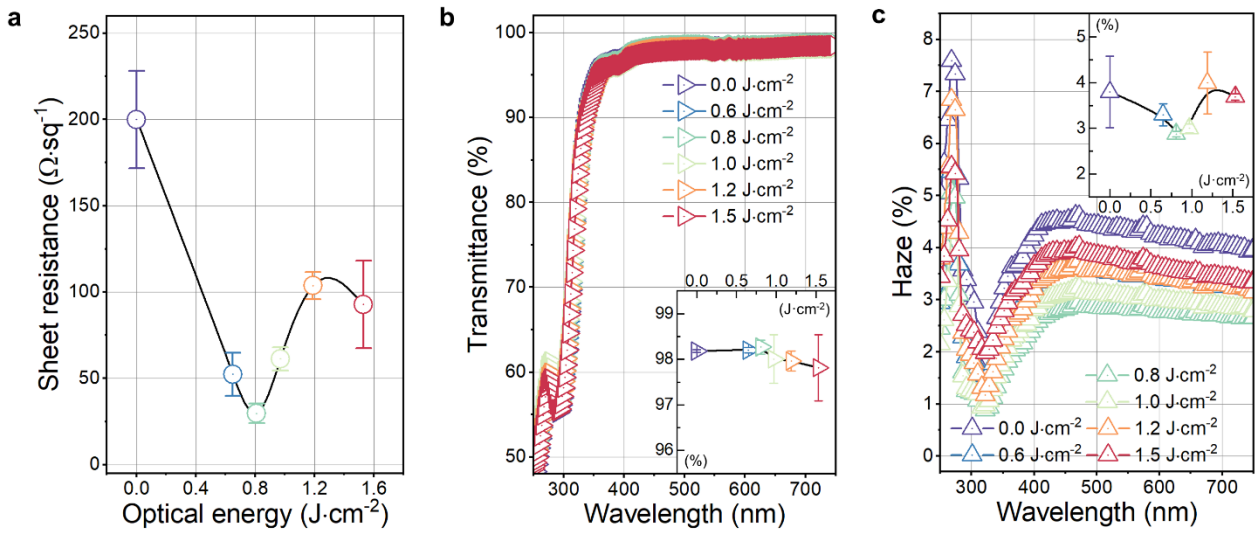

Figure 5.18. Characterization of the patterned AgNW TCs: (a) Electrical performance, as represented by sheet resistance vs. the optical energy under IPL irradiation. Optical properties represented by the transmittance (b) and haze factor (c) as functions of the IPL energy. Inset: values at the wavelength of 550 nm. Error bars indicate standard deviations of the results for six independent samples.

To elucidate the underlying mechanism, we investigated the stacking of the cross–linked AgNW network by quantifying the haze and observing the microscale morphology. As shown in **Figure 5.18 c**, the haze factor, defined as the light scattered by a TC divided by the total light transmittance,[141] gradually decreased at first and then increased with increasing optical energy. When optical energy of 0.8 J cm^{-2} was applied, the AgNW TCs exhibited the lowest haze factor of 2.8%, which corresponds to the best electrical performance, implying that the AgNW arrangement might have changed.

We further inspected the junctions of the patterned AgNW network through inclined SEM observations. Distinct morphological changes toward a more compact network arrangement and fused AgNW junctions confirmed the decreased contact resistance of the AgNW network (**Figure 5.19(i–iii)**), A further increase in the optical energy beyond 0.8 J cm^{-2} led to microfractures and cracks in the NWs, which adversely affect the electrical and optical performances (**Figure 5.19(iv–vi)**). At the same time, the AgNW network was partially embedded in the polymer substrate owing to the IPL–generated local heat,[142] which could facilitate the mechanical stability.

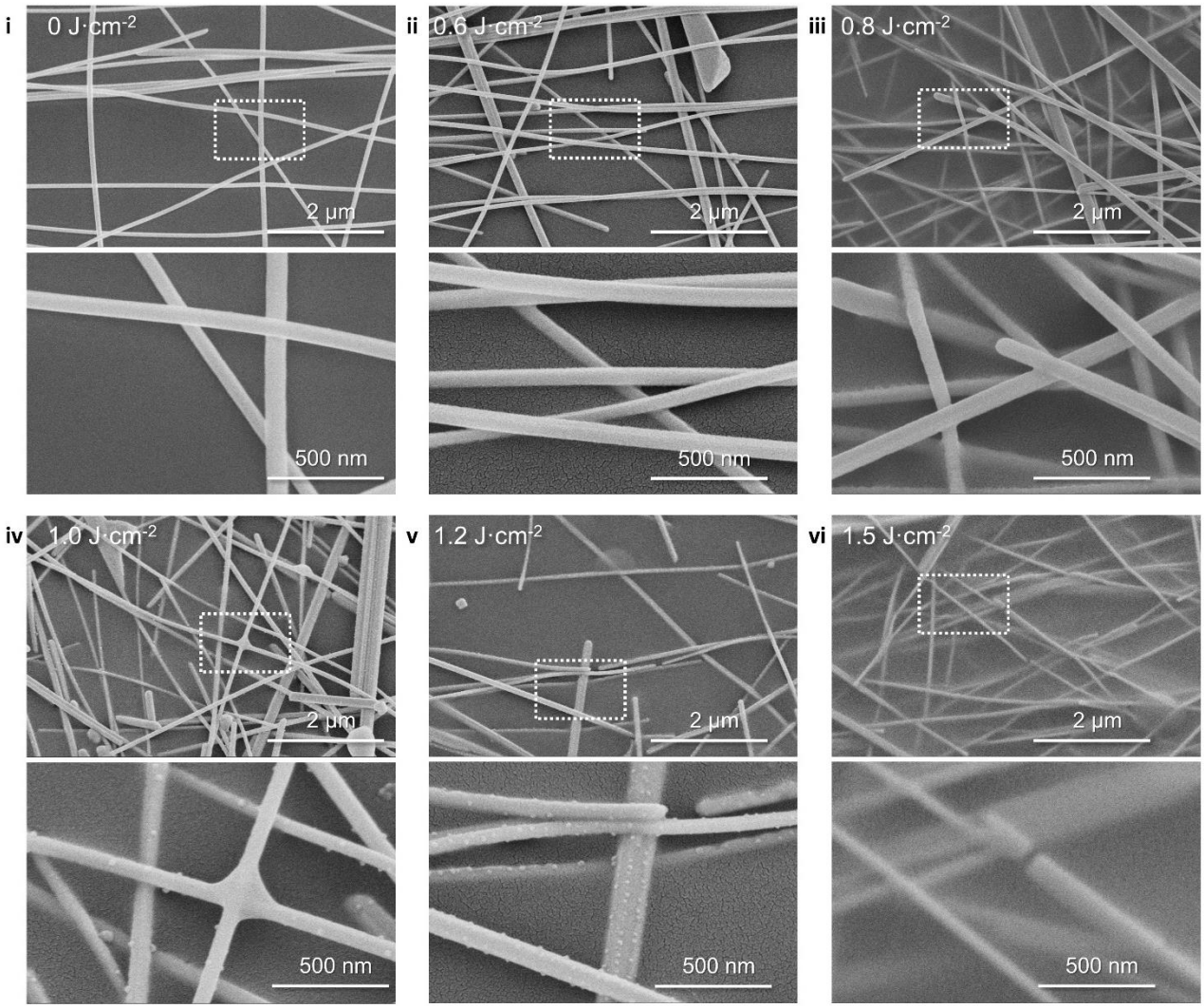

Figure 5.19. Tilted view SEM images of the self–assembled AgNW network after IPL irradiation using different optical energy.

To evaluate the mechanical durability of the self–assembled AgNW TCs, we recorded their resistance variation in real–time under cyclic bending (**Figure 5.20**). We tested the TC by bending the specimen at a speed of 10 r min^{-1} on a motorized stage while both sides of the sample were fixed on tilt clamps (**the inset of Figure 5.20**); this resulted in a radius of concave curvature of 7.5 mm at the maximum bending deformation. The relative resistance (R/R_0) of the as–obtained AgNW TC increased substantially to 9.0 because of the high contact resistance in the AgNW network. Strikingly, a highly reliable R/R_0, less than 0.5 after 5000 bending cycles, was achieved with the sample after IPL irradiation with 0.8 J cm^{-2} energy, confirming enhanced interconnection of the NW network and mechanical anchoring of the nanocomposite on the substrate.[143] A further increase in the optical energy caused a rapid variation of R/R_0 to greater than 5.0 because of structural fractures. Based on these results, we concluded that the TCs composed of 1D AgNWs with extraordinary optical, electrical, and mechanical properties can be readily obtained using the proposed directed self–assembly strategy.

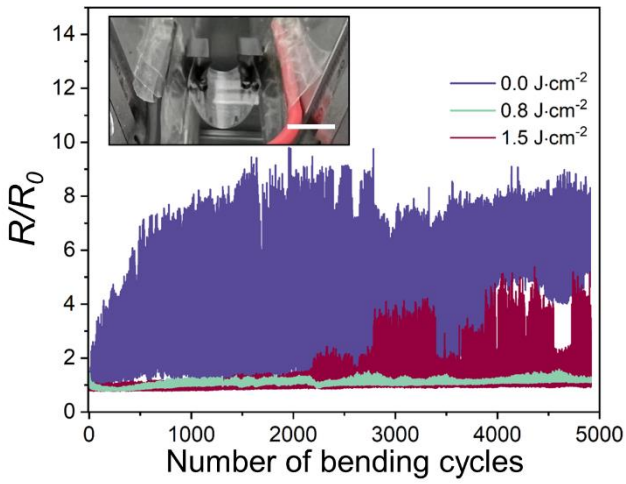

Figure 5.20. Changes in the relative resistance of a self–assembled AgNW TC during cyclic bending (Inset: digital photograph of the sample set–up).

Using the proposed strategy, we also fabricated AgNW TCs with honeycomb structures having different aspect ratios because this material property allows facile control over the optical performance, which is important in the design of optoelectronics.[144] Using photomasks with open area ratios ranging from 89.1 to 96.2%, the haze factors of the self–assembled AgNW patterns were effectively varied (**Figure 5.21 a**). This would enable extensive applications of the AgNW TCs either in solar cells and sensors, which require high haze,[145–146] or in displays and transparent heaters, which require low haze.[147–148] Meanwhile, these self–assembled AgNW TCs exhibited outstanding transmittance and conductivity compared with those of the TCs fabricated using the state–of–the–art NW or even NP patterning technologies (**Figure 5.21 b and Table 5.1**).[63, 66, 123, 150–156]

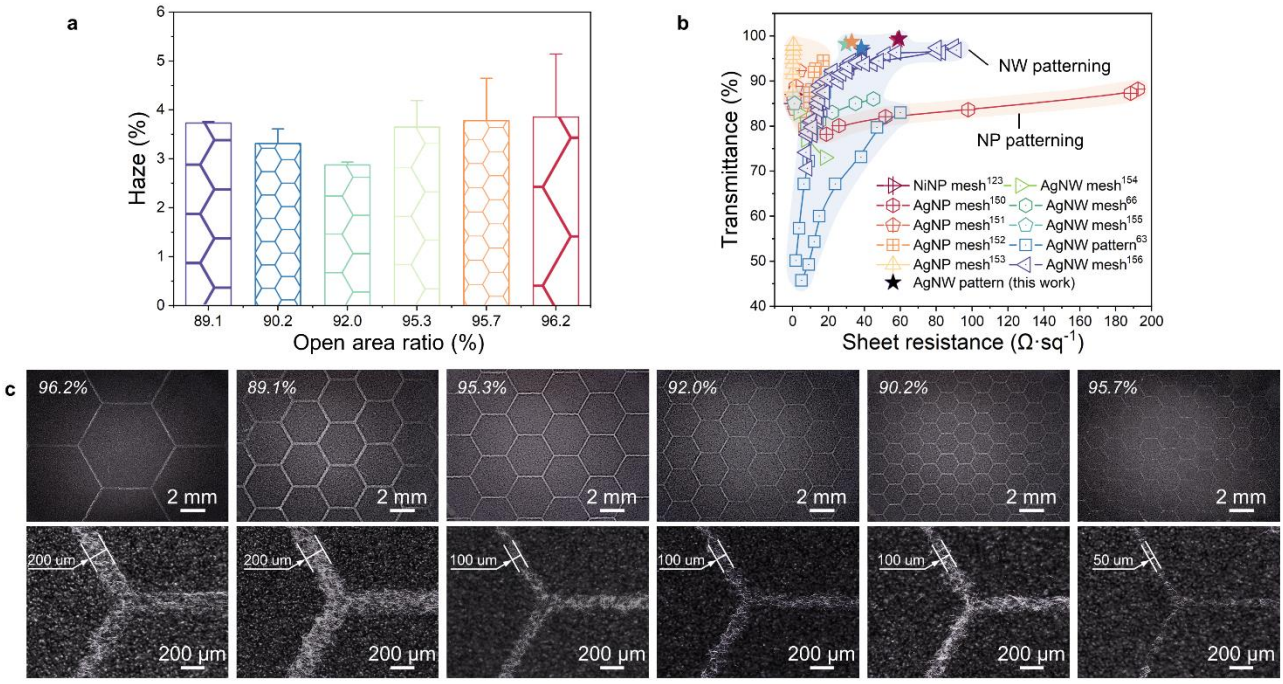

Figure 5.21. (a) Haze factor variation for honeycomb–structured AgNW TCs with open area ratios ranging from

89.1 to 96.2%. Error bars indicate standard deviations of the results for six independent samples. (b) Comparison of the electrical and optical properties of the proposed self–assembled AgNW patterns with those of some NW and NP patterns obtained by the state–of–the–art functional nanomaterial patterning technologies. (c) OM observations of different honeycomb–structured AgNW TCs.

Table 5.1. Comparison of patterned materials, transmittance, conductivity, process, and practical applications between those of some state–of–the–art patterned TCs using additively manufacturing technologies and this work.

Patterned material	Transmittance at 550 nm (%)	Conductivity ($\Omega \cdot sq^{-1}$)	Process	Practical applications	Ref.
NiNP mesh	85–87	0.2–0.5	Selective electrodeposition	Perovskite solar cells	[123]
AuNP grid	86	1.1×10^4 ($S \cdot cm^{-1}$)	Crack–controlled evaporation	Stretchable circuit board	[149]
AgNP mesh	88.2–78.2	192.4–18.8	Ice–templated assembly	/	[150]
AgNP mesh	85.79	0.75	3D printing and hot–embossing	Transparent heater	[151]
AgNP mesh	93.2	17	Reverse–offset printing	Organic photovoltaics	[152]
AgNP mesh	87.5–97.9	0.1–0.4	3D printing and micro transfer	Transparent glass heater	[153]
AgNW mesh	>80	3.2	Elastomer–templated dip–coating	Flexible touch screen panel	[154]
AgNW mesh	~80	8	Leaf skeleton templated dip–coating	Thermotherapy patch	[66]
AgNW mesh	>85	1.0	Elastomer–templated dropping–coating	Stretchable heater	[155]
AgNW pattern	91.0	20	Ice–templated assembly	Touch screen & skin sensor	[63]
AgNW mesh	74.2–97.4	7.5–80.3	laser nanowelding and soft–etching	electromagnetic interference shield	[156]
AgNW pattern	98.2	29.7	Directed self–assembly	Patterned transparent heater	This work

5.2.6 Directed self–assembly of arbitrarily high–accuracy AgNW TCs

Conductors with arbitrarily designed patterns, which are highly desired in practical electronic devices, are challenging to fabricate in a straightforward manner. By simply modifying the shape of the γ_s^+ region using the DSA strategy, we enabled the spontaneous patterning of the AgNWs into various structures ranging from regular

honeycomb–structured meshes to freeform circuits, only by functional ink overcoating and room–temperature evaporating (**Figure 5.22**).

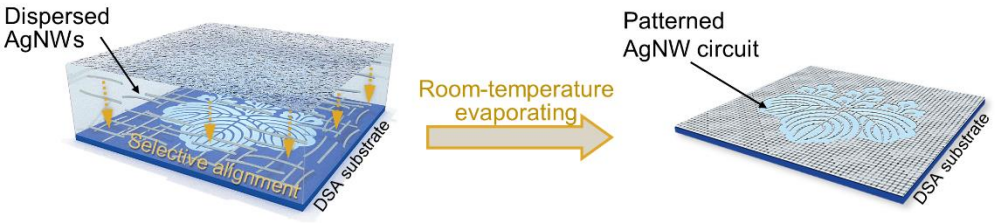

Figure 5.22. Schematic of the fabrication of AgNW TCs with arbitrary electrode designs.

Using the design of customized icons, we spontaneously obtained AgNW TCs with specific patterns. As shown in **Figure 5.23**, delicate AgNW patterns with arbitrary shapes, including irregular curves, straight lines, closed loops, and dots, could be formed on DSA substrates with well–defined boundaries and clear edges. Neither AgNW agglomeration on the γ_s^- regions nor residual AgNWs on the γ_s^+ regions was observed, indicating high–definition patterning of the AgNWs.

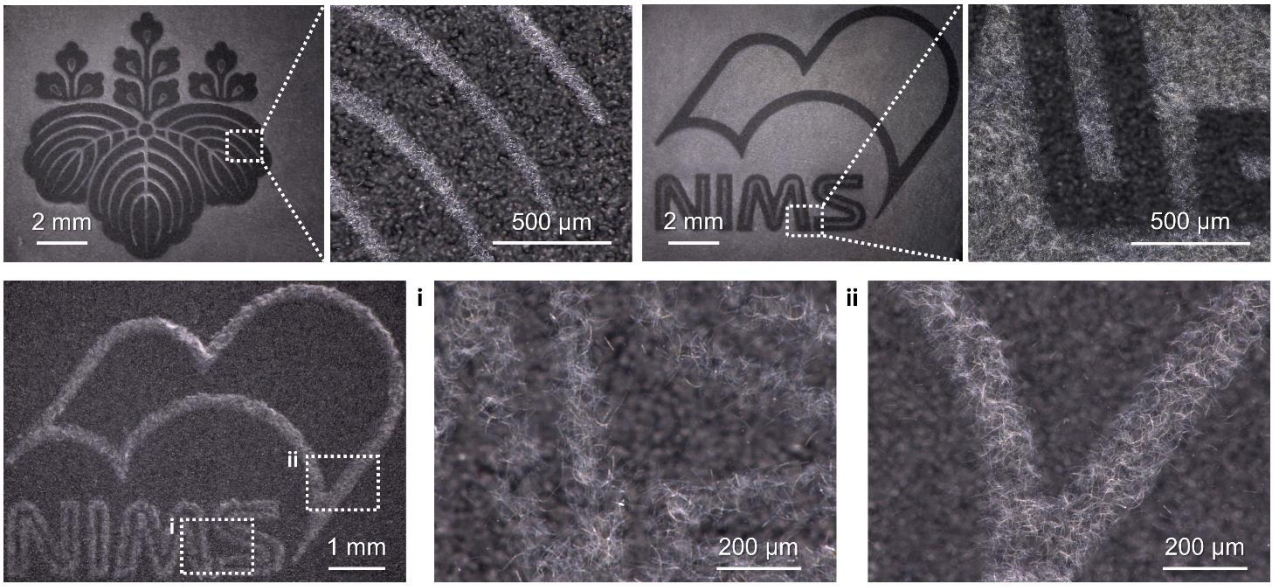

Figure 5.23. Optical images of some high–accuracy arbitrary AgNW patterns.

5.2.7 Application of patterned AgNW TCs as flexible transparent heaters

Here, we demonstrate a flexible transparent heater with adjustable localized heat sources relying on the resistance heat produced by the patterned AgNW circuits. According to Joule's first law ($P = V_a^2 \cdot R^{-1}$), the steady–state temperature increased stably only at the AgNW–patterned areas as the applied voltage (V_a) increased, whereas the γ_s^+ regions on the DSA substrate were maintained at low temperature (**Figure 5.24 a**). The homogeneously generated local Joule heat shown in **Figure 5.24 b** confirms that the proposed patterning technology can facilitate the directional alignment of AgNWs precisely and uniformly with less shape or scale limitations. We observed the temperature rise in the isolated region of the right icon, which can be attributed to a few scattered AgNWs on the

γ_s^+ regions of the DSA substrate. This behavior is expected to be optimized by further increasing the pattern resolution, which we would like to further explore in future.

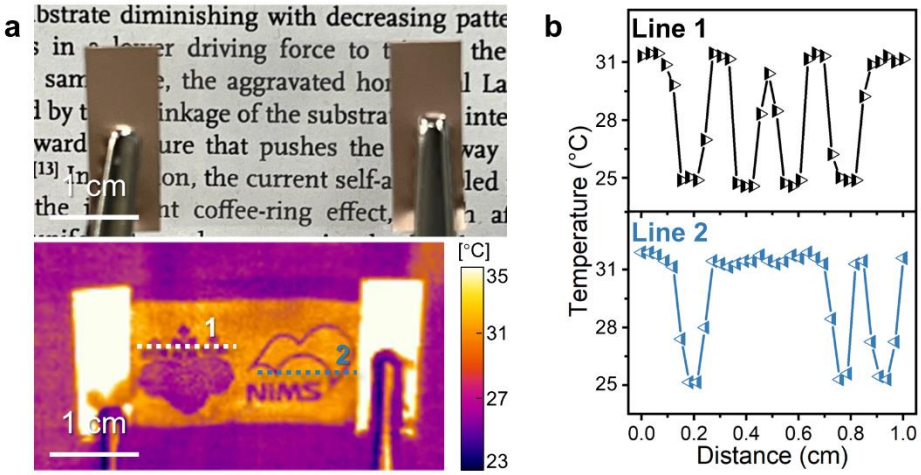

Figure 5.24. (a) Digital photographs and infrared thermal images of patterned AgNW TCs with customized icons at an applied voltage (V_a) of 2 V. (b) Joule heating performance of flexible transparent heaters.

Furthermore, the applicable temperature range of the patterned AgNW transparent heater was up to 105.9 °C, and the maximum temperature can reach 120 °C. As shown in **Figure 5.25 a**, the temperature rising characteristics by resistance heating could be divided into two periods: temperature rising slow uniformly (V_a: 0 to 5 V) and temperature rising fast rapidly (V_a: 5 to 6 V), which are corresponding to the established applicable temperature range and the maximum temperature. In the first period, a sustained temperature rising to around 100 °C and a line relation between V_a and current have been observed, revealing the stable electrical resistance of the patterned AgNW transparent heater (**Figure 5.25 b**). In the second period, the voltage–dependent temperature increased rapidly at first and then decreased sharply. In the meanwhile, the resistance of the AgNW network was observed to increased continuously. This can be explained by the low glass transition temperature (100 °C) of the COP substrate. The excessively high temperature aroused the plastic deformation of the polymer substrate, which caused the fracture in the AgNW network, overheating, and rapid failure of the patterned transparent heater. These observations not only exhibit the rapid thermal responses of the fabricated transparent heaters, but also suggest that the directed AgNW self–assembly strategy is a promising technology for the rapid fabrication of soft electronics with additive manufacturing processability, highly programmable transmittance, and reliable mechanical durability.

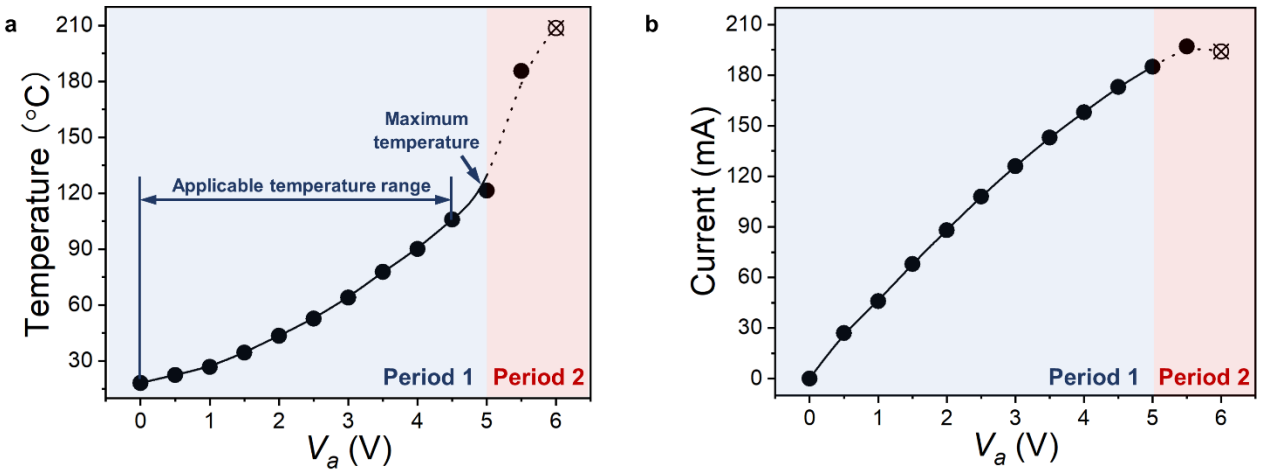

Figure 5.25. Joule heating performance of patterned flexible transparent heaters fabricated from the freeform AgNW TCs. (a) Thermal responses of the transparent heaters at gradually increased V_a. (b) V_a–current relationship of the transparent heaters. The heating rate was controlled by increasing the V_a at 0.5 V per minute.

5.3 Conclusion

We presented a spontaneous AgNW patterning strategy based on microflow velocity–field–induced alignment at the interface between a functional ink and DSA substrate, and demonstrated that 1D AgNWs can be directly assembled in a layer–by–layer fashion to obtain a cross–linked AgNW network with an arbitrary circuit design using this strategy. With appropriate manipulation of the surface energy of the substrate, the AgNWs dispersed in the aqueous ink were patterned on designated areas precisely and repeatedly, resulting in the flexible AgNW TCs with unprecedentedly high transmittance (98.2%, excluding the substrate), low sheet resistance (29.7 Ω sq^{-1}), and reliable mechanical durability. Quantitative analyses indicated that the periodic alignment of NWs was achieved through controllable manipulation of the internal microflow field at the liquid–solid interface owing to the DSA modification. The proposed strategy could be readily extended to align high–performance soft electrodes as customized and freeform circuits, and thus realize the facile prototyping of additively manufactured electronics. We foresee further development of the directed self–assembly technology via microflow velocity–field–gradient manipulation, leading the manufacturing of the highly desired in–plane or advanced 3D soft electronics using diversified functional micro–/nanomaterials.

Reference

[48] C.M. Jin, W. Lee, D. Kim, T. Kang, I. Choi, Photothermal Convection Lithography for Rapid and Direct Assembly of Colloidal Plasmonic Nanoparticles on Generic Substrates, Small. 14 (2018) 1803055. https://doi.org/10.1002/smll.201803055.

[57] J. Xiong, S. Li, J.H. Ciou, J. Chen, D. Gao, J. Wang, P.S. Lee, A Tailorable Spray–Assembly Strategy of Silver Nanowires–Bundle Mesh for Transferable High–Performance Transparent Conductor, Adv. Funct. Mater. (2020) 2006120. https://doi.org/10.1002/adfm.202006120.

[63] J. Han, J. Yang, W. Gao, H. Bai, Ice–Templated, Large–Area Silver Nanowire Pattern for Flexible

Transparent Electrode, Adv. Funct. Mater. 31 (2021) 2010155. https://doi.org/10.1002/adfm.202010155.

[64] B.R. Yang, W. Cao, G.S. Liu, H.J. Chen, Y.Y. Noh, T. Minari, H.C. Hsiao, C.Y. Lee, H.P.D. Shieh, C. Liu, Microchannel Wetting for Controllable Patterning and Alignment of Silver Nanowire with High Resolution, ACS Appl. Mater. Interfaces. 7 (2015) 21433–21441. https://doi.org/10.1021/acsami.5b06370.

[65] T. Tokuno, M. Nogi, J. Jiu, T. Sugahara, K. Suganuma, Transparent electrodes fabricated via the self–assembly of silver nanowires using a bubble template, Langmuir. 28 (2012) 9298–9302. https://doi.org/10.1021/la300961m.

[66] V. Sharma, A. Koivikko, K. Yiannacou, K. Lahtonen, V. Sariola, Flexible biodegradable transparent heaters based on fractal–like leaf skeletons, Npj Flex. Electron. 4 (2020) 27. https://doi.org/10.1038/s41528–020–00091–8.

[67] B. Han, Y. Huang, R. Li, Q. Peng, J. Luo, K. Pei, A. Herczynski, K. Kempa, Z. Ren, J. Gao, Bio–inspired networks for optoelectronic applications, Nat. Commun. 5 (2014) 5674. https://doi.org/10.1038/ncomms6674.

[68] B. Han, K. Pei, Y. Huang, X. Zhang, Q. Rong, Q. Lin, Y. Guo, T. Sun, C. Guo, D. Carnahan, M. Giersig, Y. Wang, J. Gao, Z. Ren, K. Kempa, Uniform self–forming metallic network as a high–performance transparent conductive electrode, Adv. Mater. 26 (2014) 873–877. https://doi.org/10.1002/adma.201302950.

[69] J.H.M. Maurer, L. González–García, B. Reiser, I. Kanelidis, T. Kraus, Templated Self–Assembly of Ultrathin Gold Nanowires by Nanoimprinting for Transparent Flexible Electronics, Nano Lett. 16 (2016) 2921–2925. https://doi.org/10.1021/acs.nanolett.5b04319.

[123] M. Li, W.W. Zuo, A.G. Ricciardulli, Y.G. Yang, Y.H. Liu, Q. Wang, K.L. Wang, G.X. Li, M. Saliba, D. Di Girolamo, A. Abate, Z.K. Wang, Embedded Nickel–Mesh Transparent Electrodes for Highly Efficient and Mechanically Stable Flexible Perovskite Photovoltaics: Toward a Portable Mobile Energy Source, Adv. Mater. 32 (2020) 2003422. https://doi.org/10.1002/adma.202003422.

[124] B.S. Kim, H. Kwon, H.J. Kwon, J.B. Pyo, J. Oh, S.Y. Hong, J.H. Park, K. Char, J.S. Ha, J.G. Son, S.S. Lee, Buckling Instability Control of 1D Nanowire Networks for a Large–Area Stretchable and Transparent Electrode, Adv. Funct. Mater. 30 (2020) 1910214. https://doi.org/10.1002/adfm.201910214.

[125] F. Liang, Y. Chang, C. Kuo, C. Cho, D. Jiang, F. Jhuang, S. Rwei, R. Borsali, A mechanically robust silver nanowire– polydimethylsiloxane electrode based on facile transfer printing techniques for wearable displays, Nanoscale. 11 (2019) 1520–1530. https://doi.org/10.1039/c8nr08819e.

[126] W. Kang, M.F. Lin, J. Chen, P.S. Lee, Highly Transparent Conducting Nanopaper for Solid State Foldable Electrochromic Devices, Small. 12 (2016) 6370–6377. https://doi.org/10.1002/smll.201600979.

[127] S. Lin, X. Bai, H. Wang, H. Wang, J. Song, K. Huang, C. Wang, N. Wang, B. Li, M. Lei, H. Wu, Roll–to–Roll Production of Transparent Silver–Nanofiber–Network Electrodes for Flexible Electrochromic Smart Windows, Adv. Mater. 29 (2017) 1703238. https://doi.org/10.1002/adma.201703238.

[128] C. Chen, Z. Huang, S. Zhu, B. Liu, J. Li, Y. Hu, D. Wu, In Situ Electric–Induced Switchable Transparency and Wettability on Laser–Ablated Bioinspired Paraffin–Impregnated Slippery Surfaces, Adv. Sci. (2021) 2100701. https://doi.org/10.1002/advs.202100701.

[129] D.T. Papanastasiou, A. Schultheiss, D. Muñoz–Rojas, C. Celle, A. Carella, J.P. Simonato, D. Bellet,

Transparent Heaters: A Review, Adv. Funct. Mater. 30 (2020) 1910225. https://doi.org/10.1002/adfm.201910225.

[130] Y. Yang, S. Chen, W. Li, P. Li, J. Ma, B. Li, X. Zhao, Z. Ju, H. Chang, L. Xiao, H. Xu, Y. Liu, Reduced Graphene Oxide Conformally Wrapped Silver Nanowire Networks for Flexible Transparent Heating and Electromagnetic Interference Shielding, ACS Nano. 14 (2020) 8754–8765. https://doi.org/10.1021/acsnano.0c03337.

[131] K.K. Kim, I. Ha, P. Won, D. Seo, K. Cho, S.H. Ko, Transparent wearable three–dimensional touch by self–generated multiscale structure, Nat. Commun. 10 (2019) 2582. https://doi.org/10.1038/s41467–019–10736–6.

[132] J.H.M. Maurer, L. González–García, I.K. Backes, B. Reiser, S.M. Schlossberg, T. Kraus, Direct Nanoimprinting of a Colloidal Self–Organizing Nanowire Ink for Flexible, Transparent Electrodes, Adv. Mater. Technol. 2 (2017) 1700034. https://doi.org/10.1002/admt.201700034.

[133] R. Yoshikawa, M. Tenjimbayashi, T. Matsubayashi, K. Manabe, L. Magagnin, Y. Monnai, S. Shiratori, Designing a Flexible and Transparent Ultrarapid Electrothermogenic Film Based on Thermal Loss Suppression Effect: A Self–Fused Cu/Ni Composite Junctionless Nanonetwork for Effective Deicing Heater, ACS Appl. Nano Mater. 1 (2018) 860–868. https://doi.org/10.1021/acsanm.7b00268.

[134] L. Li, W. Li, K. Tong, J. Jiu, K. Suganuma, Intense Pulsed Light–Induced Structure–transformed Ultrathin Ni Shell for Improving the Chemical, Thermal, and Electrical Reliability of Metal Nanowire Electrodes without Transmittance Loss, Chem. Eng. J. 390 (2020) 124517. https://doi.org/10.1016/j.cej.2020.124517.

[135] C. Wu, J. Jiu, T. Araki, H. Koga, T. Sekitani, H. Wang, K. Suganuma, Rapid self–assembly of ultrathin graphene oxide film and application to silver nanowire flexible transparent electrodes, RSC Adv. 6 (2016) 15838–15845. https://doi.org/10.1039/C5RA24896E.

[136] L. Li, W. Li, Q. Sun, X. Liu, J. Jiu, M. Tenjimbayashi, M. Kanehara, T. Nakayama, T. Minari, Dual Surface Architectonics for Directed Self–Assembly of Ultrahigh–Resolution Electronics, Small. 17 (2021) 2101754. https://doi.org/10.1002/smll.202101754.

[137] C. Zhao, P. Zhang, J. Zhou, S. Qi, Y. Yamauchi, Layered nanocomposites by shear–flow– induced alignment of nanosheets, Nature. 580 (2020) 210–215. https://doi.org/10.1038/s41586–020–2161–8.

[138] H. Jeong, C. Han, S. Cho, Y. Gianchandani, J. Park, Analysis of Extracellular Vesicles Using Coffee Ring, ACS Appl. Mater. Interfaces. 10 (2018) 22877–22882. https://doi.org/10.1021/acsami.8b05793.

[139] W.H. Chung, S.H. Park, S.J. Joo, H.S. Kim, UV–assisted flash light welding process to fabricate silver nanowire/graphene on a PET substrate for transparent electrodes, Nano Res. 11 (2018) 2190–2203. https://doi.org/10.1007/s12274–017–1837–3.

[140] L. Li, W. Li, J. Jiu, K. Suganuma, Efficient assembly of high–performance reduced graphene oxide/silver nanowire transparent conductive film based on in situ light–induced reduction technology, Appl. Surf. Sci. 459 (2018) 732–740. https://doi.org/10.1016/j.apsusc.2018.08.060.

[141] L. Dou, F. Cui, Y. Yu, G. Khanarian, S.W. Eaton, Q. Yang, J. Resasco, C. Schildknecht, K. Schierle–Arndt, P. Yang, Synthesis of Silver Nanowires with Reduced Diameters Using Benzoin–Derived Radicals to Make Transparent Conductors with High Transparency and Low HazeSynthesis of Silver Nanowires with

Reduced Diameters Using Benzoin–Derived Radicals to Make Transparent C, ACS Nano. 10 (2016) 2600–2606. https://doi.org/10.1021/acsnano.5b07651.

[142] E.C. Garnett, W. Cai, J.J. Cha, F. Mahmood, S.T. Connor, M. Greyson Christoforo, Y. Cui, M.D. McGehee, M.L. Brongersma, Self–limited plasmonic welding of silver nanowire junctions, Nat. Mater. 11 (2012) 241–249. https://doi.org/10.1038/nmat3238.

[143] H. Lee, Y. Li, P. Cui, L. Wang, H. Lee, K. Lee, Highly bendable, conductive, and transparent film by an enhanced adhesion of silver nanowires, ACS Appl. Mater. Interfaces. 5 (2013) 9155–9160. https://doi.org/10.1021/am402578d.

[144] J.J. Patil, W.H. Chae, A. Trebach, K.J. Carter, E. Lee, T. Sannicolo, J.C. Grossman, Failing Forward: Stability of Transparent Electrodes Based on Metal Nanowire Networks, Adv. Mater. 33 (2021) 2004356. https://doi.org/10.1002/adma.202004356.

[145] X. Fan, Doping and Design of Flexible Transparent Electrodes for High–Performance Flexible Organic Solar Cells: Recent Advances and Perspectives, Adv. Funct. Mater. 31 (2021) 2009399. https://doi.org/10.1002/adfm.202009399.

[146] J. Han, S. Yuan, L. Liu, X. Qiu, H. Gong, X. Yang, C. Li, Y. Hao, B. Cao, Fully indium–free flexible Ag nanowires/ZnO:F composite transparent conductive electrodes with high haze, J. Mater. Chem. A. 3 (2015) 5375–5384. https://doi.org/10.1039/c4ta05728g.

[147] J. Xiong, S. Li, Y. Ye, J. Wang, K. Qian, P. Cui, D. Gao, M.F. Lin, T. Chen, P.S. Lee, (s) A Deformable and Highly Robust Ethyl Cellulose Transparent Conductor with a Scalable Silver Nanowires Bundle Micromesh, Adv. Mater. 30 (2018). https://doi.org/10.1002/adma.201802803.

[148] L. Dou, F. Cui, Y. Yu, G. Khanarian, S.W. Eaton, Q. Yang, J. Resasco, C. Schildknecht, K. Schierle–Arndt, P. Yang, Solution–Processed Copper/Reduced–Graphene–Oxide Core/Shell Nanowire Transparent Conductors, ACS Nano. 10 (2016) 2600–2606. https://doi.org/10.1021/acsnano.5b07651.

[149] M. Kong, I. You, G. Lee, G. Park, J. Kim, D. Park, U. Jeong, Transparent Omni–Directional Stretchable Circuit Lines Made by a Junction–Free Grid of Expandable Au Lines, Adv. Mater. (2021) 2100299. https://doi.org/10.1002/adma.202100299.

[150] S. Wu, L. Li, H. Xue, K. Liu, Q. Fan, G. Bai, J. Wang, Size Controllable, Transparent, and Flexible 2D Silver Meshes Using Recrystallized Ice Crystals as Templates, ACS Nano. 11 (2017) 9898–9905. https://doi.org/10.1021/acsnano.7b03821.

[151] X. Zhu, M. Liu, X. Qi, H. Li, Y.F. Zhang, Z. Li, Z. Peng, J. Yang, L. Qian, Q. Xu, N. Gou, J. He, D. Li, H. Lan, Templateless, Plating–Free Fabrication of Flexible Transparent Electrodes with Embedded Silver Mesh by Electric–Field–Driven Microscale 3D Printing and Hybrid Hot Embossing, Adv. Mater. 33 (2021) 2007772. https://doi.org/10.1002/adma.202007772.

[152] Z. Jiang, K. Fukuda, X. Xu, S. Park, D. Inoue, H. Jin, M. Saito, I. Osaka, K. Takimiya, T. Someya, Reverse–Offset Printed Ultrathin Ag Mesh for Robust Conformal Transparent Electrodes for High–Performance Organic Photovoltaics, Adv. Mater. (2018) 1707526. https://doi.org/10.1002/adma.201707526.

[153] X. Zhu, Q. Xu, H. Li, M. Liu, Z. Li, K. Yang, J. Zhao, L. Qian, Z. Peng, G. Zhang, J. Yang, F. Wang, D. Li, H. Lan, Fabrication of High–Performance Silver Mesh for Transparent Glass Heaters via Electric–Field–

Driven Microscale 3D Printing and UV–Assisted Microtransfer, Adv. Mater. 31 (2019) 1902479. https://doi.org/10.1002/adma.201902479.

[154] J.H. Cho, D.J. Kang, N.S. Jang, K.H. Kim, P. Won, S.H. Ko, J.M. Kim, Metal Nanowire–Coated Metal Woven Mesh for High–Performance Stretchable Transparent Electrodes, ACS Appl. Mater. Interfaces. 9 (2017) 40905–40913. https://doi.org/10.1021/acsami.7b14342.

[155] W. Li, Y. Yang, B. Zhang, L. Li, G. Liu, C.F. Li, J. Jiu, K. Suganuma, Three–Dimensional Stretchable and Transparent Conductors with Controllable Strain–Distribution Based on Template–Assisted Transfer Printing, ACS Appl. Mater. Interfaces. 11 (2019) 2140–2148. https://doi.org/10.1021/acsami.8b18670.

[156] S.J. Kim, H.G. Yoon, S.W. Kim, Extremely Robust and Reliable Transparent Silver Nanowire–Mesh Electrode with Multifunctional Optoelectronic Performance through Selective Laser Nanowelding for Flexible Smart Devices, Adv. Eng. Mater. (2021) 2001310. https://doi.org/10.1002/adem.202001310.

Chapter 6

Summary and prospect

Liquid–mediated directed self–assembly driven by a difference in the solid surface states, as a novel additive manufacturing process, reveals incomparable process simplicity and low demand for equipment in soft electronic manufacturing. However, thus far, the practical application of self–assembled electronics is suffering from a lack of competitive performance. In this thesis, a fundamental DSA strategy and two sets of directed self–assembly systems have been demonstrated to pattern high–performance soft electrodes with substantial increases of application prospect, which triggered by the liquid–solid interfacial engineering with controllable surficial modifications.

In *Chapter 1*, the emergence, development, challenges, and opportunities of soft electronics have been briefly described. The different manufacturing technologies of micro–/nanoelectronics, including conventional photolithography, printing, and self–assembly, have been reviewed with the detailed processes, performance advantages, application range, and technical limits. It has shown that self–assembly technology exhibits tremendous potential to fulfill the manufacturing requirements from next–generation soft electronics; however, it still faces the challenges of low resolution and coffee ring effect. Therefore, the purpose of this study is to develop high–performance and versatile directed self–assembly strategy for addressing the current issues and introducing this technology into the future development of the soft electronic industry.

In *Chapter 2*, the experimental methods applied in this thesis have been summarized. In detail, the fabrication processes, including the DSA strategy for highly efficient solid surface energy regulation and the following electronic manufacturing based on the proposed DSA strategy, have been introduced. At the same time, the employed instruments and characterization tools for constructing the DSA substrates and evaluating the DSA–strategy–based self–assembled electronics have been listed. The information gives readers a general understanding of the DSA strategy and its potential functionality, which have been comprehensively discussed in *Chapters 3, 4,* and *5*.

In *Chapter 3*, the present technology creates the DSA substrates with precisely high–γ_s and strong–F_A designated regions via selective photo–oxidation by PVUV exposure and chemical polarization through alkali rinsing to strengthen the directed self–assembly property. The surface states of the modified regions have been clarified through the macroscopical characterizations using contact angle and sliding angle, the microscopical characterizations using XPS, FT–IR, and AFM, and the interfacial interaction analysis based on extended Fowkes model, revealing a significant enhancement of the directed self–assembly property on the modified regions with stronger shear stresses.

Water, as one of the most commonly used solvents in functional ink preparation, has been utilized to demonstrate the directed self–assembly property. By sliding the water droplet over the DSA substrate, an obvious wetting/dewetting and distinct pinning toward the water droplet have been observed on the modified regions, which

indicates that the DSA strategy provides a fundamental solution for controlling the liquid residence on the flexible substrate. Therefore, after adding functional solutes into the water, the aqueous functional ink can also be adsorbed onto the designated regions above the DSA substrate, leaving the self–assembled functional micro–/nanostructures after evaporation. It is worth mentioning that the spontaneous patterning behavior can be affected by the solute, including its gravity, surface condition, shape, and the used surfactant or ligand. During applying the DSA strategy practically, we need to pay extra attention toward the flowing behavior of the specific functional ink to ensure the optimal patterning performance.

On the other hand, because polymer materials with high–repellency surfaces are commercially available in great diversity, one can transform different kinds of these solids into the DSA substrates without the need to access cumbersome and expensive subtractive fabrication procedures. We anticipate that the DSA strategy will be further developed to be introduced into other existing liquid–mediated patterning technologies for facilitating performance in a cost–efficient way and thus satisfying emerging criteria in soft electronic manufacturing.

In *Chapter 4*, the present DSA strategy allows the spontaneous patterning of AuNP circuits with the extreme functionalities: high–resolution self–assembled circuits with unprecedented 600 nm in electrode width, high–definition forming for multiform circuits, suppressed coffee–ring effect, stable electrical properties of 14.1 ± 0.6 μΩ·cm, and long–term reliability. Particularly, the current resolution of the self–assembly technology is limited by that of the contact photomask, which directly determines the self–assembled areas and structures. Considering the wavelength of the developed PVUV incident light is around 150–200 nm, we envision that the potential resolution by DSA–triggered directed self–assembly could be further optimized to drop below 500 nm as long as the resolution issue of contact photomask preparation solves.

Furthermore, the self–assembled AuNP patterns have been used as high–resolution S/D and G electrodes for the integration of additively manufactured OTFTs with 1–μm–wide short channels; these OTFTs exhibited a large on–off ratio of 10^6 and a high field–effect mobility of 0.5 $cm^2 \cdot V^{-1} \cdot s^{-1}$. The resistivity of the pattern AuNP electrodes increases with the decrease of electrode linewidth due to the decreased density of the charge transports. In consequence, the resistivity deterioration affects the electrical performances of the OTFTs, in which both on–off ratio and field–effect mobility have been decreased on the OTFTs with the electrode linewidth of 1 μm. The observation suggests that during prototyping and designing soft electronics using liquid–mediated patterning technologies, we need not only to pay attention to triggering efficient stacking of the dispersed functional micro–/nanomaterials onto the designated positions, but also consider the size effect and the structure deformation/shrinkage toward the self-assembled patterns during solvent evaporation.

In *Chapter 5*, derived from the DSA strategy, the present technology enables the directed self–assembly of freeform TCs by spontaneous aligning of 1D NWs. Through overcoating AgNW functional ink on the DSA substrate to introduce the capillary force into the system, a periodically changed internal microflow field can be generated at the liquid/solid interface. Experimental observations and quantitative analyses indicate that the DSA–modified regions accelerate the internal flow owing to its strong shear stress and the pristine unmodified regions decelerate the internal flow due to its low shear stress, leading to the selective alignment of the dispersed AgNWs with high

controllability. Furthermore, the dispersed AgNWs can be aligned onto the designated regions precisely in a layer–by–layer manner through the changeable evaporative convections, resulting in a cross–linked network structure.

With appropriate manipulation of solid surface energy on the DSA substrate, the self–assembled AgNW TCs can be facilely patterned with unprecedentedly high transmittance (98.2 %, excluding the substrate), low sheet resistance (29.7 $\Omega \cdot sq^{-1}$) and reliable mechanical property. In parallel, the proposed self–assembly technology has been readily extended to align the arbitrary circuits with the high–accuracy fixation of the dispersed functional materials and thus promote the development of customized soft electronics. Therefore, the self–assembled functional circuits, using different 1D materials such as CNTs and DNAs, are planned to be explored for improving the versatility of directed self–assembly technology toward the development of highly biocompatible and durable soft electronics. Because we focus on developing the novel directed self–assembly technology instead of the AgNW–based electronics, the stability issue of the AgNW TCs has not been discussed herein. Considering the AgNWs suffer from atmospheric corrosion by oxidization and sulfurization, we suggest the utilization of post–treatments, such as overcoating the protective layer around the patterned AgNW network, to ensure the long–term reliability.

On the other hand, the proposed liquid–mediated self–assembly approaches advance other present additively manufactured technologies or conventional lithography technologies further by the tailorable movement manipulation of the functional micro–/nanomaterials directly with a high degree of freedom on the liquid–covered surface. This merit inspires the following study to bring the cost–effective and scalable liquid–mediated direct self–assembly technology from 2D surface into 3D space. Thus, it could satisfy all the requirements in both prototyping and manufacturing of spatial soft electronics dealing with the next–generation industrial revolution, including highly customized electrification kits as well as cognitive cyber-physical systems.

Research achievements

A) Journal papers

1. **Lingying Li**, Wanli Li*, Xuying Liu, Mizuki Tenjimbayashi, Hiroyo Segawa, Chisato Niikura, Tomonobu Nakayama*, and Takeo Minari*, Silver Nanowire Patterning via Microflow Velocity–Field–Gradient Manipulation for Tailored Flexible Transparent Conductors, Advanced Materials Technologies, accepted, 2022.
2. **Lingying Li**, Wanli Li*, Qingqing Sun, Xuying Liu, Jinting Jiu, Mizuki Tenjimbayashi, Tomonobu Nakayama*, and Takeo Minari*, Dual Surface Architectonics for Directed Self–Assembly of Ultrahigh–Resolution Electronics, Small, 17, 2101754, 2021. DOI: 10.1002/smll.202101754. *(Front cover)*
3. **Lingying Li**, Wanli Li, Tomonobu Nakayama*, and Takeo Minari*, Liquid–mediated Patterning for Micro–/Nanoelectronics: A Focused Review of Emerging Microfluidic Manipulation Techniques and the Path to Applications, Science and Technology of Advanced Materials, to be submitted.
4. **Lingying Li**, Wanli Li*, Ke Tong, Jiuting Jiu*, and Katsuaki Suganuma, Intense Pulsed Light–Induced Structure–Transformed Ultrathin Ni Shell for Improving the Chemical, Thermal, and Electrical Reliability of Metal Nanowire Electrodes without Transmittance Loss, Chemical Engineering Journal, 390, 124517, 2020. DOI: 10.1016/j.cej.2020.124517.
5. **Lingying Li***, Wanli Li, Jiuting Jiu, and Katsuaki Suganuma*, Efficient Assembly of High–Performance Reduced Graphene Oxide/Silver Nanowire Transparent Conductive Film Based on in Situ Light–Induced Reduction Technology, Applied Surface Science, 459, 732–740, 2018. DOI: 10.1016/j.apsusc.2018.08.060.
6. Wanli Li*, **Lingying Li**, Fei Li, Kohsaku Kawakami, Qingqing Sun, Tomonobu Nakayama, Xuying Liu, Masayuki Kanehara, Jie Zhang, and Takeo Minari*, Self–Organizing, Environmentally Stable, and Low–Cost Copper–Nickel Complex Inks for Printed Flexible Electronics, ACS Applied Materials & Interfaces, 14(6), 8146–8156, 2022. DOI: 10.1021/acsami.1c21633
7. Wanli Li, **Lingying Li**, Qingqing Sun, Xuying Liu*, Masayuki Kanehara, Tomonobu Nakayama, Jinting Jiu, Kenji Sakamoto, and Takeo Minari*, Direct Fabrication of High–Resolution and High–Performance Flexible Electronics via Surface–Activation–Localized Electroless Plating, Chemical Engineering Journal, 416, 127644, 2021. DOI: 10.1016/j.cej.2020.127644.
8. Qingqing Sun, Tianqi Gao, Xiaomeng Li, Wanli Li, Xiaoqian Li, Kenji Sakamoto, Yong Wang, **Lingying Li**, Masayuki Kanehara, Chuan Liu, Xinchang Pang, Xuying Liu*, Jianwen Zhao*, and Takeo Minari*, Layer–By–Layer Printing Strategy for High–Performance Flexible Electronic Devices with Low–Temperature Catalyzed Solution–Processed SiO2, Small Methods, 5, 2100263, 2021. DOI: 10.1002/smtd.202100263. *(Back cover)*
9. Wanli Li*, Qingqing Sun, **Lingying Li**, Jinting Jiu, XuYing Liu, Masayuki Kanehara, Takeo Minari*, and Katsuaki Suganuma, The Rise of Conductive Copper Inks: Challenges and Perspectives, Applied Materials Today, 18, 100451, 2020. DOI: 10.1016/j.apmt.2019.100451.
10. Wanli Li*, Yang Yang, Bowen Zhang, **Lingying Li**, Guiming Liu, Cai–Fu Li*, Jinting Jiu*, and Katsuaki Suganuma, Three–Dimensional Stretchable and Transparent Conductors with Controllable Strain–Distribution Based on Template–Assisted Transfer Printing, ACS Applied Materials & Interfaces, 11, 2140–2148, 2019. DOI: 10.1021/acsami.8b18670.

11. CaiFu Li*, Wanli Li, Hao Zhang, Jinting Jiu, Yang Yang, **Lingying Li**, Yue Gao, ZhiQuan Liu, and Katsuaki Suganuma, Highly Conductive Ag Paste for Recoverable Wiring and Reliable Bonding Used in Stretchable Electronics, ACS Applied Materials & Interfaces, 11, 3231–3240, 2019. DOI: 10.1021/acsami.8b19069.

12. Wanli Li*, **Lingying Li**, Yue Gao, Dawei Hu, Cai Fu Li, Hao Zhang, Jinting Jiu*, Shijo Nagao, and Katsuaki Suganuma, Highly Conductive Copper Films Based on Submicron Copper Particles/copper Complex Inks for Printed Electronics: Microstructure, Resistivity, Oxidation Resistance, and Long–Term Stability, Journal of Alloys and Compounds, 732, 240–247, 2018. DOI: 10.1016/j.jallcom.2017.10.193.

13. Wanli Li*, Dawei Hu, **Lingying Li**, Cai–fu Li, Jinting Jiu*, Chuantong Chen, Toshiyuki Ishina, Tohru Sugahara, and Katsuaki Suganuma, Printable and Flexible Copper–Silver Alloy Electrodes with High Conductivity and Ultrahigh Oxidation Resistance, ACS Applied Materials & Interfaces, 9, 24711–24721, 2017. DOI: 10.1021/acsami.7b05308.

B) Proceedings

1. **Lingying Li**, Wanli Li, Jiuting Jiu, and Katsuaki Suganuma, Effects of Oxygen Containing Groups on Barrier Layer on The Stability of Silver Nanowire Transparent Electrodes, *IEEE 17th International Conference on Nanotechnology (IEEE–NANO)*, Pittsburgh/U.S. and 2017, IEEE, New York/U.S. and 2017, 903–906. DOI: 10.1109/NANO.2017.8117267.

2. Wanli Li, **Lingying Li**, Cai–Fu Li, Jinting Jiu, and Katsuaki Suganuma, Enhanced High Temperature Stability of Printed Cu Wirings Based on Big Cu Particle Ink, Ag Element Addition, and Intense Pulsed Light Sintering, *19th International Conference on Electronic Packaging Technology (ICEPT 2018)*, Shanghai/China and 2018, IEEE, New York/U.S. and 2018, 1112–1115. DOI: 10.1109/ICEPT.2018.8480785.

C) Patent

1. **Lingying Li**, Takeo Minari, and Tomonobu Nakayama, 一次元導体によるパタ–ンの形成方法, patent pending, February 2022.

D) Conference

I. Oral presentation

1. **Lingying Li**, Wanli Li, Mizuki Tenjimbayashi, Masayuki Kanehara, Tomonobu Nakayama, Takeo Minari, Directed Self–Assembly Technology via Dual Surface Architectonics for Ultrahigh–Resolution Additively Manufactured Electronics, 第 82 回応用物理学会秋季学術講演会 2021, Japan, September, 2021.

2. **Lingying Li**, Wanli Li, Qingqing Sun, Takeo Minari, Tomonobu Nakayama, High–Resolution Flexible Electronics via Capillary–Force–Assisted Spontaneous Patterning, The 13th MANA International Symposium 2020 jointly with ICYS, Tsukuba, Japan, March, 2020.

3. **Lingying Li**, Wanli Li, Jiuting Jiu, Katsuaki Suganuma, Ultrathin and Uniform Ag@Ni Core–Shell Nanowires for High–Performance Stretchable Transparent Heater, Large–area, Organic & Printed Electronics Convention 2019, Munich, Germany, March, 2019.

4. **Lingying Li**, Wanli Li, Jiuting Jiu, Katsuaki Suganuma, A high–response transparent heater Ag@Ni

nanowire network with superior stretchability and long–term stability, The International Conference on Nanomaterials & Nanotechnology 2018, Stockholm, Sweden, October, 2018.

5. **Lingying Li**, Wanli Li, Jiuting Jiu, Katsuaki Suganuma, Facile fabrication of Ag–Ni alloy nanowire for high–performance transparent conductive electrodes with enhanced long–term stability, The 9th International Conference on Flexible and Printed Electronics 2018, Changzhou, China, September, 2018.

6. **Lingying Li**, Wanli Li, Jiuting Jiu, Katsuaki Suganuma, 2018 A3 Foresight 2nd Symposium on Organic/inorganic Nanohybrid Platforms for Precision Tumor Imaging and Therapy, Seoul, Korea, July, 2018.

7. **Lingying Li**, Wanli Li, Jiuting Jiu, Katsuaki Suganuma, 2017 A3 Foresight 2nd Symposium on Organic/inorganic Nanohybrid Platforms for Precision Tumor Imaging and Therapy, Osaka, Japan, December, 2017.

8. **Lingying Li**, Wanli Li, Jiuting Jiu, Katsuaki Suganuma, Highly flexible and reliable transparent conductive electrodes with reduced graphene oxide–coated silver nanowire networks, 2017 Fall Annual (161th) Meeting, Hokkaido, Japan, September, 2017.

9. **Lingying Li**, Wanli Li, Jiuting Jiu, Katsuaki Suganuma, Effects of Oxygen Containing Groups on Barrier Layer on the Stability of Silver Nanowire Transparent Electrodes, IEEE 17th International Conference on Nanotechnology, Pittsburgh, USA, July, 2017.

10. **Lingying Li**, Wanli Li, Jiuting Jiu, Katsuaki Suganuma, 銀ナノワイヤ–透明電極のためのバイア層形成効果, 実装学会第 31 回春季講演大会, Yokoyama, Japan, March, 2017.

II. Poster presentation

1. **Lingying Li**, Wanli Li, Qingqing Sun, Takeo Minari, Tomonobu Nakayama, High–Resolution Self–Assembly of Flexible Printed Electronics via Energy–Efficient Surface Architectonics, The 14th MANA International Symposium 2021 jointly with ICYS, Tsukuba, Japan, March, 2021.

2. **Lingying Li**, Wanli Li, Jiuting Jiu, Katsuaki Suganuma, 2018 A3 Foresight 2nd Symposium on Organic/inorganic Nanohybrid Platforms for Precision Tumor Imaging and Therapy, Seoul, Korea, July, 2018.

3. **Lingying Li**, Wanli Li, Jiuting Jiu, Katsuaki Suganuma, Fabrication of a reduced graphene oxide/silver nanowires transparent electrode with facile and rapid flame method, The 20th SANKEN International The 15th SANKEN Nanotechnology Symposium 2016, Osaka, Japan, December 2016.